Western University
Scholarship@Western

Digitized Theses | Digitized Special Collections

2009

GROWTH AND CHARACTERIZATION OF LIGHT-EMITTING SILICON NANOCRYSTALS

Christopher Ryan Mokry

Follow this and additional works at: https://ir.lib.uwo.ca/digitizedtheses

Recommended Citation
Mokry, Christopher Ryan, "GROWTH AND CHARACTERIZATION OF LIGHT-EMITTING SILICON NANOCRYSTALS" (2009). *Digitized Theses*. 4160.
https://ir.lib.uwo.ca/digitizedtheses/4160

This Thesis is brought to you for free and open access by the Digitized Special Collections at Scholarship@Western. It has been accepted for inclusion in Digitized Theses by an authorized administrator of Scholarship@Western. For more information, please contact wlswadmin@uwo.ca.

GROWTH AND CHARACTERIZATION OF LIGHT-EMITTING SILICON NANOCRYSTALS

(Spine title: Growth and Characterization of Silicon Nanocrystals)

(Thesis format: Monograph)

By

Christopher Ryan Mokry

Graduate Program in Physics

A thesis submitted in partial fulfillment
of the requirements for the degree of

DOCTOR OF PHILOSOPHY

The School of Graduate and Postdoctoral Studies
The University of Western Ontario
London, Ontario, Canada

© Christopher Ryan Mokry 2009

ABSTRACT

This thesis describes experimental and theoretical research aimed at understanding and manipulating the growth and optical characteristics of silicon nanocrystals (Si-nc). Si-nc were grown by implanting silicon ions into SiO_2 and annealing to promote the nanocrystal growth by precipitation and Ostwald ripening. This nanomaterial system has the potential for fabricating a silicon-based light emitter, and possibly a silicon laser. A silicon-based light emitter is the key component missing for complete integration of silicon photonic devices on microprocessors.

Samples were prepared with various doses of implanted silicon, annealed to various temperatures and times, and studied by photoluminescence (PL), cathodoluminescence (CL), transmission electron microscopy (TEM), positron annihilation spectroscopy (PAS), Rutherford backscattering spectroscopy (RBS) and ellipsometry. It was determined from the depth profile of Si-nc obtained by TEM that vacancy-type defects introduced by implantation play a critical role in the Si-nc growth. Consequently, a double implant experiment at 450 keV and 90 keV was designed to increase the vacancy-type defect concentration in the region of the 90 keV implant, and resulted in increased PL emission intensity. This knowledge of the growth mechanism is beneficial for optimizing the light emission of Si-nc, while minimizing production costs and resources.

A simple theoretical model to predict the spectrum of light emission from the dimensions of Si-nc using a one-dimensional finite square well was constructed.

The model reasonably predicted the PL emission spectrum for our Si-nc and for those published by other authors. Using the model the optical efficiency of the nanocrystals was determined and revealed a possible quasi-direct band gap transition predicted for nanostructured materials. The simple emission model provides a tool to understand the changes occurring to the Si-nc system through PL measurements.

Finally the PL and CL of Si-nc are discussed in detail. The knowledge obtained on the growth and optical properties of Si-nc was applied to explain the increase in PL intensity with implantation dose, and the eventual decrease in intensity at very high doses. The CL emission was at a dramatically different wavelength than the PL and was determined to be caused by defects at the surface of the Si-nc.

Keywords: silicon nanocrystals, quantum dots, ion implantation, growth mechanisms, optical properties

To my parents, Manfred and Heidi, and my sister Jennifer

ACKNOWLEDGEMENTS

I would like to thank Prof. Peter Simpson for being a fantastic mentor and supervisor. My experience at the University of Western Ontario has been great and you were a large part of that experience. I have enjoyed our conversations, including all your support, suggestions, constructive criticism, honesty, and availability. I have also valued the independence you provided in allowing me to pursue my PhD project, which has been a tremendous educational experience that I have benefited from.

I would also like to thank Prof. Andy Knights at McMaster University who started me on my PhD project and suggested Peter as my supervisor. Your ongoing expertise was invaluable and I always learned something from our discussions regarding the experiments I was conducting or had completed. Thank you for your ongoing support, suggestions, and constructive criticism. They have been greatly appreciated.

Numerous individuals from institutions in England, Austria, across Ontario, and other University of Western Ontario departments have assisted with my project. I would like to thank all these individuals for their assistance, but I would like to thank Mr. Jack Hendriks in particular. I have spent countless hours in Jack's lab and he has been a tremendous help in setting up experiments and maintaining the equipment. Without Jack it would have taken me much longer to complete my thesis and with greater obstacles.

To my family, who have always been my personal rock to which I look for

guidance and support, I want to thank them for their encouragement in pursuing my goals. I am very fortunate to have parents who are concerned and interested in my life, including this project and my ambitions. My sister Jennifer is always there for me and puts aside her own personal interests to help me out. Throughout my post secondary education she has been my editor in chief and she has left many of her marks on my thesis. Thank you for all the love, guidance, support, and help. I have always appreciated and cherished it.

Throughout my time at Western, I have made many friends in the Physics and Astronomy department during the lunch hour and through various intramural and departmental sports. Thank you for all the interesting conversations, a chance to stretch my legs, and the occasional beverage at the Grad Club.

I would like to thank the Western's men's varsity volleyball team. My three years on the team were fun and provided an opportunity to play at a competitive level again. We had some great nights away from the court and I made some lifelong friends.

Finally, I would also like to gratefully acknowledge the financial support I received as a graduate student from OGSST.

CONTENTS

Certificate of Examination ii

Abstract iii

Dedication v

Acknowledgements vi

List of Tables xi

List of Figures xiii

List of Acronyms xix

1. Introduction 1

1.1 Influence of Silicon Microelectronics 1

1.2 Optical Interconnects 3

1.3 Properties of Silicon 5

1.3.1 Porous Silicon 6

1.3.2 Silicon Nanocrystals (Si-nc) 7

1.4 Luminescence Mechanisms 9

1.4.1 Quantum Confinement 10

1.4.2 Interface/Surface States 11

1.5 Thesis Outline 12

2. Characterization 15

2.1 Overview 15

2.2 Ion Implantation 15

2.3 Transmission Electron Microscopy (TEM) 16

2.3.1 Sample Preparation 17

2.4 Rutherford Backscattering Spectroscopy (RBS) 18

2.5 Positron Annihilation Spectroscopy (PAS) 20

2.5.1 Doppler Broadening 22

2.6 Photoluminescence Spectroscopy (PL) 22

2.7 Cathodoluminescence Spectroscopy(CL) 25

3. Silicon Nanocrystal Growth 27
3.1 Overview 27
3.2 Transmission Electron Microscopy (TEM) 28
3.2.1 Sample Composition 28
3.2.2 Electron Beam Effects 30
3.2.3 Silicon Nanocrystal Size and Location 33
3.3 Rutherford Backscattering Spectroscopy (RBS) 36
3.3.1 Silicon Ion Distribution 37
3.4 Positron Annihilation Spectroscopy (PAS) 39
3.4.1 Vacancy-Type Defect Distribution 39
3.5 Verifying Vacancy-type Defect Correlation 45
3.6 Summary and Conclusions 52
4. Silicon Nanocrystal Optical Properties 54
4.1 Overview 54
4.2 Introduction 55
4.3 Quantum Confinement Models 57
4.3.1 One-Dimensional Finite Square Well 58
4.3.2 Three-Dimensional Finite Spherical Well 60
4.4 Recombination Strength 64
4.5 Discussion of Recombination Strength 70
4.5.1 Large to Medium Size Nanocrystals (> 1.75 nm) 70
4.5.2 Small Nanocrystals (< 1.75 nm) 71
4.6 Photoluminescence Simulations 73
4.7 Discussion of PL Simulations 74
4.7.1 TEM Distributions 74
4.7.2 Interface Defects 77
4.7.3 Coulomb Interaction 78
4.8 Summary and Conclusions 79
5. Luminescence 81
5.1 Overview 81
5.2 Photoluminescence 81
5.2.1 Implantation Dose 82
5.2.2 Annealing 88

5.2.2.1 Furnace versus Rapid Thermal Annealing 88
5.2.2.2 Nitrogen and Argon 90
5.2.2.3 Hydrogen 93
5.2.3 Photoluminescence Conclusions 95
5.3 Cathodoluminescence 96
5.3.1 Cathodoluminescence Conclusions 102

6. Conclusions 104

Appendices 108

A. Modeling PAS Results 108
A.1 Presence and Location of Silicon Nanocrystals 109

B. Quantum Mechanics Calculations 112
B.1 One-Dimensional Finite Square Well 112
B.2 Three-Dimensional Finite Spherical Well 115
B.3 Results 118

C. Photoluminescence Simulations 120

D. Coulomb Interaction 124
D.1 Coulomb Interaction for a Finite Square Well 125
D.2 Coulomb Interaction for a Finite Spherical Well 133
D.2.1 Comparison of Three-Dimensional Coulomb Interaction Results 135
D.3 Coulomb Interaction and Photoluminescence 137

Bibliography 141

Curriculum Vitae 147

LIST OF TABLES

3.1 Atomic percentage of elements present in different regions of the SiO_x film using energy dispersive X-ray spectroscopy (EDX). 30

3.2 Comparison of maximum transferable kinetic energy (E_{max}) with the displacement and sputtering energies at 200 kV. The displacement and sputtering energies were taken from SRIM [37]. 32

3.3 Median and mean Si-nc size as a function of depth for a 430 nm thick oxide layer implanted with 1.4×10^{17} silicon ions/cm^2 (20 at.% excess Si) and annealed at 1070°C for 3 hrs. The TEM image locations are illustrated in Figure 3.5, and the uncertainty in the mean diameter is the standard error and not standard deviation. 34

3.4 Electronic and nuclear stopping powers for different silicon implant energies tabulated by SRIM. 40

3.5 Summary of the peak wavelength and corrected PL intensity for the samples shown in Figure 3.12(c). The PL intensity was corrected for the system response. 49

3.6 Summary of the ellipsometry measurements at the pump wavelength of 325 nm. 51

4.1 One-dimensional and three-dimensional model parameters. 58

4.2 Summary of the experimental and simulated PL. The values in brackets of the "simulated" columns represent the difference between the experimental and simulated results. 74

5.1 A comparison of the important factors that affect the PL intensity for samples annealed at 1070°C for 3 hrs and 1170°C for 15 min. The values are calculated by converting the PL emission energy into the Si-nc distribution that emits light. Peak size refers to the mode of the distribution and FHWM stands for full width half maximum. The size distribution gets cut off at nanocrystal sizes greater than 3.5 nm due to the detector wavelength limit of 1000 nm. 85

5.2 List of luminescent defects in SiO_2 [100]. 102

A.1 Normalized S-parameter values simulated by POSTRAP5 for PAS data collected from the 430 nm thick SiO_2 film implanted at 90 keV and a dose of 1.4×10^{17} ions/cm^2. Sample (A) reference SiO_2 film, (B) as-implanted film, (C) annealed 10 sec. at 1170°C, and (D) annealed 30 min. at 1170°C. 109

B.1 Results for the one-dimensional *even* solution and the three-dimensional solution (which is equivalent to the one-dimensional *odd* solution). . . . 118

C.1 Summary of the experimental and simulated PL utilizing our own fit of the TEM distributions. The values in brackets of the "simulated" columns represent the difference between the experimental and simulated results. 123

D.1 Comparison of the Coulomb interaction energy determined utilizing the two trial wavefunctions. 132

D.2 Comparison of the Coulomb interaction energies determined through effective mass approximation (EMA), pseudopotentials (PS) [103], as a perturbation using Eq. D.19 (3D), and effective mass approximation utilizing the effective well width (EMA*). 136

D.3 Summary of the experimental and simulated PL utilizing our own fit of the TEM distributions. The values in brackets of the "simulated" columns represent the difference between the experimental and simulated results. 140

LIST OF FIGURES

1.1 Number of transistors on a microchip that demonstrates consistency with Moore's Law [3]. 2

1.2 Si photonic devices required for the implementation of microphotonics into integrated circuits [12]. 5

1.3 Direct and indirect semiconductors: (a) a direct transition with the emission of a photon and (b) an indirect transition via a non-radiative process. 6

1.4 Fabrication of Si-nc using ion implantation to enrich the oxide layer. . . 8

1.5 Widening of the Silicon band gap with quantum confinement. 10

2.1 A TEM sample prepared using the FIB and being removed by the molybdenum nanomanipulator. The samples are further thinned with the Ga ion beam until a thickness of approximately 25 nm. 18

2.2 The upper image shows the experimental setup and the bottom plot shows the backscattered results [39]. 20

2.3 A typical gamma ray energy spectrum due to positron annihilation showing how the S- and W-parameters are calculated. The S-parameter is determined by dividing the number of counts in the centroid of the spectral peak (region A) by the total number of counts in the spectral peak (region C). The W-parameter is determined by dividing the number of counts in the wing region of the spectral peak (region B) by the total number of counts in the spectral peak (region C). 23

2.4 Excitation of a direct and indirect band gap material by a pump laser [45]. 25

3.1 Energy dispersive X-ray spectrum of the SiO_x film near the surface. . . 29

3.2 EELS with a 4 eV window centered on (a) the silicon plasmon peak of 17 eV, and (b) the SiO_2 plasmon peak of 22 eV. 31

3.3 The increase in temperature of the specimen as a function of the specimen's thermal conductivity k [$Wm^{-1}K^{-1}$] and the beam's current [38]. 32

3.4 Damage caused by the electron beam at 200 pA/cm^2. The damaged region is contained within the circle. 33

3.5 (a) SRIM simulation of the implantation and vacancy-type defect distributions for a 90 keV implant plotted along with the mean size of the Si-nc determined from TEM. (b) TEM images including an outline indicating their location and orientation relative to the oxide film and the surface. The TEM samples were implanted at 90 keV to a dose of 1.4×10^{17} ions/cm^2, and annealed at 1070°C for 3 hrs. 35

3.6 The RBS measurements were performed with a 2.25 MeV $^4He^+$ beam. The noisy curves are the experimental results and the smooth curves are the QUARK models. The samples were implanted at 90 keV and a dose of 1.4×10^{17} ions/cm^2. (a) is the reference SiO_2, (b) is the implanted sample where the QUARK model uses the SRIM simulated implantation profile, and (c) is the implanted sample after it has been annealed. 38

3.7 S-parameter results of as-implanted samples implanted at 90 keV and various doses in a 430 nm thick SiO_2 film. The lines are to guide the eye. 41

3.8 Raw data spectrum at 3 keV comparing the reference SiO_2 with the as-implanted, 10 s anneal and 30 min anneal at 1170°C of a sample implanted with a dose of 1.4×10^{17} ions/cm^2. The data have been smoothed for clarity. 42

3.9 S-parameter results showing the reduction of vacancy-type defects after a short anneal time and the appearance of Si-nc after a longer anneal time in a 430 nm thick SiO_2 film implanted at 90 keV and a dose of 1.4×10^{17} ions/cm^2. The lines are fitted results of the collected experimental data using POSTRAP5 [57] and the model is discussed in Appendix A. 43

3.10 Progression of the photoluminescence peak wavelength for various implant doses. The apparent blue shift in the peak PL wavelength from 10 s to 2 min for the 1.4×10^{17} ions/cm^2 sample is not reliable and is due to the progressive increase in detector noise above 800 nm, which skews the peak PL wavelength to a higher value for very low intensity samples. 44

3.11 SRIM simulation of the vacancy-type defect profile (nuclear stopping) and ionization (electronic stopping), and PAS measurement for a 430 nm SiO_2 film implanted at 90 keV. The PAS results are from a sample implanted with a dose of 1.4×10^{17} ions/cm^2. The depth for the PAS measurement is the mean depth of the implanted positrons and not an absolute depth. 46

3.12 SRIM simulations of a 450 keV implant at 1 × 10^{17} ions/cm^2 and a 90 keV implant at 3 × 10^{16} ions/cm^2 where (a) is the relative normalized ion concentration, (b) is the relative normalized vacancy-type defect concentration, and (c) is the relative PL intensity of the samples. The PL intensity of the sample implanted at 90 keV is multiplied by a factor of 10 for clarity. 48

3.13 Pump beam intensity at different depths within samples A, B and C for (a) the TE modes and (b) the TM modes. The angle of incidence of the incoming beam was 45°. 53

4.1 On the left is the PL emission from a Si/SiO_2 superlattice (SL) structure and Si-nc in SiO_2 with similar shape and peak wavelength. On the right is the TEM histogram for the two different systems with similar Gaussian distributions [64]. 63

4.2 PL and TEM results superimposed using the one-dimensional model. (a) plots the results linearly, and (b) plots the results logarithmically. . 65

4.3 (a) Fitted recombination strength of the Si-nc with respect to the emission wavelength using the results in Figure 4.2. (b) Recombination strength converted into the equivalent nanocrystal diameter along with the recombination strength from the superlattice (SL) structures [76]. . 67

4.4 Luminescent lifetime measurement of Si-nc emitting light at a wavelength of 800 nm, fitted with a stretched exponential. The luminescent lifetime measurements were performed utilizing a monochromator and photomultiplier tube, along with a pump wavelength of 473 nm and a pump power of 40 mW. 68

4.5 Dispersion factor plotted along side the recombination strength indicating similarities in the trend and peak location. The luminescent lifetime measurements were performed with a pump wavelength of 473 nm and a pump power of 40 mW. The beam spot was approximately 1 mm in diameter. 69

4.6 Lifetime measurements at various wavelengths that were performed with a pump wavelength of 473 nm and a pump power of 40 mW. The beam spot was approximately 1 mm in diameter. 71

4.7 TEM image showing smaller nanocrystals closer to larger ones. 72

4.8 Simulated PL (in red) of Si-nc in SiO_2 for a Si concentration of 37% annealed at 1250°C for 1 hr. The experimental PL is from Priolo *et al.* [64], which was previously shown in Figure 4.1. 75

4.9 The simulated PL emissions are from Table 4.2 sample's $A2$ (a), $B2$ (b), $B3$ (c), $B4$ (d), $B5$ (e), and $B6$ (f). The experimental PL for (a - b), and (d - f) are from Priolo [64], and (c) is from Iacona [80]. 76

4.10 PL peak wavelength as a function of Si-nc diameter. A linear relationship exists between the results with a square symbol (□), and the linear fit is from the square symbols. The results with a triangular symbol (△) appear to be outliers. 77

5.1 PL intensity for samples implanted with different doses of Si. The samples were annealed at 970°C for 10 hrs, 1070°C for 3 hrs, or 1170°C for 15 min. All samples after the high temperature anneals were annealed at 450°C in a mixture of hydrogen and nitrogen. 84

5.2 Theoretical size distribution that emits light for samples implanted at 90 keV, and doses of 6.1×10^{16} ions/cm^2 and 1.4×10^{17} ions/cm^2. Both samples were annealed at 1170°C for 15 min and at 450°C for 1 hr in a mixture of hydrogen and nitrogen. 85

5.3 (a) the PL peak wavelength and (b) the mode for the nanocrystal size of samples annealed at 1070°C for 3hrs and 1170°C for 15 min in nitrogen, followed by a 1 hr hydrogen anneal. 87

5.4 PL intensity of similar samples annealed in a furnace or an RTA at 1070°C for 3 hrs. Both samples were annealed at 450°C for 1 hr in forming gas to reduce additional dangling bonds. The RTA ramp rate was 100°C/s. 89

5.5 PL intensity of two samples annealed in either argon or nitrogen at a temperature of 1100°C for 1 hr. All samples were implanted with silicon at 425 keV and a dose of 1×10^{17} ions/cm^2, and two of the samples were implanted with nitrogen at 250 keV and a dose of 5×10^{14} ions /cm^2. 92

5.6 Evolution of the PL intensity for various Si implant doses at an anneal temperature of 1170°C in nitrogen. 93

5.7 PL intensity before and after a 1 h anneal at 450°C in forming gas (5%H_2 95%N_2). The sample was implanted at 90 keV, a dose of 1.2×10^{17} Si ions /cm^2 and annealed at 1170°C for 15 min. 95

5.8 CL and PL emission spectra for a sample implanted at 90 keV and a dose of 1.4×10^{17} ions/cm^2. The sample was annealed in nitrogen at 1170°C for 15min followed by a passivation anneal at 450°C for 1 hr. The CL measurement was done at an energy of 6 keV with a 0.6 mA electron beam current. The CL emission was smoothed for clarity. . . . 98

5.9 A 10 keV CL measurement with various target currents measured by a Faraday cup. The sample was implanted at 90 keV and a dose of 1.4×10^{17} ions/cm^2. . . . 99

5.10 A progression of the CL at 10 keV with a target current of 5 nA. 99

5.11 Picture of a sample during implantation emitting light in the blue region of the visible spectrum. 101

5.12 Comparison of defects excited by PL and CL. The two PL measurements are from the same sample. The first PL measurement was taken after the ion implantation stage and the other PL measurement was measured after a nitrogen and hydrogen anneals. The sample had a 1 μm thick oxide layer implanted at 450 keV and a dose of 1×10^{17} ions/cm^2. The sample was annealed at 1070°C in nitrogen gas and 450°C in 5%H_2 95%N_2. The CL measurement was done at 10 keV with an electron beam current of 5 nA. All the curves were smoothed for visual clarity. . 102

A.1 Model used in POSTRAP5 to fit the PAS results for the implanted and annealed samples. 109

B.1 The emission energy and wavelength of silicon nanocrystals for the one-dimensional *even* solution and the three-dimensional solution (or one-dimensional *odd* solution). 119

C.1 The TEM distribution for (a) is from Priolo [64], and (b - f) are from Iacona [80]. Both the author's fits and our own are included in the TEM distributions. The TEM distributions refer to sample's $A2$ (a), $B2$ (b), $B3$ (c), $B4$ (d), $B5$ (e), and $B6$ (f) from Table C.1. 121

C.2 The simulated PL intensities are from our own fits' of the TEM size distributions and not those stated in References [64, 80]. The simulated PL emissions are from Table C.1 sample's $A2$ (a), $B2$ (b), $B3$ (c), $B4$ (d), $B5$ (e), and $B6$ (f). The experimental PL for (a - b), and (d - f) are from Priolo [64], and (c) is from Iacona [80]. 122

D.1 Comparison of the Coulomb interaction energy evaluated utilizing the two trial wavefunctions. 132

D.2 Plot comparing the Coulomb interaction results from the effective mass approximation (EMA), pseudopotentials (PS) [103], as a perturbation (3D), and effective mass approximation utilizing the effective well width (EMA*). 137

D.3 The emission energy and wavelength for both the one-dimensional and three-dimensional models, with the inclusion of the Coulomb interaction. 138

D.4 The PL emission for (a - b), (d - f) are from Priolo *et al.* [64], and (c) is from Iacona *et al.* [80]. The simulated PL intensity incorporates the Coulomb interaction and is evaluated utilizing our own fits' of the TEM size distributions and not those stated in Ref. [80]. 139

LIST OF ACRONYMS

AFM	Atomic Force Microscopy
CL	Cathodoluminescence
CMOS	Complementary Metal Oxide Semiconductor
EDX	Energy Dispersive X-ray Spectroscopy
EELS	Electron Energy Loss Spectroscopy
EL	Electroluminescence
EMA	Effective Mass Approximation
FEG	Field Emission Gun
FIB	Focused Ion Beam
FTIR	Fourier Transform Infrared Spectroscopy
ITRS	International Technology Roadmap for Semiconductors
NBOHC	Non-Bridging-Oxygen Hole Centres
PAS	Positron Annihilation Spectroscopy
PL	Photoluminescence
PS	Pseudopotential
QUARK	Quantitative Analysis of Rutherford Kinematics
RBS	Rutherford Backscattering Spectroscopy
RTA	Rapid Thermal Annealer
SEM	Scanning Electron Microscope
Si-*nc*	Silicon Nanocrystals
SL	Superlattice
SRIM	The Stopping and Range of Ions in Matter
TEM	Transmission Electron Microscopy

CHAPTER 1

Introduction

1.1 Influence of Silicon Microelectronics

The silicon microelectronic industry creates numerous products, for various applications, that have become crucial to our daily routines. The majority of individuals use a personal computer at work or at home to check their e-mail, create reports and presentations, access and analyze information, and for many other applications. Cell phones are also ubiquitous, allowing individuals to connect and communicate with friends, family, or colleagues anywhere and at any time. These are just two examples of products that rely on integrated circuits, but it also highlights the importance of these products in our daily lives.

The microelectronics industry's success stems from a variety of factors. A critical factor is the use of silicon, a widely abundant material with excellent mechanical and thermal properties that allows for the easy processing and manufacturing of devices [1]. The industry's success is also due to the improved performance of every new generation of products and the continued decrease in the cost per component. The concept of continued improvement and cost savings has been called Moore's Law after Gordon Moore who in 1965 projected that the number of transistors on a microchip would double every two years [2]. From the time when Gordon Moore first observed this scaling trend, it has been the driving force behind the micro-

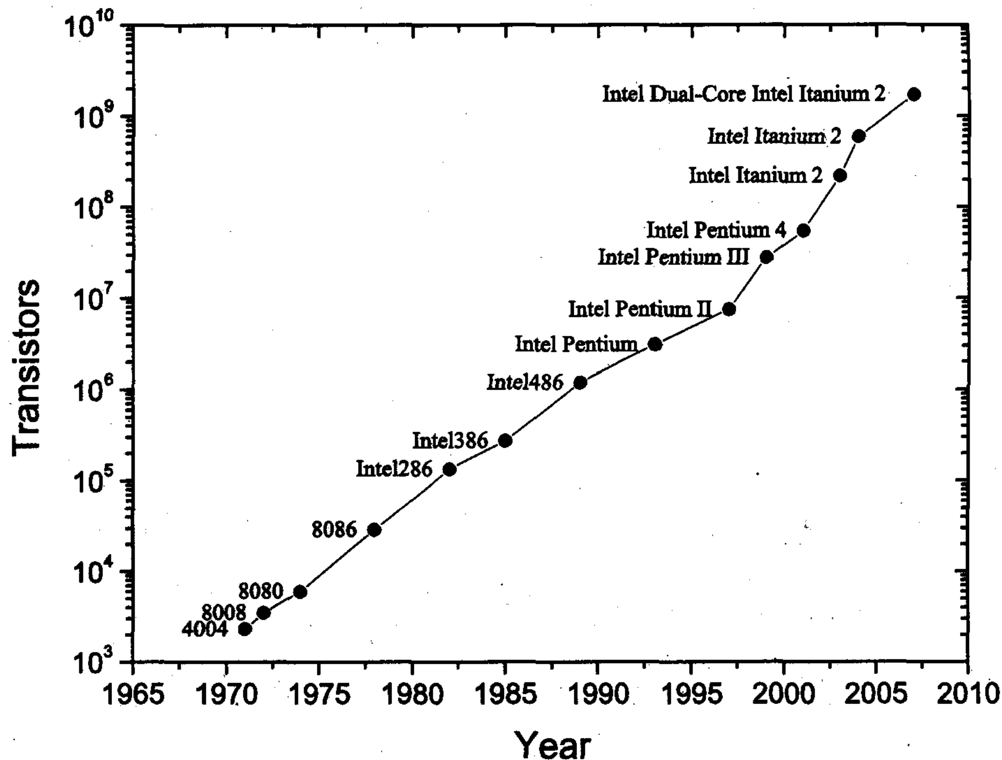

Figure 1.1: Number of transistors on a microchip that demonstrates consistency with Moore's Law [3].

electronics industry's development of smaller microchips with increasing numbers of transistors, and is illustrated in Figure 1.1. The increased number of transistors has improved the microchip's computing power while maintaining a reasonable cost.

The current goals and benchmarks for the scaling of microchips are monitored by the International Technology Roadmap for Semiconductors (ITRS). ITRS is an organization comprised of five different semiconductor manufacturing regions interested in the sustained health of the industry through cost effective advancements in integrated circuit performance [4]. In order to maintain Moore's Law, the consortium prepares every two years an updated roadmap outlining advancements in equipment and processes, future challenges, and possible solutions to these challenges. Historically the challenges to maintaining Moore's Law have been in regards

to the transistors, but the consortium has for several years highlighted another problem, the interconnects that link to the transistors.

Interconnects link transistors together, but as the number of transistors in an integrated circuit increases, so too do the number of required interconnecting wires. The current metallic interconnects on a microchip are comprised of two kilometers of wire per square centimeter and a very complex architecture of twelve metallic levels [5]. This complexity and length of wiring produces delays in signal propagation, tremendous power consumption (most of which is converted to heat), heating of the microchip, signal cross-talk, and signal latency. In addition, these problems are exacerbated by the continued scaling down of microchips to smaller sizes and interconnect delays will be the foremost speed limiting factor in future integrated circuits. In the ITRS's chapter on interconnects the performance requirements will not be met beyond 2010 [5]. However, a possible solution to the interconnect problem is optical interconnects.

1.2 Optical Interconnects

Telecommunication systems have already been revolutionized by optical interconnections, which unfortunately do not convert well into the dense, short distance environment of the integrated circuit. The photonic devices fabricated for the telecommunications industry are dominated by III/V semiconductors that are too large and expensive, and have poor material and fabrication compatibility with silicon. As such, silicon photonics may be capable of bridging these gaps. The infrastructure and mature fabrication technology necessary for silicon photonics are

available, which reduces some of the implementation and fabrication costs associated with their production. Major microelectronic manufacturers are aggressively pursuing microphotonics focused primarily on silicon [6].

Optical interconnects provide numerous advantages over their metallic counterparts. They reduce power consumption and heat dissipation, and they significantly reduce crosstalk due to strong confining waveguides and highly collimated laser beams. In addition, RC delays and signal propagation time would be reduced because the signal would be carried by neutral photons. Optical devices can operate at higher frequencies, which would allow for increased bandwidth, higher frequency modulation (or bit rate), low distortion transmission, wavelength division multiplexing, ultra-short pulses, and compatibility with future high bandwidth technology [7]. Finally, the potential for fibre optic cables to be directly connected to a personal computer would be feasible.

In order to implement optical interconnects, three essential devices are required: a laser or LED; an optical modulator or switch; and a photodetector. Other passive devices would also be required, including waveguides, optical routers, and optical switches [8]. The required components for the implementation of optical interconnects are shown in Figure 1.2. These basic components, including photonic integrated circuits, have been tested and employed, except for a Si laser, which is a major limitation in integrating silicon photonics into microprocessing [9]. A laser is preferred over a LED because incoherent light from the LED is difficult to focus and may not be sufficient for dense, high speed interconnects [10]. It is difficult for silicon to emit light due to its indirect band gap, which has a tendency

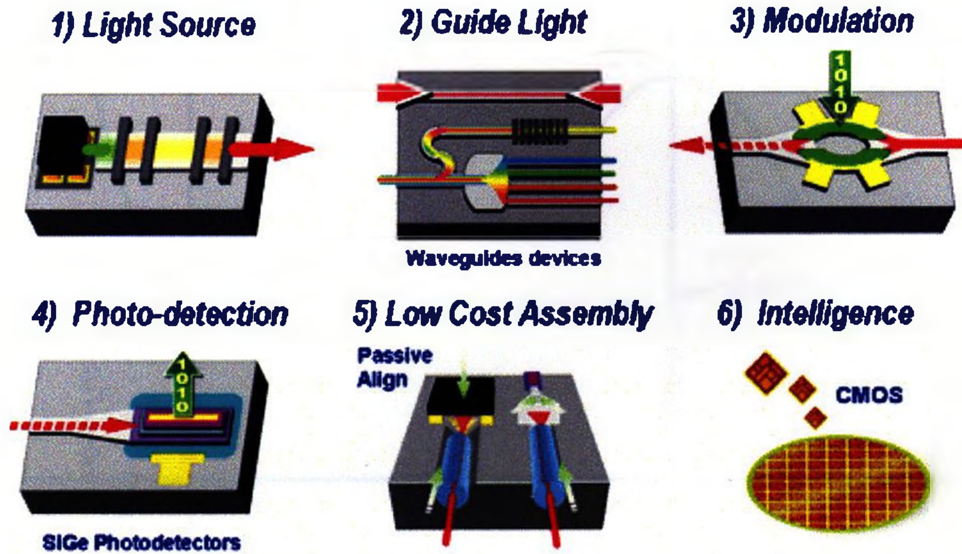

Figure 1.2: Si photonic devices required for the implementation of microphotonics into integrated circuits [12].

for non-radiative recombination processes, particularly since the radiative process has a longer spontaneous lifetime in the millisecond range [10]. As well, Auger or free carrier absorption prevents population inversion or optical amplification in silicon. Therefore, material engineering is required for silicon to luminesce and to date, the most successful attempts have been in silicon nanostructures that modify the electronic properties of the free carriers [11].

1.3 Properties of Silicon

Silicon is an indirect band gap semiconductor, which means that the bottom of the conduction band does not align with the top of the valence band as it does in a direct band gap semiconductor (illustrated in Figure 1.3). In an indirect band gap material, the excitation of electrons into the conduction band is a simultaneous two step process whereby the electron absorbs enough energy to overcome the band

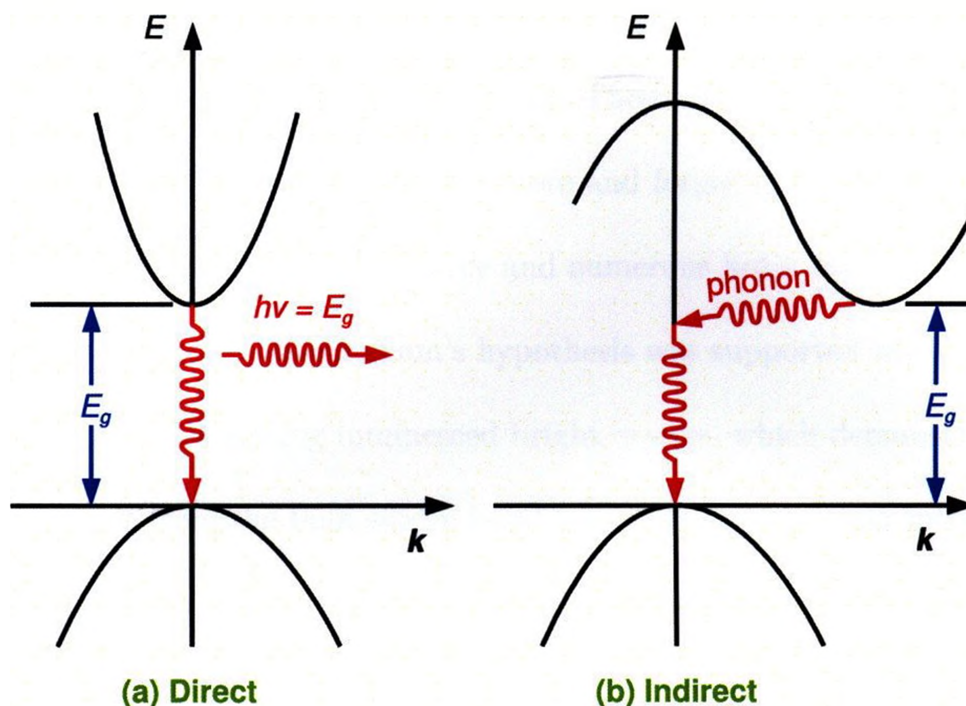

Figure 1.3: Direct and indirect semiconductors: (a) a direct transition with the emission of a photon and (b) an indirect transition via a non-radiative process.

gap and a phonon is required to conserve momentum. In contrast, the emission of a photon in a direct band gap results from the energy lost as an electron transitions from the valence band to the conduction band. For indirect band gap materials, the majority of transitions occur through recombination levels within the band gap, which result in energy being given to the lattice as opposed to the emission of a photon [13]. The inefficient emission of silicon is due to its indirect band gap, which can be overcome through the use of nanostructured materials, such as porous silicon or silicon nanocrystals.

1.3.1 Porous Silicon

A means to overcome silicon's indirect band gap was accidentally discovered in the mid 1950's by researchers at Bell Laboratories. The Bell Laboratories' re-

searchers were attempting to polish silicon wafers electrochemically, but under certain conditions holes developed in the wafers. These unexpected results were documented in a Bell Laboratories' technical note and forgotten until the early 1990's when L.T. Canham postulated that large and numerous holes could result in quantum confinement effects [14]. Canham's hypothesis was supported when the porous silicon material he was testing luminesced bright orange, which demonstrates a significant blue-shift from the bulk silicon band gap energy in the near infrared.

Canham's discovery resulted in significant interest in porous silicon, particularly for the development of silicon optoelectronic devices and a silicon laser. However, interest waned as chemical and mechanical instabilities, and difficulties forming electrical contacts proved problematic. Eventually interest shifted toward materials that incorporated the quantum confinement phenomenon of porous silicon into a medium more amenable to engineering, such as silicon nanocrystals embedded in silicon dioxide. Compared to silicon, silicon dioxide (SiO_2) has a large band gap, thus providing the potential barrier required for quantum confinement. As well, both silicon and SiO_2 are compatible with current complementary metal oxide semiconductor (CMOS) technology [15].

1.3.2 Silicon Nanocrystals (Si-nc)

Silicon nanocrystals embedded in SiO_2 exhibit strong luminescence at room temperature and are of interest for the development of silicon photonic devices that are compatible with silicon processing techniques. Since the discovery of intense red luminescence from porous Si in 1990, extensive work has been completed on

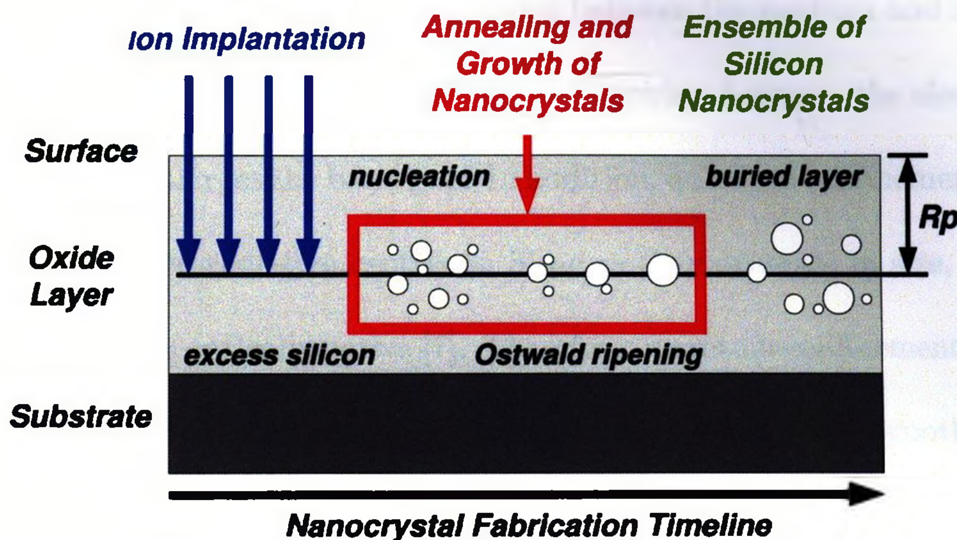

Figure 1.4: Fabrication of Si-nc using ion implantation to enrich the oxide layer.

the optical properties of porous Si and Si-nc [14, 16]. Since Si-nc are embedded in a dielectric matrix, they are more appealing than porous silicon in regards to device fabrication because they offer more surface stability and material rigidity [7]. Many techniques for fabricating Si-nc exist, such as sputtering [17], plasma enhanced chemical vapour deposition [16], laser ablation [18], and ion implantation [19]. In order for crystalline nanoclusters to form, annealing temperatures greater than 1000°C are required [20].

In the work described in this thesis, ion implantation was utilized to introduce excess silicon into SiO_2 in order to form Si-nc. Ion implantation was chosen because it is a common CMOS process and allows accurate control over the amount of added silicon. The required processing sequence for the fabrication of Si-nc through ion implantation is illustrated in Figure 1.4.

The high luminescence of Si-nc is due to three distinct properties: quantum confinement of free carriers; Brillouin zone folding and the uncertainty in momentum

space; and the difference in the refractive index between the medium and the dielectric matrix. Quantum confinement increases the overlap between the electron-hole wavefunctions and enlarges the band gap. In addition, quantum confinement reduces the probability of non-radiative centres in Si-nc as they decrease in size, which allows more Si-nc to be optically active [7]. Therefore, quantum confinement improves the efficiency of the radiative processes. Brillouin zone folding was hypothesized by Gnutzman and Clausecker [21] approximately 35 years ago. They speculated that thin layers on the order of unit cell dimensions could fold the Brillouin zone resulting in 'quasi-direct' band gap structures. Direct band gap structures as already mentioned are more efficient at emitting photons than indirect band gap structures. As well, uncertainty in momentum space increases the more carriers are confined spatially, relaxing the momentum conservation rule or leading to optical transitions not involving phonons (quasi-direct) [22]. Therefore, a quasi-direct transition would increase the probability of light emission. The efficient emission of light from Si-nc is also due to their surrounding matrix of SiO_2, which has a lower refractive index than silicon and allows for the greater extraction efficiency of the light from the Si-nc [9]. All the reasons reviewed above regarding nanocrystals improve the efficiency of light emission from silicon, but there is another mechanism by which nanocrystals can luminesce, discussed below.

1.4 Luminescence Mechanisms

In order for Si-nc to luminesce, they need to be optically or electrically excited. Optical excitation requires a photon with sufficient energy to create an electron-

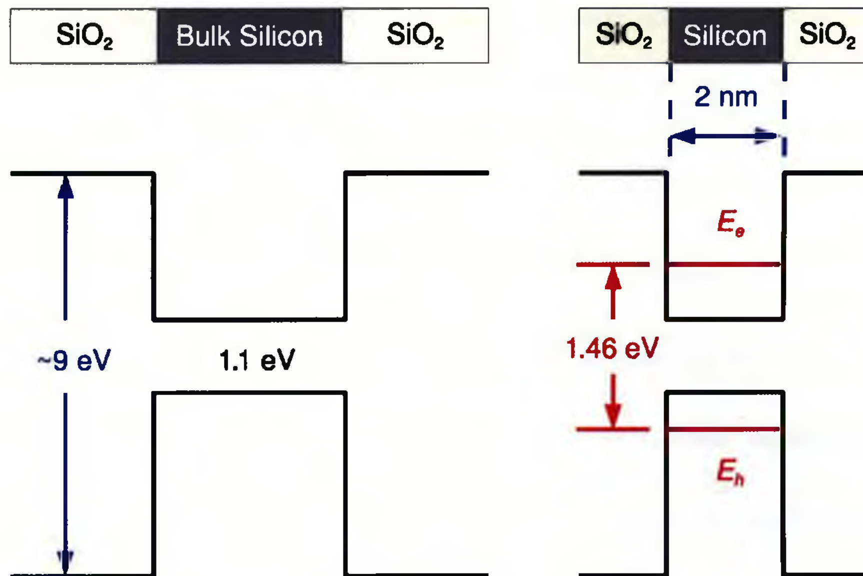

Figure 1.5: Widening of the Silicon band gap with quantum confinement.

hole pair across the band gap. Electrical excitation requires an electric field large enough for the electrons to overcome the band gap leaving behind a hole. However, in optical excitation two radiative recombination mechanisms have been observed and are highly debated [23–30]. The two radiative recombination mechanisms are quantum confinement and interface/surface states .

1.4.1 Quantum Confinement

As the dimensions of the Si-nc become comparable with or smaller than the exciton Bohr radius of bulk silicon ($\sim$ 4.3 nm) [31], quantum confinement effects become evident. Quantum confinement produces discrete energy levels and widening of the bulk silicon band gap (shown in Figure 1.5). Evidence of quantum confinement was found in porous silicon with a blue-shift in photoluminescence for silicon dimensions less than 10 nm in diameter, which suggests band gap widening [32].

Quantum confinement or spatial localization, as previously mentioned, results

in several effects that improve the light emission of silicon. Spatial localization enhances the overlap of electron and hole wavefunctions, which increases the probability of electron-hole pairs recombining radiatively. Even though the electron and hole can be located anywhere in bulk silicon, they become increasingly localized in Si-nc minimizing the uncertainty in Δx. According to the Heisenberg uncertainty principle, the uncertainty in the wave vector, Δk, then increases with spatial confinement. Therefore, adequate confinement can result in sufficient uncertainty regarding the wave vector to allow quasi-direct transitions. However, there are surface states that also luminescence and can compete with quantum confinement, thus complicating the system.

1.4.2 Interface/Surface States

It has been observed that porous silicon smaller than 2.8 nm in diameter does not necessarily emit light according to the quantum confinement model [24]. M. V. Wolkin *et al.* observed this phenomenon through photoluminescence (PL) measurements of porous silicon samples fabricated in an argon ambient and exposed to an oxygen environment. The PL red-shifted after exposure to oxygen and this was more noticeable for smaller nanocrystals than larger ones. The use of Fourier transform infrared spectroscopy (FTIR) on the samples demonstrated an increase in the transmittance of the Si-O-Si bonds within the material, which increased with exposure to oxygen and suggests increased Si=O bonds. The Si=O bond at the interface is an effective radiative trap, attracting the electrons and holes at the surface where they recombine radiatively. Therefore, the emitted energy from a small nanocrystal is

affected by the Si=O bond, whose energy depends on the stability of the bond and is related to the size of the nanocrystal [24]. However, Godefroo *et al.* [33] recently completed PL measurements in large magnetic fields and determined that Si-nc's annealed in hydrogen emitted light according to the quantum confinement model. Consequently, if samples are annealed in hydrogen, their emission will be dominated by quantum confinement and a model to approximate the emission characteristics can potentially be determined.

Several research groups have investigated the emission energy of Si-nc using various theoretical approaches, such as the effective mass approximation [34], truncated crystal method [34], direct molecular calculations [34], empirical tight-binding [35], empirical pseudo-potential [34, 36], and other methods. First principles calculations generally overestimate the emission energy and the other theoretical methods employ fitted parameters, which naturally results in good agreement [31]. As a result, some form of first principles calculation or model that can approximate the energy of the Si-nc would be of interest to researchers.

1.5 Thesis Outline

This thesis focuses on experimental and theoretical work to understand the growth and optical properties of silicon nanocrystals in SiO_2. The chapters are laid out as follows:

Chapter 2 reviews the six key experimental techniques utilized to understand the growth and optical properties of Si-nc. The six experimental techniques were: ion implantation; transmission electron microscopy (TEM); positron annihilation

spectroscopy (PAS); Rutherford backscattering spectroscopy (RBS); photoluminescence (PL); and cathodoluminescence (CL). In addition to the discussion of the techniques themselves, specific details regarding the unique experimental setups are summarized.

Chapter 3 focuses on the growth of the Si-nc embedded in SiO_2. Along with simulations, the TEM, PAS, RBS, and PL measurements were utilized to investigate the location and size distribution of the Si-nc in the SiO_2 matrix. The Si-nc size distribution and location were found to be correlated with the vacancy-type defect distribution introduced by the ion implantation. Since a correlation between the vacancy-type distribution and Si-nc size distribution was observed, the manipulation of the growth of the Si-nc using additional vacancies deliberately introduced, was attempted. This manipulation was expected to affect the Si-nc's optical properties and verify the observed correlation. The manipulation of the Si-nc's growth was done using a double implant, whereby the first implant was deep in the SiO_2 film and the second implant was shallow in the SiO_2 film. The deep implant affected the shallow implant's vacancy-type defect distribution allowing larger nanocrystals to be grown, which should be observed in the PL measurements. As hypothesized, a significant change occurred in the PL emission, thus verifying the correlation between the Si-nc's growth and the vacancy-type defect distribution.

In Chapter 4 the optical properties of the Si-nc are examined and two first principle models are introduced: a one-dimensional finite square well and a three-dimensional spherical well. The one-dimensional model approximated the emission energy very well compared to the overestimation of the emission energy by the

three-dimensional model. Although Si-nc are three-dimensional structures, there is evidence in the literature to suggest that a one-dimensional model is applicable to Si-nc. Through the application of the one-dimensional model, the recombination strength or radiative emission efficiency was determined. The recombination strength was verified through luminescent lifetime measurements and corresponded very well to the recombination strength results of superlattice structures, which are considered one-dimensional structures since the electron confinement is in one dimension only. As well, other published TEM size distributions were examined using the one-dimensional model and the Si-nc recombination strength to predict the PL spectrum. Good agreement occurred for distributions of smaller nanocrystals and greater deviations occurred for larger distributions. Rationales for the observed deviations are discussed.

Chapter 5 investigates the luminescence of the Si-nc through PL and CL measurements. The processing steps that affect the PL intensity are reviewed, employing the observations described in Chapters 3 and 4 on the growth and optical properties. These observations were applied in order to understand the rise and fall of PL intensity depending on implantation dose and annealing temperature. The CL measurements provided emission characteristics that were either caused by the excitation of a second excited state or by the creation and excitation of defects. After some experimentation and a literature review, the CL emission characteristics were concluded to be related to defects.

The final chapter summarizes the conclusions of each chapter and provides suggestions for future work.

CHAPTER 2

Characterization

2.1 Overview

This chapter describes the equipment and techniques utilized to investigate the growth mechanism and luminescence of silicon nanocrystals (Si-nc). The key techniques in determining the growth and luminescence were ion implantation, transmission electron microscopy (TEM), Rutherford backscattering spectroscopy (RBS), positron annihilation spectroscopy (PAS), photoluminescence (PL), and cathodoluminescence (CL). Since the majority of these techniques are well established and in-depth books have been written, only a brief overview of each technique will be given and specific details regarding unique experimental setups are provided.

2.2 Ion Implantation

Ion implantation is a technique utilized in CMOS technology to incorporate dopant atoms into a target material in a very controlled and precise manner. Ions are accelerated to thousands of volts and directed toward a target material creating a cascade of damage until the dopant atom losses all of its energy and comes to rest in some location. The loss of energy and trajectory of the dopant atom is a random process due to scattering events, but since a large number of atoms are implanted the distribution of implanted ions can be determined. A Monte Carlo program,

the stopping and range of ions in matter (SRIM) [37], allows the distribution of implanted ions to be simulated with fairly good accuracy.

The scattering events that create damage in the target material and the loss of energy to the dopant atoms comes in the form of electronic and nuclear interactions or stopping powers as they are more commonly known. Electronic stopping results from the interactions between the implanted atoms and electrons in the material as the atoms move through the target material. Nuclear stopping results from collisions between implanted atoms and stationary target atoms, whereby the implanted atoms loss energy through interactions with the electric field surrounding the nucleus of the target atom. The collisions between the implanted and target atoms results in the target atom being recoiled and the implanted atom continuing on a deflected path. The recoiled target atoms leave behind empty spaces in the lattice, which are called vacancies.

2.3 Transmission Electron Microscopy (TEM)

Transmission electron microscopy (TEM) is a technique that examines materials on a small scale by exposing very thin samples to an electron beam. The transmitted electrons are detected by a fluorescent screen and transferred to a CCD camera that records the results as a digital image. The recorded images reflect the interaction that occurred between the electrons and the material. From the collected images some analysis can be performed which in our case was to determine the size distribution of the Si-nc. In addition to the recorded images secondary signals are produced by the electrons which can be used in analyzing properties of the material.

Electrons are a type of ionizing radiation that produces secondary signals, which are useful in analyzing properties of materials, such as chemical composition [38]. Two of the techniques available in the TEM environment that utilize secondary signals are energy dispersive X-ray spectroscopy (EDX) and electron energy loss spectroscopy (EELS). EDX examines characteristic X-rays to determine the type of atoms present in a small region. Unfortunately, EDX complicates the analysis by detecting X-rays produced by scattered electrons from atoms not in the region of interest. Therefore, EDX was used to determine the approximate chemical composition of certain regions in the SiO_x film. EELS analyzes the energy lost by electrons passing directly through the sample and can distinguish between atomic species. A small energy window centered on the plasmon peak of an atom can enhance the features associated with that atom. This technique was used to determine whether the observed particles were composed of silicon. To make use of TEM, thinning the sample to approximately 25 nm thick is critical to achieving good contrast between silicon and SiO_2. Thinning the material to this thickness required delicate techniques, which are not typically performed and are described in the next section.

2.3.1 Sample Preparation

The TEM samples were thinned through vertical milling using a Leo 1540 focused ion beam (FIB)/scanning electron microscope (SEM) cross beam. Vertical milling is a sputtering process in which a Ga ion beam creates two wedge-shaped trenches in the sample, thus leaving a thin slice of material. Figure 2.1 demonstrates the removal of the thin slice from the bulk material, which is thinned further and

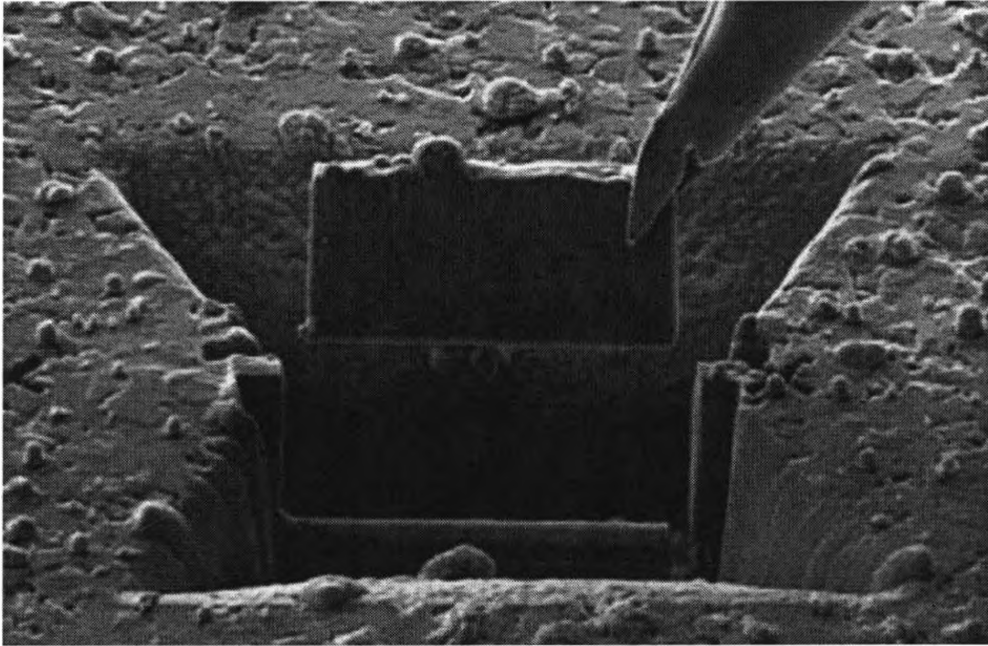

Figure 2.1: A TEM sample prepared using the FIB and being removed by the molybdenum nanomanipulator. The samples are further thinned with the Ga ion beam until a thickness of approximately 25 nm.

imaged. Platinum was deposited on the sample surface prior to milling to protect the surface layer and a molybdenum tip was used to remove and hold the samples. Images of the vertically-milled samples were captured by a JEOL 2010 field emission TEM/STEM with a Gatan electron energy loss spectrometer energy filter. The captured images permitted the size distribution of the Si-nc to be determined as a function of depth.

2.4 Rutherford Backscattering Spectroscopy (RBS)

Rutherford backscattering spectroscopy (RBS) is a method for determining a thin film's stoichiometry, impurity distributions, and areal density. RBS is quick, easy, and is often a non-destructive method. As well, it has modest depth resolution (10-30 nm) and the stoichiometric uncertainties are less than 1% [39]. The primary

weakness of RBS is its poor sensitivity to light elements in heavy matrices.

Typically, an RBS spectrum is acquired by accelerating light ions (^{1}H or ^{4}He) to MeV energies and allowing them to elastically collide with target atoms in the film. Through conservation of energy and momentum, the backscattered ions reflect the target atom's mass via the following expression

$$E_1 = E_o \left[\frac{\left(m_2^2 - m_1^2 \sin^2\theta\right)^{\frac{1}{2}} \pm m_1 \cos\theta}{m_1 + m_2} \right]^2 \tag{2.1}$$

where E_o is the incident ion's kinetic energy, θ is the angle through which the incident ions are scattered, and m_1 and m_2 are the incident and target atom masses. Since all other parameters are known, the mass of the target atom can be determined. Figure 2.2 illustrates how RBS can be used to determine the atoms present in an experimental geometry composed of two target atom species and their stoichiometry using Eq. 2.1.

Generally, RBS is utilized for relative measurements but the collected RBS spectrum can be simulated if a known standard sample is also measured. The standard sample permits the unique parameters of the instrumentation to be determined. A silicon substrate implanted with a known amount of bismuth was the standard sample measured to obtain the parameters for the simulation program quantitative analysis of Rutherford kinematics (QUARK) [40]. QUARK is capable of simulating the stoichiometry, areal density (if the thickness is known), and thickness (if the areal density is known). The main use made of QUARK in this work is the comparison of the simulated SRIM profile with the measured RBS spectra, discussed in section 3.3.

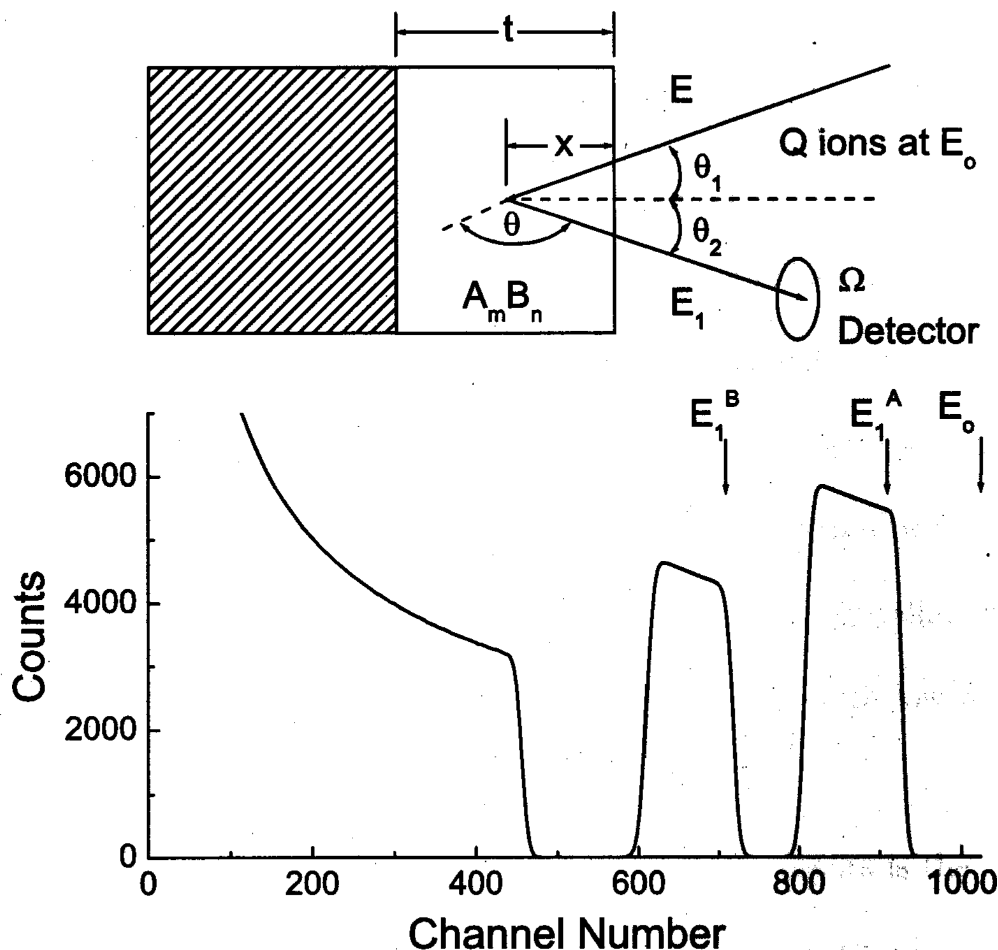

Figure 2.2: The upper image shows the experimental setup and the bottom plot shows the backscattered results [39].

2.5 Positron Annihilation Spectroscopy (PAS)

Positron annihilation spectroscopy (PAS) is a non-destructive technique that detects and differentiates between defects (e.g., vacancies, voids, etc.) and a material's chemical composition from the near surface to the bulk of the material [41, 42]. Mono-energetic positrons from a radioactive source, sodium-22 in our case, were implanted into the material and annihilated with an electron. Two or more gamma rays of approximately $m_oc^2 = 511$ keV are created in order to conserve energy and momentum. Due to the predominantly thermalized positrons, the detected gamma rays indicate the momentum distribution of the electrons in the annihilation region.

Positrons thermalize within picoseconds of entering a material and either diffuse or become trapped at defect sites until annihilating with an electron. Once within the material, positrons experience a potential due to the Coulombic repulsion of atoms and thus only interact with conduction and/or core electrons [43]. In the absence of an atom or presence of an impurity, a potential minimum occurs that attracts positrons and accounts for their sensitivity to defects. As a result, the wavefunction of a trapped positron collapses and then overlaps with that of an electron. Since a defect's electron density is lower than in a crystalline structure, significant changes occur as positrons annihilate more often with low momentum conduction electrons [43].

Another possible circumstance in which annihilation occurs is the formation of hydrogen-like bonds between a positron and electron, called positronium (Ps). Positronium generally occurs in either large, open volumes or near the material's surface where the concentration of free-electrons is low. Depending on the positron-electron spin, two forms of positronium exist: a parallel spin or para-Ps (occurs 25% of the time) resulting in the emission of 2 gamma rays and an anti-parallel spin or ortho-Ps (occurs 75% of the time) which emits 3 gamma rays [42].

Observable differences in positron annihilation of either a delocalized, trapped, or positronium state can be analyzed through several methods, such as Doppler Broadening, positron lifetime, angular correlation spectrum, positronium fraction, and centroid shift. This study relied on the Doppler Broadening spectrum method and therefore, it will be the only technique described further.

2.5.1 Doppler Broadening

The gamma rays emitted after a positron and electron annihilate emerge in approximately opposite directions and are Doppler shifted due to the momentum of the electron. The Doppler shift, plus the instrument resolution result in an overall broadening of the annihilation peak and this leads to the name Doppler broadening [41]. Two parameters are often used to describe the annihilation peak; S for "sharpness" and W for "wing". The S-parameter is defined as the number of counts in the centroid of the spectral peak divided by the total number of counts in the peak, as shown in Figure 2.3. The W-parameter refers to the number of counts in the wing region of the peak divided by the total number of counts in the peak, also shown in Figure 2.3.

A simple relationship between the S- and W-parameters exists using the Doppler Broadening method. Annihilation with a slow moving electron has the effect of narrowing the peak with more counts in the centroid, resulting in a large S-parameter value and small W-parameter value [41]. Thus, valence electrons are reflected in the S-parameter and core electrons are reflected in the W-parameter. The S and W regions are selected to obtain the best statistical results and the PAS spectrum is often normalized for comparisons between different experimental arrangements and samples.

2.6 Photoluminescence Spectroscopy (PL)

Photoluminescence spectroscopy (PL) is a technique in which a material sample is illuminated by a laser and a spectrum of light emitted from the sample is

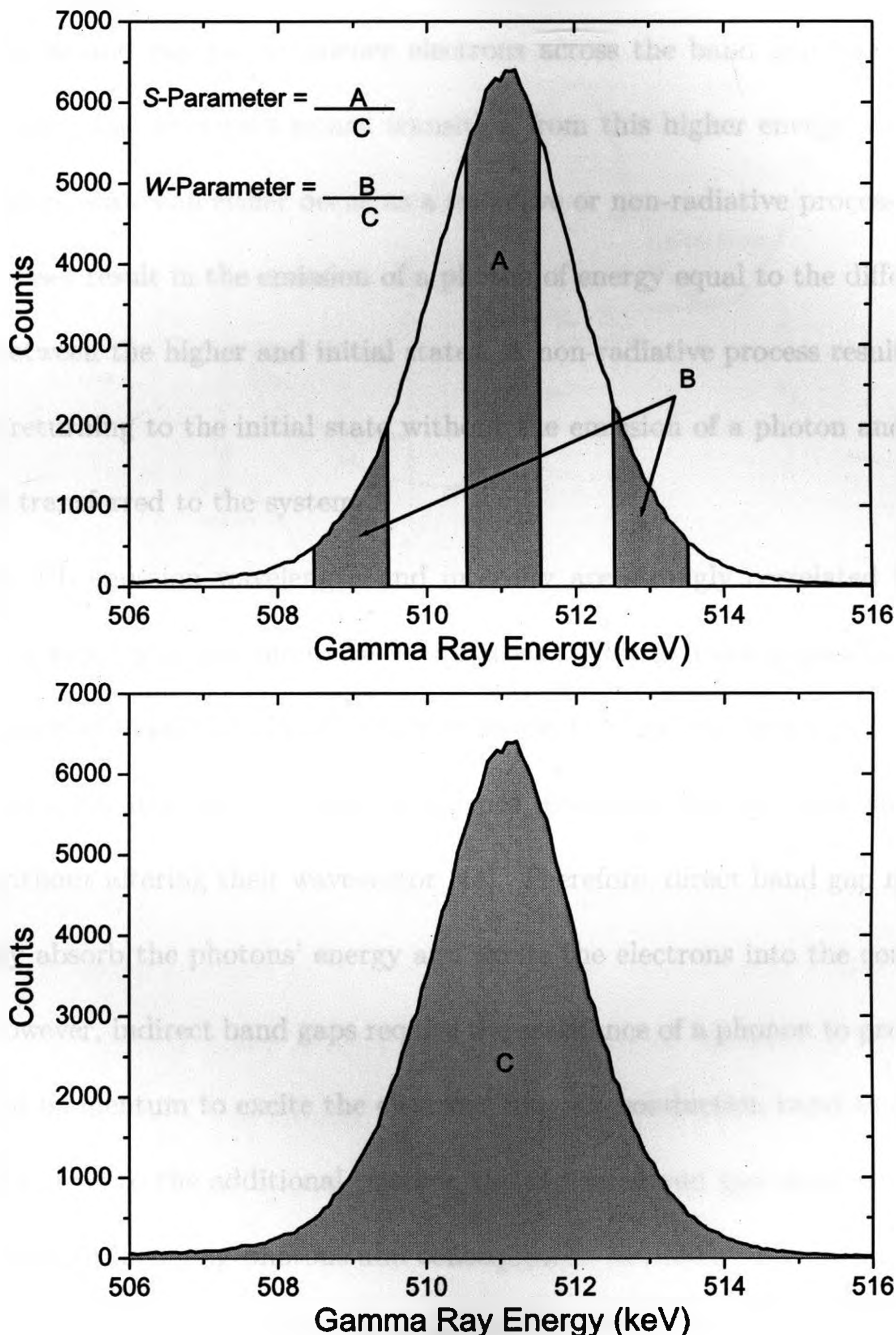

Figure 2.3: A typical gamma ray energy spectrum due to positron annihilation showing how the S- and W-parameters are calculated. The S-parameter is determined by dividing the number of counts in the centroid of the spectral peak (region A) by the total number of counts in the spectral peak (region C). The W-parameter is determined by dividing the number of counts in the wing region of the spectral peak (region B) by the total number of counts in the spectral peak (region C).

collected. The photon energy from a laser is equal to or greater than the band gap of a material and can excite valence electrons across the band gap into a higher energy state. The electron's return transition from this higher energy state to its initial energy state can either occur as a radiative or non-radiative process. Radiative processes result in the emission of a photon of energy equal to the difference in energy between the higher and initial states. A non-radiative process results in the electron returning to the initial state without the emission of a photon and heat is typically transferred to the system.

The PL emission wavelength and intensity are strongly correlated with the absorption process of the pump laser's photons. This process is greatly affected by the material's band gap being direct or indirect. Since the laser's photons have significantly less momentum than the valence electrons, the electrons absorb the energy without altering their wavevector [44]. Therefore, direct band gap materials can easily absorb the photons' energy and excite the electrons into the conduction band. However, indirect band gaps require the assistance of a phonon to provide the additional momentum to excite the electrons into the conduction band as shown in Figure 2.4. Due to the additional phonon, the indirect band gap materials are less likely to absorb incoming photons and consequently, less likely to emit photons.

An exciton is a form of absorption and is one of the probable reasons Si-nc can emit light more efficiently [7]. When electrons are excited to a higher energy state by the incoming photons, a hole is left behind in the valence band. By definition a hole is the absence of an electron and attracts the electron through Coulomb forces creating a bound hydrogen-like state. Once the exciton collapses, the electron and

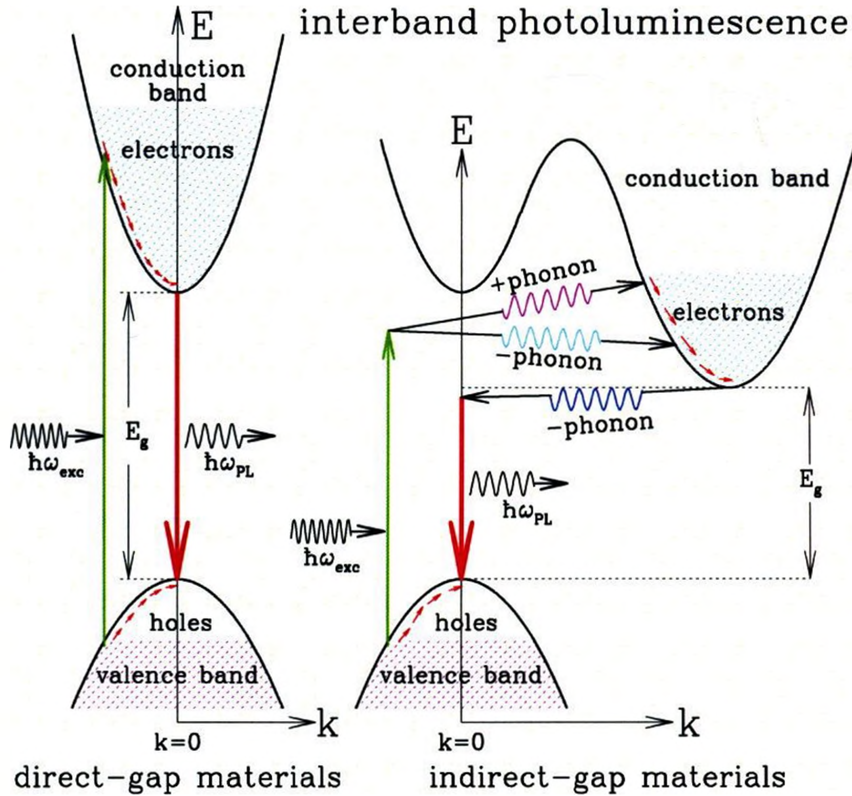

Figure 2.4: Excitation of a direct and indirect band gap material by a pump laser [45].

hole can either recombine radiatively or non-radiatively.

The majority of the PL measurements were performed at room temperature with the excitation provided by a 17 mW He-Cd laser operating at a wavelength of 325 nm. The effective power density of the pump laser on the sample was approximately 0.64 W/cm^2. The emitted light was analyzed by an Ocean Optics S2000 spectrometer with a large spectral window from 350 - 1000 nm. All of the spectra were corrected for the system response.

2.7 Cathodoluminescence Spectroscopy(CL)

Cathodoluminescence spectroscopy (CL) is a technique to excite a sample by bombarding it with electrons in the keV energy range and collect a spectrum of emitted light. A process similar to PL occurs in the excitation of electrons. The

incident electrons impart enough energy to the material's native electrons to excite them into the conduction band, which results in holes in the valence band. The excited electrons then recombine with the holes to emit a photon or return back to their original state. Exciting the valence band electrons in this manner can potentially produce defects in the material because of impact ionization.

There are typically two types of CL arrangements. The first option uses a cold cathode electron gun to supply the incident electrons and the second option has the electrons produced from a heated filament typically in a scanning electron microscope (SEM). The electron gun can usually provide higher current densities on the samples, which means the excitation or luminescence is stronger. However, this process will result in greater damage to the sample. The heated filaments in a SEM produce weaker current densities, which results in less damage and the current density can be controlled more effectively. Both types of CL arrangements were utilized in the analysis of the sample's luminescence with slight differences occurring. The results are discussed further in section 5.3.

In the first CL arrangement where the Si-nc were excited by a cold cathode electron gun manufactured by Relion Industries, the light was coupled out of the vacuum chamber by a fibre optic light guide into an Acton Spectra Pro 2150i dual grating monochrometer. The second CL arrangement excited the Si-nc by a heated filament in a Cambridge Stereoscan 200 SEM, where the light was coupled out by a fibre optic cable to an EOS spectrometer. The CL emission collected from both arrangements were not corrected for the system response, but the spectra will not be affected significantly.

CHAPTER 3

Silicon Nanocrystal Growth

3.1 Overview

The mechanism that mediates the growth and size of silicon nanocrystals (Si-nc) is important as it determines their photon emission energy and the probability that radiative transitions will occur. Through transmission electron microscopy (TEM), Rutherford backscattering spectroscopy (RBS) and positron annihilation spectroscopy (PAS), the growth of Si-nc was determined to be affected by the vacancy-type defect distribution introduced through the implantation process. This chapter describes and discusses the results obtained from the three techniques mentioned above, the correlation between the growth and vacancy-type defect distribution, and an experiment supporting that correlation.

It also needs to be mentioned that the annealing gas affects the growth of Si-nc and this will be briefly discussed. The most common gases used during the annealing process are nitrogen and argon. At temperatures greater than 1000°C, nitrogen can dissociate and be incorporated into the film's chemistry, while argon remains inert. The incorporation of nitrogen is likely to create an oxynitride film on the Si-nc surface, which has the effect of maintaining the nanocrystals' size after the initial growth [46]. Conversely, argon allows the continued growth of the nanocrystals, but at a slower rate.

3.2 Transmission Electron Microscopy (TEM)

Transmission electron microscopy (TEM) is a technique to observe materials on a small scale. Particles were observed in the TEM images, and the composition of the particles was determined to be silicon by energy dispersive X-ray spectroscopy (EDX) and electron energy loss spectroscopy (EELS). The effects of the electron beam on the sample used to obtain the TEM images was also investigated and concluded to be negligible. Therefore, the TEM images were capable of yielding the size distribution of the Si-nc as a function of depth within the oxide film. The size distribution indicated a correlation between vacancy-type defects and Si-nc size.

3.2.1 Sample Composition

The chemical composition of particles detected in regions suspected of containing Si-nc must be determined. The particles' composition was ascertained through two methods in the TEM environment. The first method, energy dispersive X-ray spectroscopy (EDX) was utilized to analyze the different SiO_x film regions and allowed for a loose identification of the elements present. The other method, electron energy loss spectroscopy (EELS) was used to directly determine whether the particles were composed of silicon. The analysis stemming from these two methods resulted in an identification of silicon particles in the TEM images. The specific process for identifying the sample composition is given below.

The analysis was initiated by analyzing the different elements present in the film using EDX, which examines characteristic X-rays of atoms. An example EDX spectrum taken from near the surface of the oxide layer is illustrated in Figure 3.1

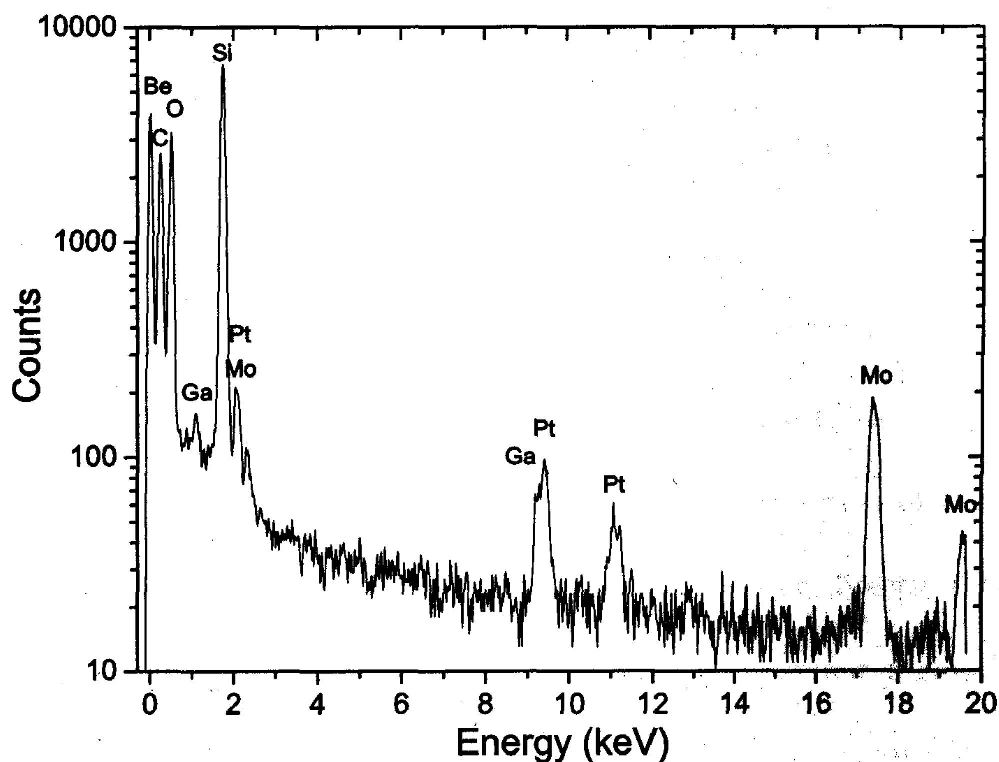

Figure 3.1: Energy dispersive X-ray spectrum of the SiO_x film near the surface.

and the compositions are summarized in Table 3.1. There were seven atomic species present in the film: Be, C, O, Si, Ga, Mo, and Pt. Although Be and Mo atoms should not be present in the film, they were detected by EDX because scattered electrons from the film interacted with the Be TEM sample stage, and from both the Mo nanomanipulator holding the sample and the rings clamping the nanomanipulator to the TEM stage. Similarly, C is present throughout the TEM system making it difficult to distinguish between the sample and the environment. Consequently, Be, Mo and C were excluded from Table 3.1 and the majority of the remaining material was composed of O and Si, with trace amounts of Ga and Pt. The trace amounts of Ga are due to the ion beam used to thin the TEM sample and the Pt is due to the protective layer deposited before the thinning of the TEM sample. Thus, the concentration of C, and particle composition (O, Si or C) required further analysis.

Table 3.1: Atomic percentage of elements present in different regions of the SiO_x film using energy dispersive X-ray spectroscopy (EDX).

	O (%)	Si (%)	Ga (%)	Pt (%)
Near the Surface	63.10	36.34	0.24	0.32
Middle of the film	65.48	34.31	0.07	0.15
SiO_2/Si interface	65.27	34.56	0.13	0.05

Given that the possible elements in the sample were ascertained through EDX, EELS was utilized to determine the actual elemental composition of the sample's particles. EELS analyzes the energy lost by electrons passing directly through the sample, which make it sensitive to the elements in a particular region. EELS's sensitivity to the presence of carbon in the material is greater than EDX and the amount of carbon was determined to be negligible. As such, the particles were either composed of oxygen or silicon or a combination of the two. To distinguish between the two species in the TEM images, a small energy window of 4 eV was moved from the silicon plasmon peak to the oxygen plasmon peak. The modification in the window's position was evident at the interface between the SiO_2 and Si by an inversion of the image's grey scale as shown in Figure 3.2. The same effect occurred in the region where nanocrystals were observed. Therefore, the particles observed in the TEM images were composed of silicon and only the effects of the electron beam on the sample needed to be established.

3.2.2 Electron Beam Effects

Electron beam damage must be discussed when employing TEM because at high doses of electron irradiation SiO_2 can lose oxygen, the silicon can aggregate

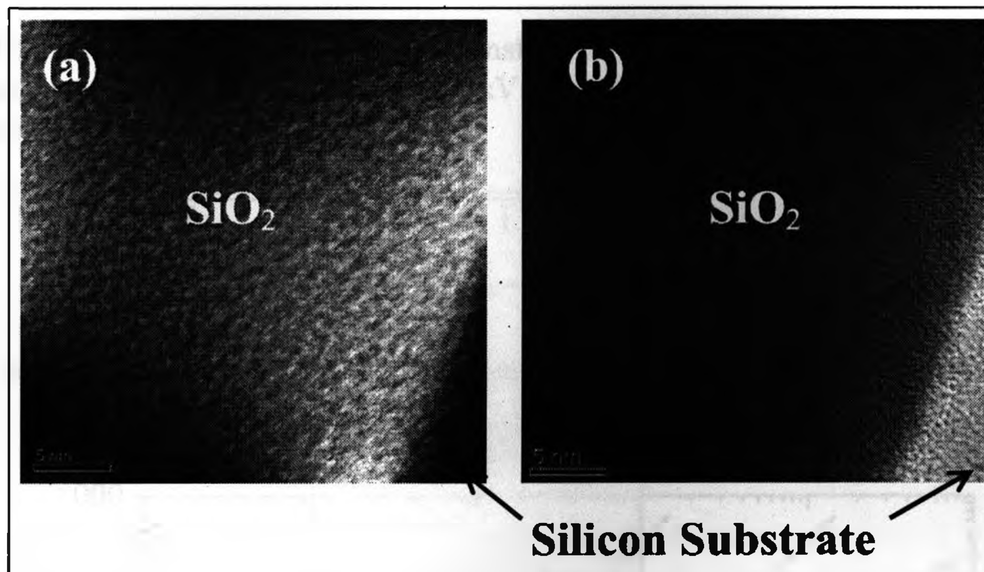

Figure 3.2: EELS with a 4 eV window centered on (a) the silicon plasmon peak of 17 eV, and (b) the SiO_2 plasmon peak of 22 eV.

through heating of the sample [47], atoms can be displaced due to the high energy, and material can be sputtered from the surface [38]. Sample heating was not a concern because the field emission gun (FEG) only heats SiO_2 by less than 1 Kelvin, as shown in Figure 3.3, which is not enough heat to affect the growth and size of the Si-nc. At an acceleration voltage of 200 kV, the electrons' maximum transferable kinetic energy can impart enough energy to displace and sputter both silicon and oxygen atoms (summarized in Table 3.2). The maximum transferable kinetic energy was calculated using the following expression [48]:

$$E_{max} = \frac{2m_a E\left(E + 2m_e c^2\right)}{\left[\left(m_a + m_e\right)^2 c^2 + 2m_a E\right]}$$

where m_a is the atomic mass, m_e is the mass of an electron, c is the speed of light, and E is the accelerating voltage. Therefore, the beam's effects were tested by exposing a region in the oxide layer to 200 pA/cm^2 for more than two minutes, which imparts a dose greater than 2.4×10^{-8} C/cm^2. A subtle change in the contrast was observed

Table 3.2: Comparison of maximum transferable kinetic energy (E_{max}) with the displacement and sputtering energies at 200 kV. The displacement and sputtering energies were taken from SRIM [37].

Element	E_{max} (eV)	Displacement Energy (eV)	Surface Binding Energy (eV)
Si	18.68	15	4.71
O	32.79	28	2

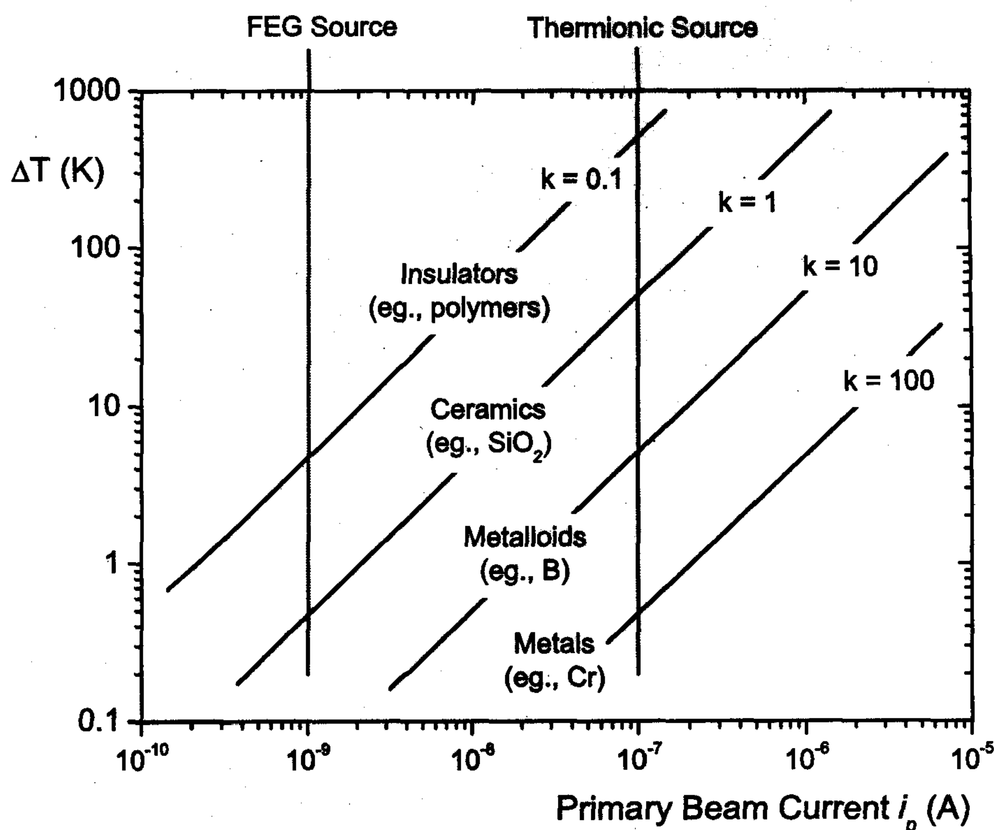

Figure 3.3: The increase in temperature of the specimen as a function of the specimen's thermal conductivity k [$Wm^{-1}K^{-1}$] and the beam's current [38].

in the exposed region of Figure 3.4. However, it would have taken 16 hours to impart the same dose with the 0.4 pA/cm^2 flux used to capture the TEM images. As well, both EDX and EELS measurements were performed after the TEM images were taken, which reduced the exposure to the sample further. Therefore, the beam's damage on the sample would not have significantly affected the TEM images and the silicon particle size distribution could be analyzed.

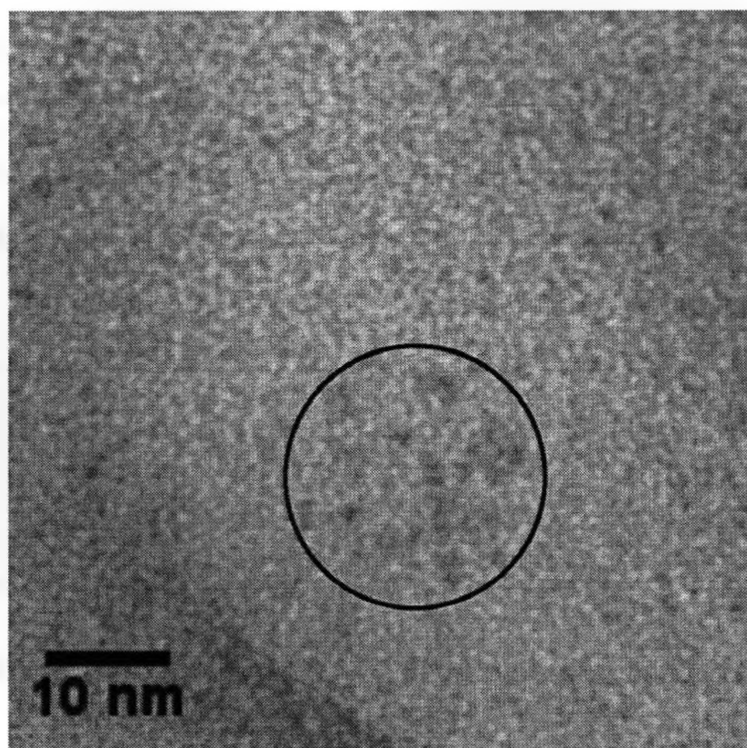

Figure 3.4: Damage caused by the electron beam at 200 pA/cm^2. The damaged region is contained within the circle.

3.2.3 Silicon Nanocrystal Size and Location

The location and distribution of Si-nc was determined by collecting and analyzing TEM images from consecutive depths within the sample. The mean and median Si-nc sizes were calculated from two different regions to enhance the statistical analysis. Particles were rejected from the analysis if they lay on the image's border or if their circularity was not between 0.5 and 1 (where 1 is a perfect circle). A circularity of 0.5 was chosen in order to reject particles that overlapped from the analysis. Typically 3 to 4 particles were rejected per TEM image containing approximately 60 particles. Table 3.3 summarizes the mean and median Si-nc sizes as a function of depth where each TEM image covers approximately 30 nm × 30 nm, and the image sequence is outlined in Figure 3.5. The Si-ncs increase in size the further they are from the sample surface until 135-180 nm (image 4), after which

Table 3.3: Median and mean Si-nc size as a function of depth for a 430 nm thick oxide layer implanted with 1.4×10^{17} silicon ions/cm^2 (20 at.% excess Si) and annealed at 1070°C for 3 hrs. The TEM image locations are illustrated in Figure 3.5, and the uncertainty in the mean diameter is the standard error and not standard deviation.

TEM Image Location	SiO_x Depth (nm)	Median Si-nc Diameter (nm)	Mean Si-nc Diameter (nm)
1	0 - 45	1.71	1.77 ± 0.05
2	45 - 90	1.79	1.82 ± 0.05
3	90 - 135	1.82	1.86 ± 0.05
4	135 - 180	1.61	1.67 ± 0.04
5	180 - 225	Too small to distinguish	

depth the size decreases. By image 5, the Si-ncs are too small to distinguish and in the unimplanted oxide region (beyond ~250 nm) no Si-nc are visible, which either means that there are no Si-ncs or that they are much smaller than 1 nm.

In view of the relatively small diffusivity of silicon in SiO_2 [49], these results are surprising since one might reasonably anticipate that the Si-nc distribution would follow the Si ion implantation profile. Examining Figure 3.5(a), it would be expected that regions 3 and 4, and regions 2 and 5 exhibit a similar concentration and size of Si-nc due to a similar density of implanted silicon. However, Table 3.3 demonstrates that this is not the case. To explain the existence of such large Si-nc near the surface of the sample requires consideration of factors other than the density of implanted silicon. Ion implantation creates defects of various types in SiO_2, including vacancy-type defects and vacancy clusters, which decrease in concentration with increasing annealing temperature and time. The vacancy-type defect and implantation profiles simulated by SRIM are plotted in Figure 3.5(a). These profiles reveal that the primary vacancy-type defect distribution is broader than the implanted ion

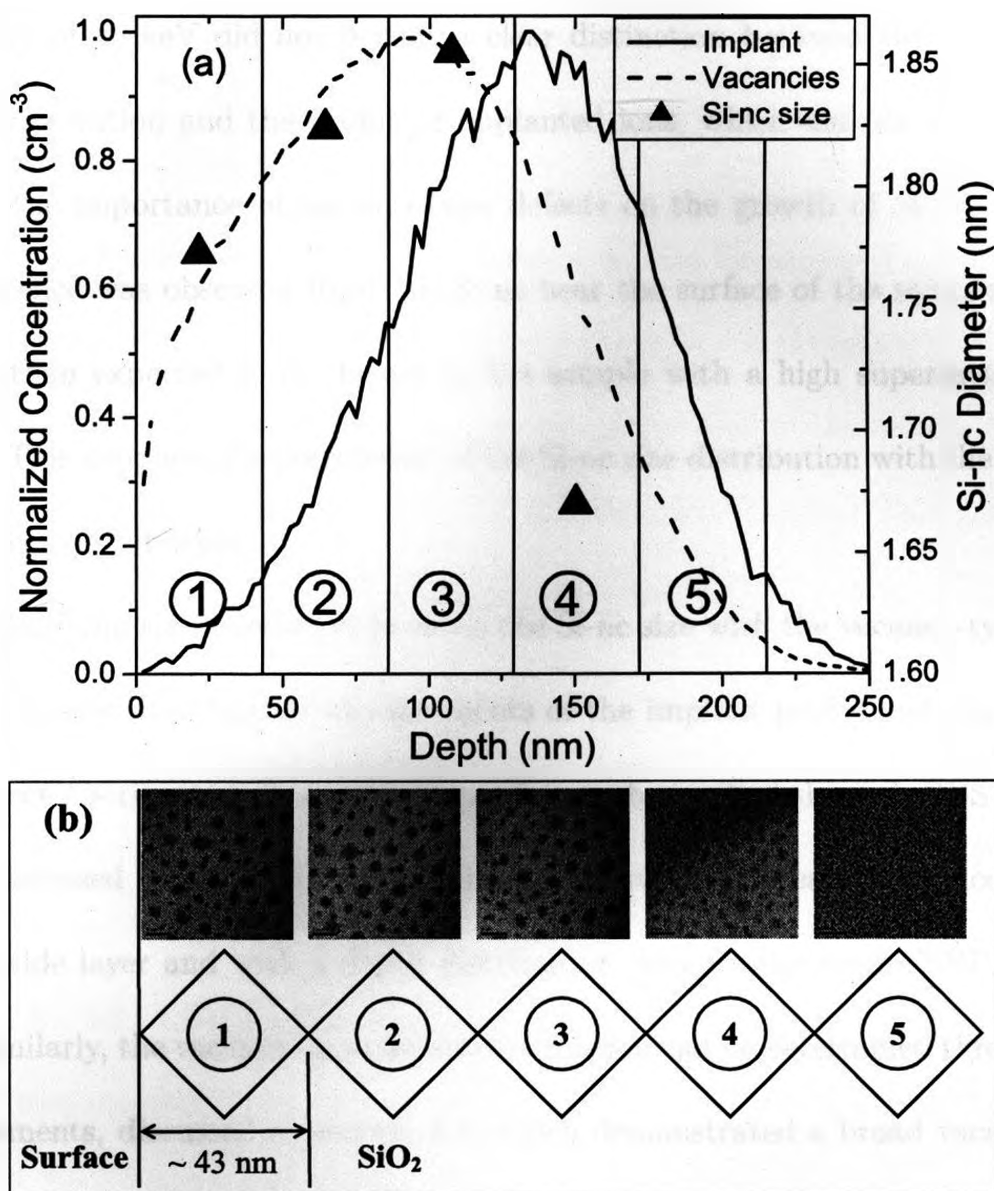

Figure 3.5: (a) SRIM simulation of the implantation and vacancy-type defect distributions for a 90 keV implant plotted along with the mean size of the Si-nc determined from TEM. (b) TEM images including an outline indicating their location and orientation relative to the oxide film and the surface. The TEM samples were implanted at 90 keV to a dose of 1.4 $\times$ 10^{17} ions/cm^2, and annealed at 1070°C for 3 hrs.

distribution and reaches its peak concentration closer to the surface.

In Figure 3.5(a), a strong correlation between the distribution of vacancy-type defects and the distribution of Si-nc is observed. Similar results of Si-nc in close proximity to a sample's surface were observed by Brongersma *et al.* through a process of iterative PL measurements and etching [50]. Their Si^+ implant at

an energy of 35 keV did not permit a clear distinction between the vacancy-type defect distribution and the profile of implanted ions, which did not allow them to observe the importance of vacancy-type defects on the growth of Si-nc. However, luminescence was observed from: (i) Si-nc near the surface of the sample; and (ii) smaller than expected Si-nc deeper in the sample with a high supersaturation of silicon. This supports the correlation of the Si-nc size distribution with the vacancy-type defect distribution.

Solidifying the correlation between the Si-nc size with the vacancy-type defect distribution required further measurements of the implant profile and the vacancy-type defect distribution. The implant profile can be verified through RBS measurements discussed in the next section, which confirmed the presence of excess silicon in the oxide layer and with a depth distribution very similar to the SRIM simulation. Similarly, the vacancy-type defect distribution can be determined through PAS measurements, discussed in section 3.4, which demonstrated a broad vacancy-type defect distribution centred around 100 nm (consistent with SRIM).

3.3 Rutherford Backscattering Spectroscopy (RBS)

The stoichiometry of the films was examined by Rutherford backscattering spectroscopy (RBS). In particular, the silicon ion distribution before and after annealing was compared to the simulations obtained by SRIM through the modeling program QUARK [40]. The results from QUARK demonstrated the consistency between the simulated SRIM ion distribution and RBS measurements. Also, negligible change in the ion distribution occurred after annealing the sample, which is

consistent with the small diffusivity of silicon in SiO_2 [49].

3.3.1 Silicon Ion Distribution

The RBS measurements were performed on the films after every processing stage in order to observe the stoichiometric changes. In Figure 3.6, observable differences occurred in the silicon and oxygen composition of the SiO_2 between the reference sample and both the implanted and annealed samples. This difference is the result of the implantation of silicon ions into the oxide, which can be simulated by SRIM.

Incorporating the SRIM simulation into the QUARK modeling program resulted in excellent agreement with the RBS experiments (Figure 3.6). Subtle differences in the thickness of the films were evident by ellipsometry measurements but were harder to distinguish in the RBS results. Therefore, one sample partially masked from the implantation was produced in order to measure the film expansion, by atomic force microscopy (AFM). It was established that the implanted side was approximately 6 nm thicker than the non-implanted side, thus the sputtering from the film was not significant. As well, the difference between Figure 3.6 (b) and (c) in the implanted region is minimal, which is expected due to the small diffusivity of silicon in SiO_2 [49]. Thus, the simulated SRIM profile of the silicon ion distribution predicted the experimentally measured implanted silicon ion distribution very well.

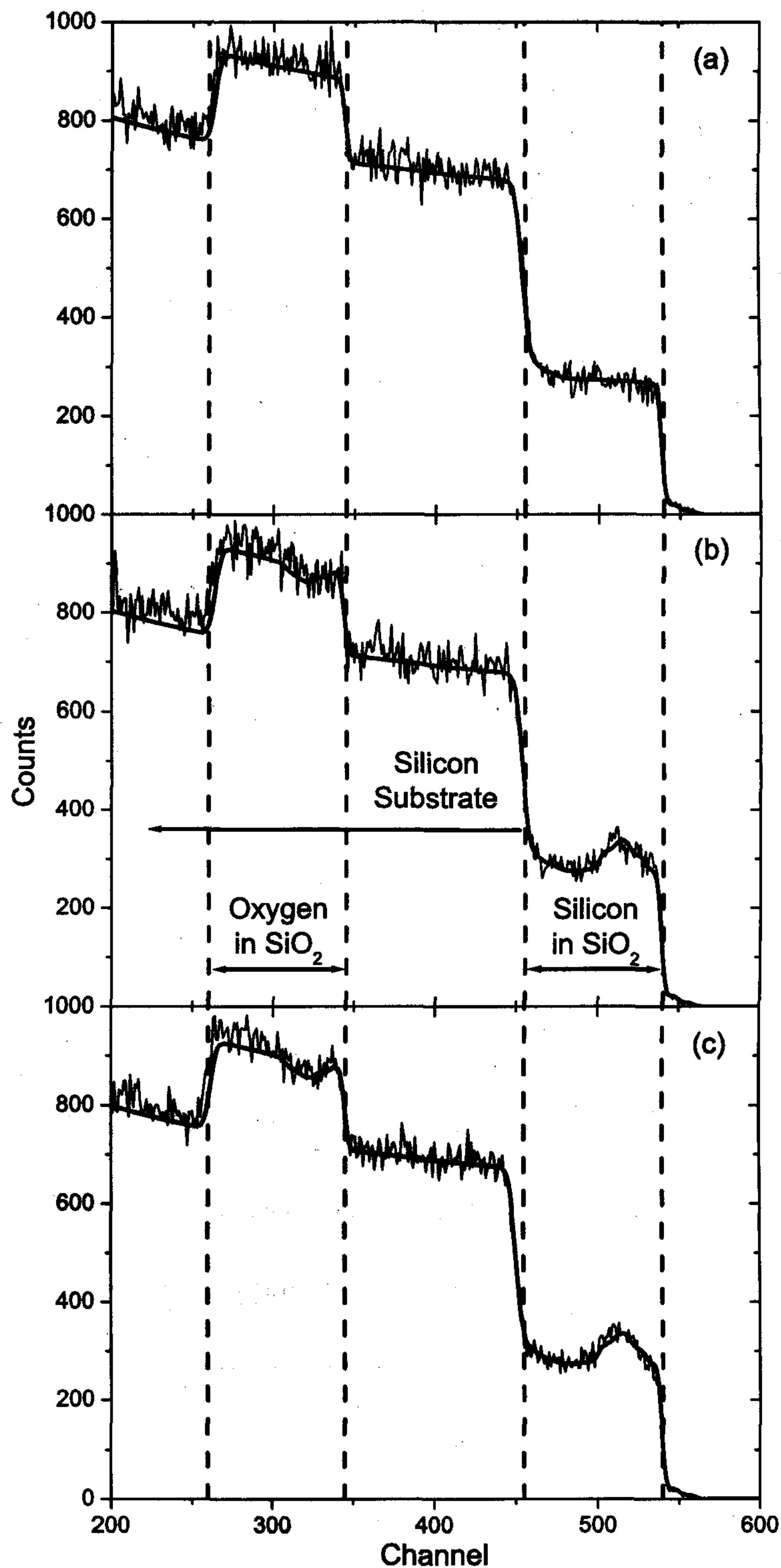

Figure 3.6: The RBS measurements were performed with a 2.25 MeV $^4He^+$ beam. The noisy curves are the experimental results and the smooth curves are the QUARK models. The samples were implanted at 90 keV and a dose of 1.4×10^{17} ions/cm^2. (a) is the reference SiO_2, (b) is the implanted sample where the QUARK model uses the SRIM simulated implantation profile, and (c) is the implanted sample after it has been annealed.

3.4 Positron Annihilation Spectroscopy (PAS)

The vacancy-type defect distributions were probed by positron annihilation spectroscopy (PAS). The PAS results confirmed the SRIM simulated vacancy-type defect distribution. As well, both PAS and PL measurements provided additional evidence regarding the role of vacancy-type defects in the formation of Si-nc with the concomitant rapid reduction of defects and rapid growth of Si-nc. These results would indicate that the vacancy-type defects facilitate the silicon atom diffusion required for the growth of Si-nc.

3.4.1 Vacancy-Type Defect Distribution

Defect distributions of implanted material can be qualitatively measured using PAS. There are several defect species that can be formed in SiO_2 by ion implantation [51]: peroxy radicals; E' centres; non-bridging-oxygen hole centres (NBOHC); and vacancy-type defects. Peroxy radicals are most often observed in oxygen rich SiO_2, making them less likely to be detected in a silicon rich film [52]. However, E' centres are most often found in silicon rich SiO_2 [53], but they are positively charged and therefore, very inefficient at trapping positrons. The final two defect types, NBOHC and vacancy-type, are the result of the implanted ions' two stopping mechanisms, electronic and nuclear [54].

Initially, the implanted silicon's ionization effect (i.e., electronic stopping) knocks off valence electrons creating NBOHC defects, which reduce the S-parameter value due to the lack of valence electrons and the annihilation of positrons with oxygen core electrons [55]. Such results have been observed by Knights *et al.* [56] for a

Table 3.4: Electronic and nuclear stopping powers for different silicon implant energies tabulated by SRIM.

Energy (keV)	$\frac{dE}{dx}$ Electronic ($MeV{\cdot}cm^2/mg$)	$\frac{dE}{dx}$ Nuclear ($MeV{\cdot}cm^2/mg$)
25	0.6411	1.936
50	0.9067	1.683
90	1.255	1.387
100	1.317	1.330
250	1.804	0.8553
500	2.674	0.5657
1000	4.635	0.3556
1500	6.279	0.2661

high energy implant of 1.5 MeV where the dominant stopping power was electronic (see Table 3.4). Finally, the implanted silicon knocks other atoms away from their location (i.e., nuclear stopping), which leaves vacancy-type defects that increase the S-parameter because in open-volumes the positrons have a higher probability of encountering slow moving valence electrons [55]. If the vacancy-type defect is large enough, positronium can form and be observed [41].

The majority of the implants were performed at 90 keV, where the two stopping mechanisms were roughly equivalent as shown in Table 3.4, which indicates that both types of defects should be present and affect the S-parameter value. In Figure 3.7, PAS measurements for three different implant doses demonstrated an S-parameter value greater than the initial material, and which increased with ion dose. As well, Figure 3.8 demonstrated that the raw data spectrum for the as-implanted sample had a higher peak in the S-parameter window and a lower peak in the W-parameter window compared to the reference SiO_2 film. These results indicate that the positrons are annihilating with slower moving valence electrons and less with

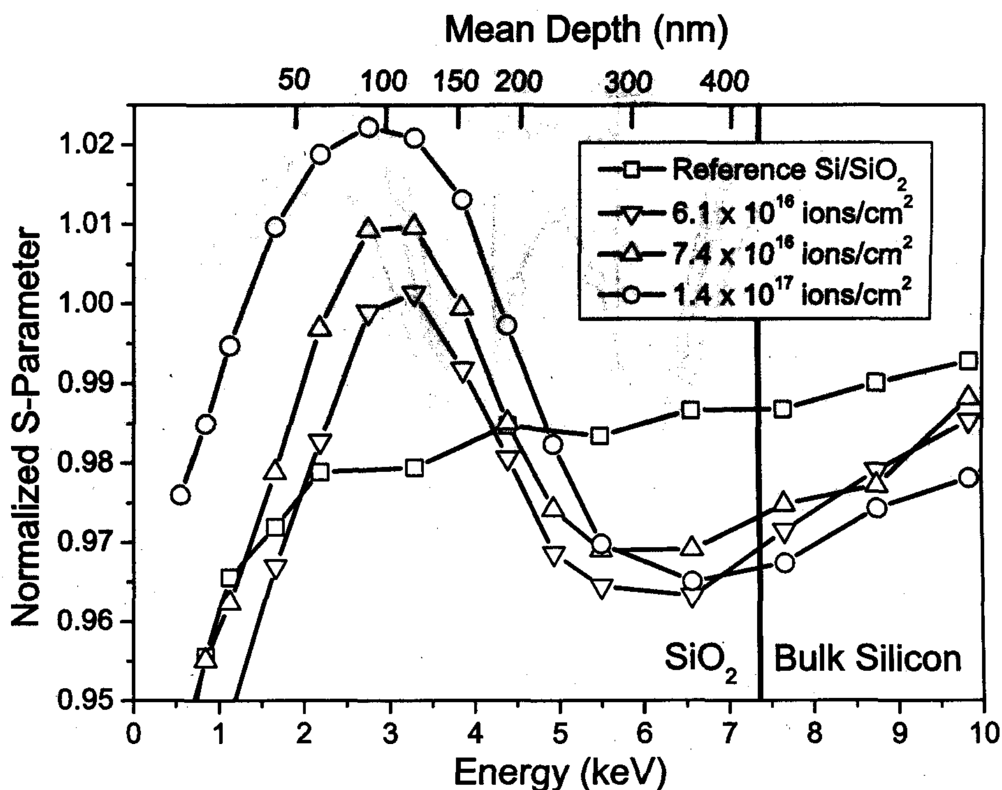

Figure 3.7: S-parameter results of as-implanted samples implanted at 90 keV and various doses in a 430 nm thick SiO_2 film. The lines are to guide the eye.

core electrons, which is characteristic of vacancy-type defects. Ghislotti *et al.* [52] performed a comparable experiment with similar results at high doses, but at lower implant doses they measured a decreased S-parameter value, signifying the presence of NBOHC defects. Nonetheless, the results at lower doses from Ghislotti *et al.* [52] still possessed a distribution of S-parameter value versus depth of similar shape and location to the vacancy-type defect distribution.

It was suggested by Ghislotti *et al.* [52] that the distribution and the increased S-parameter value for high ion doses was related to the higher concentration of Si-atoms. The PAS and RBS measurements contradict this suggestion. In Figure 3.9, a dramatic reduction in the S-parameter value occurred after a 10 s anneal. This result does not reflect the consistency in stoichiometry of the material between the

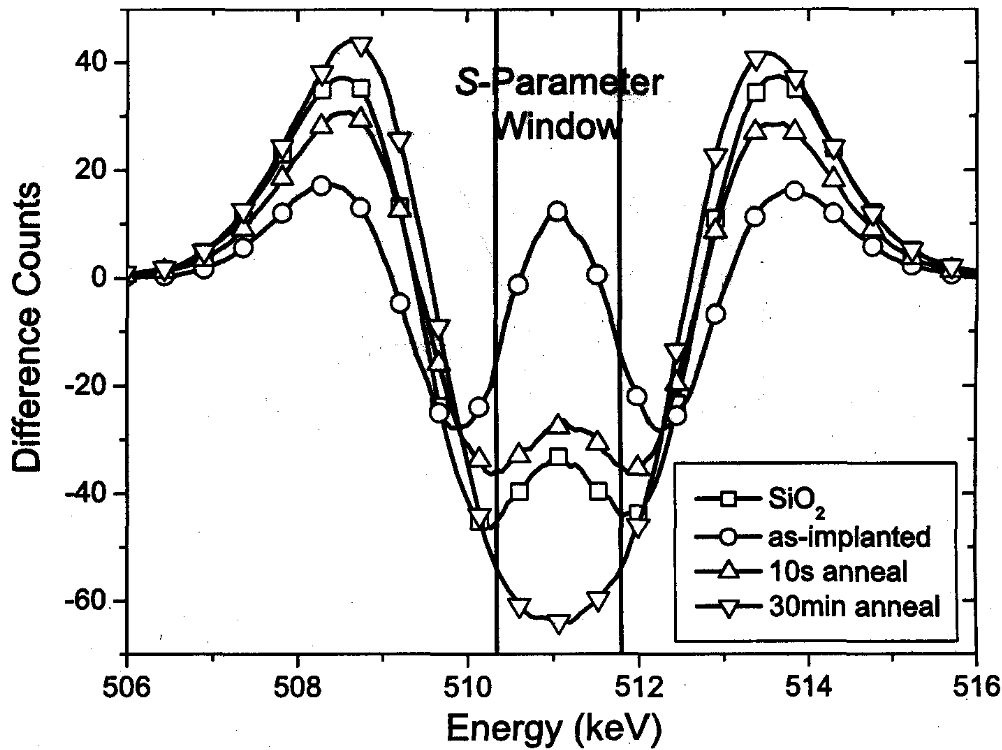

Figure 3.8: Raw data spectrum at 3 keV comparing the reference SiO_2 with the as-implanted, 10 s anneal and 30 min anneal at 1170°C of a sample implanted with a dose of 1.4×10^{17} ions/cm^2. The data have been smoothed for clarity.

as-implanted and annealed samples (Figures 3.6 (b) and (c)). As well, in the PAS measurements the peak is located approximately at 100 nm, which is closer to the depth of the peak vacancy-type defect concentration than the peak ion concentration. Therefore, the change in the S-parameter is likely not stoichiometry related but vacancy-type defect related.

The present data demonstrate that the location and size distribution of Si-nc closely resembles the distribution of vacancy-type defects rather than the profile of the implanted Si ions. This suggests that the Ostwald ripening process, where larger Si-nc grow at the expense of smaller ones [58], may be mediated by vacancy-type defects. The relationship between ripening and vacancy-type defects can be inferred through the PL and PAS measurements. Figure 3.9 illustrates the positron

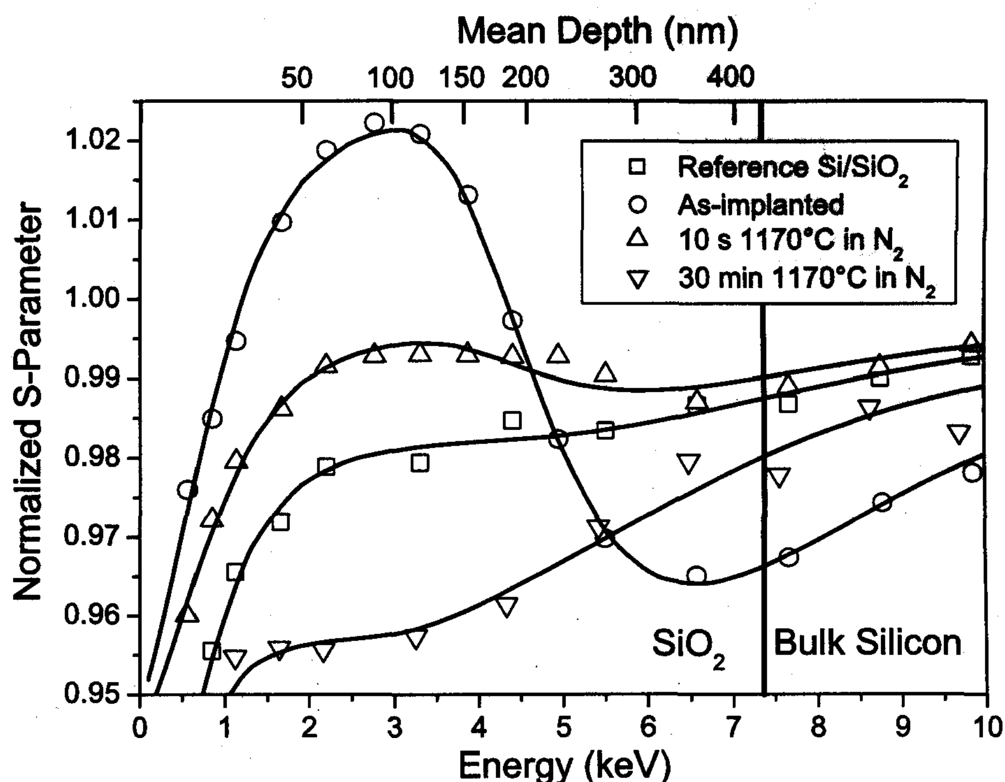

Figure 3.9: S-parameter results showing the reduction of vacancy-type defects after a short anneal time and the appearance of Si-nc after a longer anneal time in a 430 nm thick SiO_2 film implanted at 90 keV and a dose of 1.4×10^{17} ions/cm^2. The lines are fitted results of the collected experimental data using POSTRAP5 [57] and the model is discussed in Appendix A.

annihilation S-parameter value versus mean positron implantation energy and depth for samples at various processing stages. The S-parameter value decreases from 1.02 to 0.99 after a 10 s anneal at 1170°C. The lower value approaches the S-parameter value of the SiO_2 prior to implantation, denoting a rapid reduction in the concentration of vacancy-type defects.

PL measurements demonstrate the concomitant and rapid evolution of Si-nc at the high temperature. The data presented in Figure 3.10 reveal that the peak wavelength, an indication of the Si-nc size, does not change significantly beyond 2 minutes of annealing. Garrido Fernandez *et al.* observed similar rapid precipitation or formation of Si-nc using Fourier transform infrared spectroscopy and x-ray

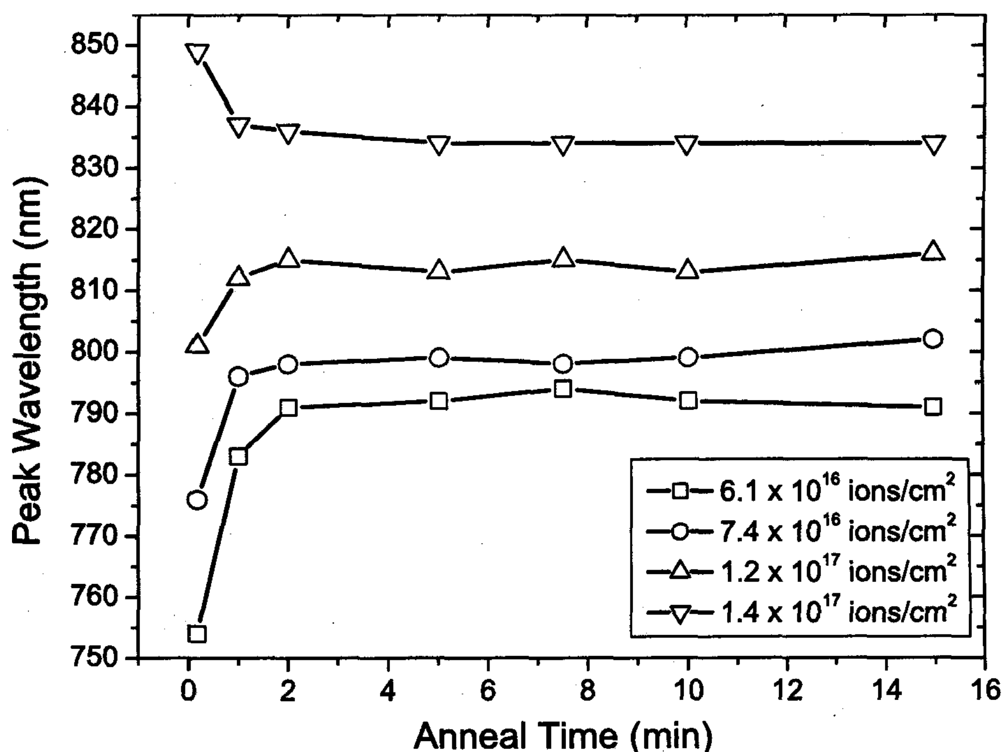

Figure 3.10: Progression of the photoluminescence peak wavelength for various implant doses. The apparent blue shift in the peak PL wavelength from 10 s to 2 min for the 1.4 $\times$ 10^{17} ions/cm^2 sample is not reliable and is due to the progressive increase in detector noise above 800 nm, which skews the peak PL wavelength to a higher value for very low intensity samples.

photoelectron spectroscopy [59]. The results parallel the behaviour of the PAS S-parameter (i.e., a significant change during short annealing times). The correlation between the rapid reduction in vacancy-type defect concentration observed in the PAS measurements and the stabilization of peak PL wavelength after only 2 minutes of annealing, is once more consistent with the suggestion that vacancy-type defects play a significant role in the formation of Si-nc. One possible mechanism for this correlation is that vacancy-type defects facilitate the silicon atom diffusion required for ripening of the Si-nc.

Since it has been established that the PAS results are associated with vacancy-type defects, the results must be compared to the SRIM simulated vacancy-type

defect distribution shown in Figure 3.5. The SRIM simulation and PAS measurements are plotted in Figure 3.11 and produce comparable distributions and correlated peaks. The simulation and measurement data are similar on the left side of the distribution and deviate on the right side. Nevertheless, the slight deviation on the left side is likely due to the positrons diffusing to the surface at low positron implant energies, thus lowering the S-parameter value. The deviation on the right side of the distribution is likely attributed to a combination of two factors. First, as the positron implant energy increases, the positron depth distribution broadens and the S-parameter is sampled from a wider region of the film. Secondly, the large number of vacancy-type defects near the surface of the film trap more positrons than the unimplanted SiO_2. Therefore, as the positron implant energy increases, the broadly distributed positrons are more likely to annihilate in the region containing vacancy-type defects rather than in the unimplanted region. This would generate a wider tail on the right side of the S-parameter distribution results.

Based on the PAS measurements and analysis presented above, the observed distribution is due to vacancy-type defects. As well, the concomitant rapid evolution of the vacancy-type defects and PL peak wavelength further supports the correlation of the Si-nc size with the vacancy-type defect distribution.

3.5 Verifying Vacancy-type Defect Correlation

If the hypothesis regarding the role of vacancy-type defects in Si-nc growth is correct, it should be possible to manipulate the emission properties of Si-nc contained within an oxide matrix via defect engineering. To test this hypothesis, three

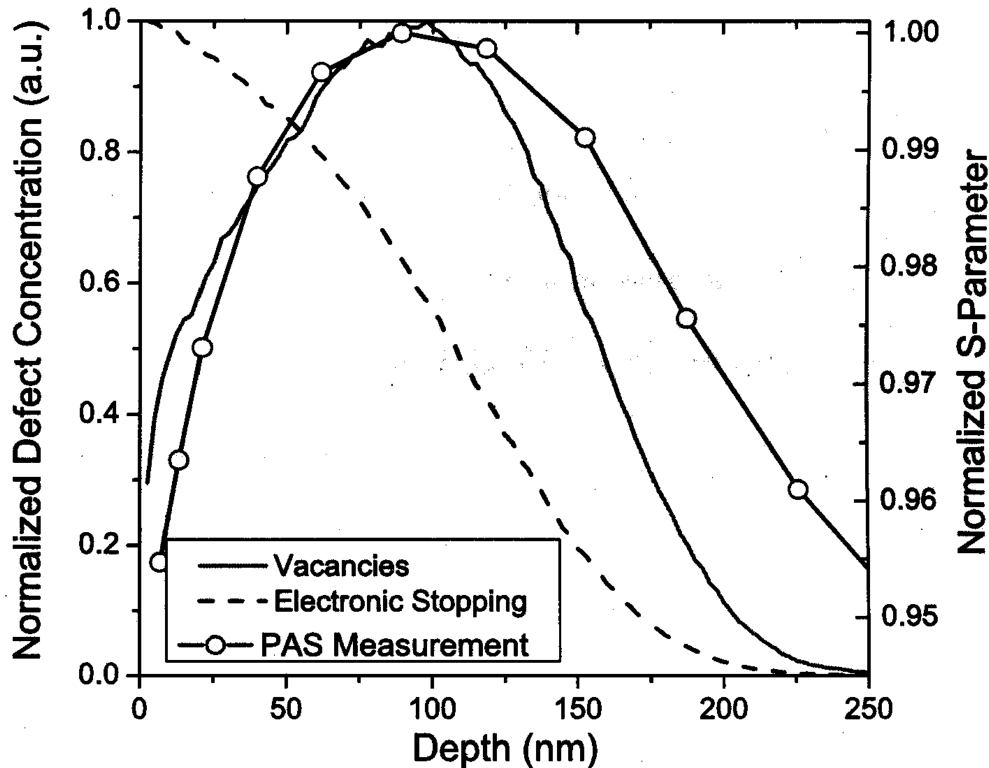

Figure 3.11: SRIM simulation of the vacancy-type defect profile (nuclear stopping) and ionization (electronic stopping), and PAS measurement for a 430 nm SiO_2 film implanted at 90 keV. The PAS results are from a sample implanted with a dose of 1.4×10^{17} ions/cm^2. The depth for the PAS measurement is the mean depth of the implanted positrons and not an absolute depth.

samples were prepared using implantation of a 965 nm thick SiO_2 film. Sample *A* was prepared using a single Si ion implant with a projected range of 650 nm (implantation energy of 450 keV and a fluence of 1×10^{17} ions/cm^2), while sample *B* had the Si ions implanted at a shallower projected range of 130 nm (implantation energy of 90 keV and a fluence of 3×10^{16} ions/cm^2). The third sample, *C*, was implanted first at an energy of 450 keV and then at 90 keV, with the same doses as for samples *A* and *B*. The SRIM simulated profiles of the implanted Si ions and the associated vacancy-type defects are shown in Figures 3.12(a) and (b). All three samples were annealed in nitrogen at 1070°C for 3 hrs and passivated at 450°C in forming gas. Forming gas passivates the interface with hydrogen and allows the

quantum confinement emission to be the dominant emission characteristic [33].

Depending upon the mechanism driving the growth of the Si-nc, the following three statements regarding the emission properties of the samples can be made: (i) if the size, number, and location of the Si-nc were determined solely by the implanted Si ion profile, then the sum of the PL spectra from the two control samples, $A + B$, should resemble the spectrum for the dual implanted sample C. The results would be due to the low diffusivity of silicon and the separation of the implant profiles in Figure 3.12(a), in essence making them independent of one another;
(ii) if vacancy-type defects impact the growth of Si-nc, then in sample C the PL shape should be comparable to sample A and the intensity should increase compared to sample A. This would be a direct consequence of the number of vacancy-type defects in the 90 keV implanted region shown in Figure 3.12(b) doubling to a concentration similar to the 450 keV implantation region or the Si-nc size distribution being comparable in both regions;
(iii) if statement (ii) is correct, then the peak emission wavelength for sample C should red-shift compared to sample B but be limited in its red-shift to a value less than the peak wavelength for sample A, because the peak vacancy-type defect concentration in the 90 keV region of sample C is less than the peak vacancy-type defect concentration in the 450 keV region.

The PL results shown in Figure 3.12(c) and summarized in Table 3.5 indicate that the PL intensity for sample C is nearly twice that of sample A, with a similar shape to sample A in accord with statement (ii). Further, the peak wavelength shifted according to the arguments presented above in statement (iii). However,

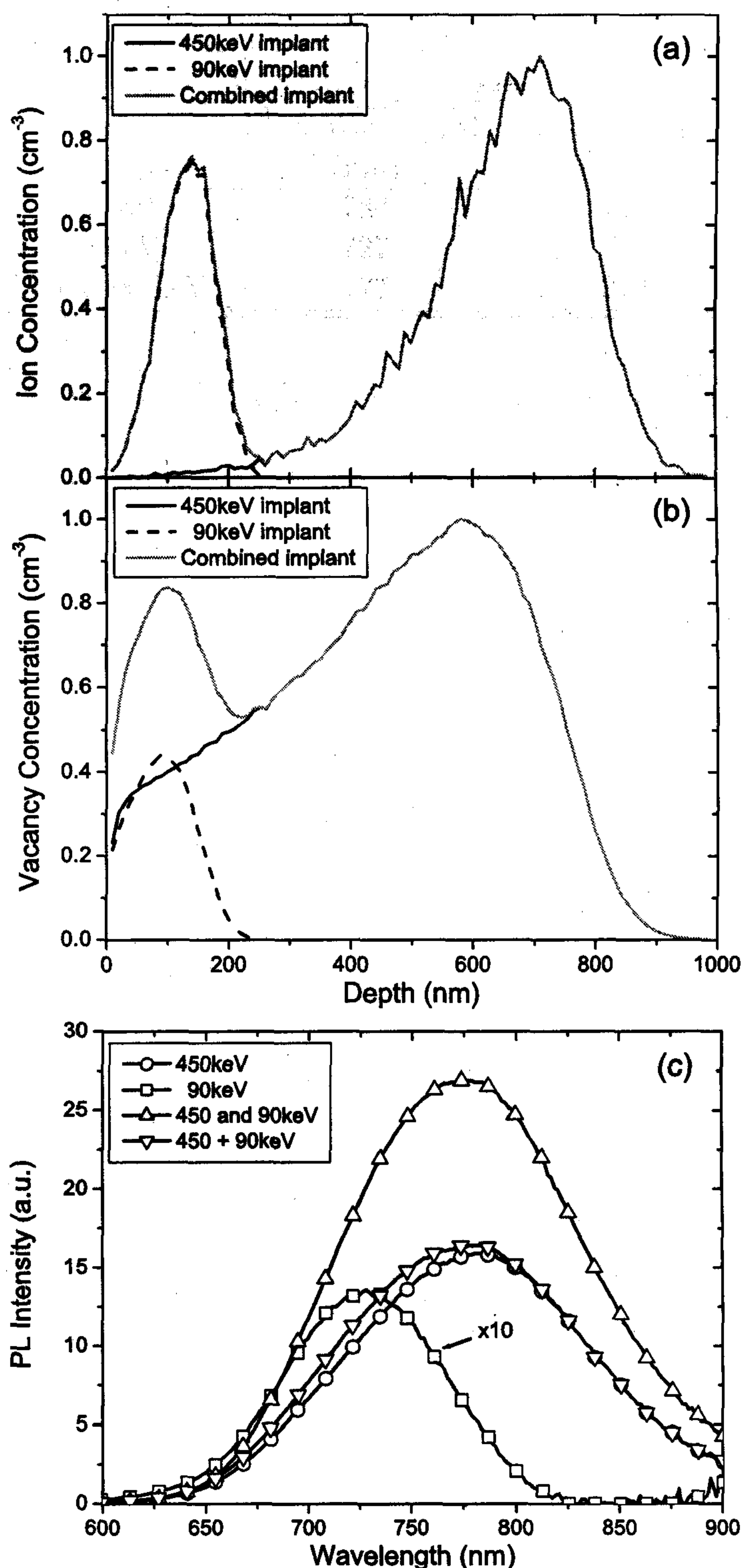

Figure 3.12: SRIM simulations of a 450 keV implant at 1×10^{17} ions/cm^2 and a 90 keV implant at 3×10^{16} ions/cm^2 where (a) is the relative normalized ion concentration, (b) is the relative normalized vacancy-type defect concentration, and (c) is the relative PL intensity of the samples. The PL intensity of the sample implanted at 90 keV is multiplied by a factor of 10 for clarity.

Table 3.5: Summary of the peak wavelength and corrected PL intensity for the samples shown in Figure 3.12(c). The PL intensity was corrected for the system response.

Sample	Peak Wavelength (nm)	Corrected PL Intensity (a.u.)
450 keV	784	15.9
90 keV	727	1.3
450 & 90 keV	777	26.9

before any conclusions are made the slight difference in absorption and reflection of the pump beam for the different samples needs to be considered.

We can approximate the intensity of the pump beam using transfer matrices often used to calculate the optical response of multilayer structures [60, 61]. The relationship between the electric and magnetic vectors of a single layer with the incident and substrate media can be expressed in a matrix notation given by

$$\begin{bmatrix} B \\ C \end{bmatrix} = \left\{ \prod_{m=1}^{s-1} \underbrace{\begin{bmatrix} \cos\delta_m & \dfrac{i\sin\delta_m}{\gamma_m} \\ i\gamma_m \sin\delta_m & \cos\delta_m \end{bmatrix}}_{\text{transfer matrix}} \right\} \begin{bmatrix} 1 \\ \gamma_s \end{bmatrix} \tag{3.1}$$

where δ_m is the phase factor and $\gamma_{m,s}$ is the admittance. The phase factor, and the admittance for the s- and p-polarized waves are expressed as

$$\delta_m = \frac{2\pi}{\lambda_o} N_m d_m \cos\theta_m$$

$$\gamma_{m,s} = N_{m,s} \cos\theta_{m,s} \qquad \text{s-polarized (TE)}$$

$$\gamma_{m,s} = \frac{N_{m,s}}{\cos\theta_{m,s}} \qquad \text{p-polarized (TM)}$$

where λ_o is the pump beam wavelength in air, d_m is the thickness of the layer, N_m is the complex refractive index, and θ_m is the angle of refraction. The complex

refractive index combines the refractive index (n_m) and extinction coefficient (k_m), and the angle of refraction is determined by Snell's law.

$$N_m = n_m - ik_m$$

$$N_{m-1} \sin\theta_{m-1} = N_m \sin\theta_m \qquad \text{Snell's law}$$

From the matrix relationship in Eq. 3.1, the reflection, transmission and absorption of the system can be calculated as follows

$$R = \left(\frac{\gamma_o B - C}{\gamma_o B + C}\right)\left(\frac{\gamma_o B - C}{\gamma_o B + C}\right)^*$$

$$T = \frac{4\gamma_o \mathrm{Re}\left(\gamma_s\right)}{\left(\gamma_o B + C\right)\left(\gamma_o B + C\right)^*}$$

$$A = \frac{4\gamma_o \mathrm{Re}\left(BC^* - \gamma_s\right)}{\left(\gamma_o B + C\right)\left(\gamma_o B + C\right)^*}$$

where γ_o and γ_s are the admittance of the incident and substrate media respectively.

Since the implanted film is inhomogeneous, the optical properties will vary from the reference SiO_2 depending on the excess silicon concentration as is shown in Table 3.6. From the TEM images it was calculated that approximately ten percent of the implanted silicon ions are consumed in the formation of Si-nc. Combining that with the negligible change in the RBS implant profile after annealing, would indicate that the refractive index and extinction coefficient will change in accord with the implant profiles shown in Figure 3.12(a). Therefore, we divided the film into 10 nm layers, weighting them according to the implant profiles such that the average of all the layers equalled the effective optical properties measured by ellipsometry. We verified this assumption by calculating the films' reflectance, transmittance and

Table 3.6: Summary of the ellipsometry measurements at the pump wavelength of 325 nm.

Sample	Refractive Index	Extinction Coefficient
Reference SiO_2	1.486	0
450 keV	1.520	0.0056
90 keV	1.498	0.0012
450 & 90 keV	1.542	0.0071

absorption using the effective optical properties measured by ellipsometry and the multilayer method with nearly identical results.

To determine the pump beam intensity for each layer, the transmitted light to the layer and the reflected light from subsequent layers deeper in the film must be calculated. The transmitted light can be calculated using the multilayer approach for every layer starting from the surface and working toward the substrate. The intensity of reflected light on the other hand will be small due to the small difference in refractive index and extinction coefficient between layers, and as such is orders of magnitude smaller than the transmitted light. Thus, the relative pump beam intensity is strongly dependent on the calculated transmittance and results for the TE and TM modes are shown in Figure 3.13. Figure 3.13 shows the pump intensity for the incoming beam excluding the reflected light from the substrate. The exclusion of the reflected light will underestimate the pump beam intensity in the 450 keV region for samples A and C but in the same manner for both, and in the 90 keV region of sample B. The underestimation affects only the difference in intensity between samples B and C in the 90 keV region, where sample B would have a larger intensity due to the lack of absorption by the SiO_2. From these calculations the pump intensity in the 90 and 450 keV regions of sample C is lower than in their

single implant counterpart (samples A and B), however the PL intensity is larger for sample C. The stronger PL intensity despite the lower pump beam intensity is most likely due to an increase in the number of Si-nc of sizes similar to sample A in agreement with argument (ii) above. This strongly supports the postulate that the Si-nc growth, size, and location are dependent on the concentration of vacancy-type defects.

An important implication of these results is highlighted by the TEM images in Figure 3.5(b). From these we can estimate that for a single energy implantation process, only ten percent of the implanted Si ions form Si-nc. By judicious choice of multiple implantation energies and doses, it may be possible to engineer greater efficiency in the use of the supersaturated Si concentration in the formation of Si-nc.

3.6 Summary and Conclusions

Understanding the growth mechanisms of Si-ncs is critical because it determines their size and ultimately their emission characteristics. The importance of the growth mechanism is evident through ion implantation, which is a reliable and controllable means of manipulating Si-nc growth through the introduction of more vacancy-type defects to obtain a desirable nanocrystal size for a particular application. Transmission electron microscope measurements and SRIM simulations initially indicated the correlation between the vacancy-type defect distribution and the Si-nc growth. Further experiments utilizing Rutherford backscattering and positron annihilation confirmed that the SRIM simulated distributions were a good representation of the experimental ion and vacancy-type defect distributions. Finally,

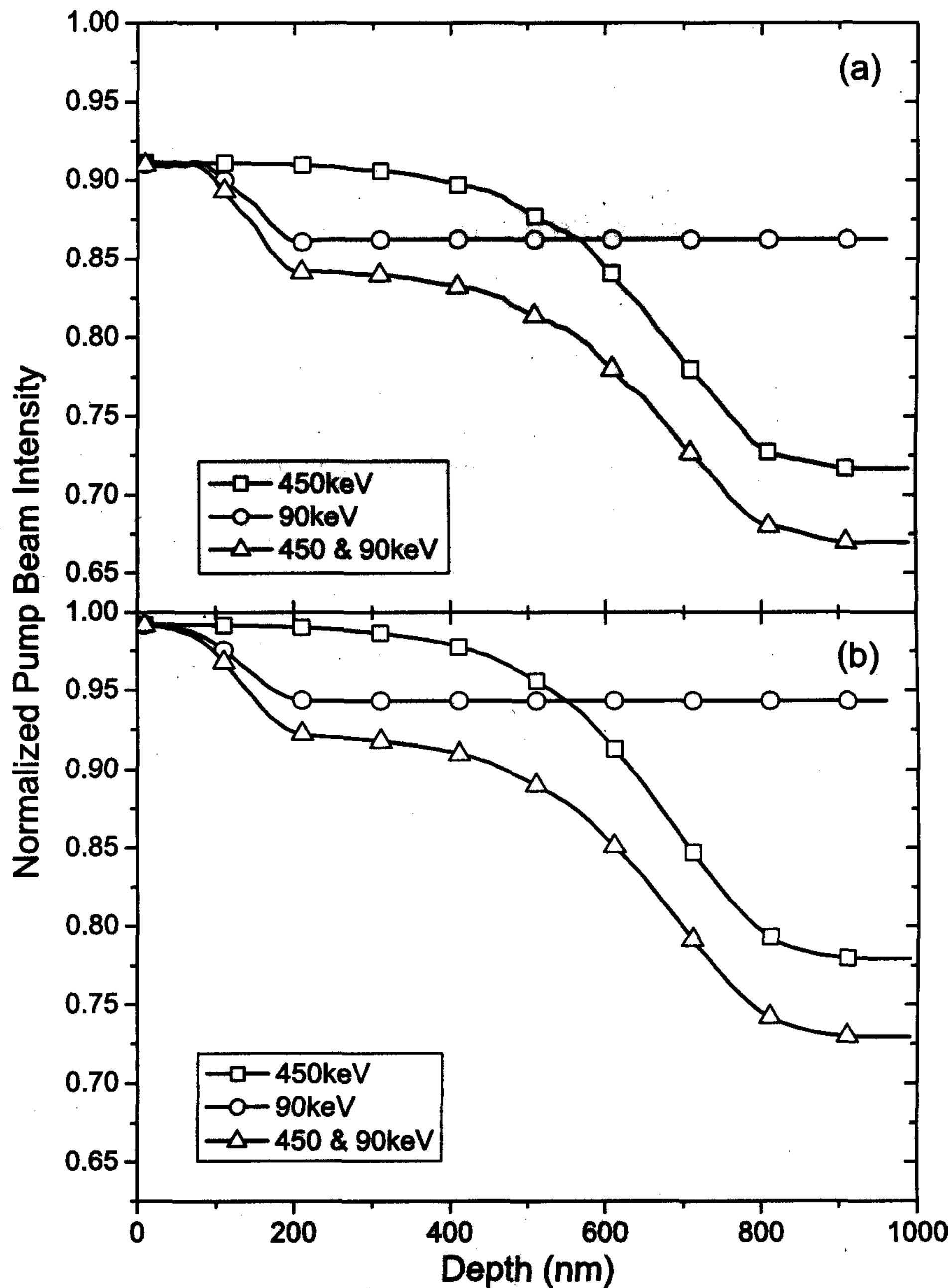

Figure 3.13: Pump beam intensity at different depths within samples A, B and C for (a) the TE modes and (b) the TM modes. The angle of incidence of the incoming beam was 45°.

an experiment verified the correlation of the Si-nc growth to the vacancy-type defect distribution through a double implantation, one deep within the material and the other near the surface. Based on the presented evidence and analysis, the initial growth, size, and location of the Si-nc is dependent on the vacancy-type defect distribution, which was previously unknown.

CHAPTER 4

Silicon Nanocrystal Optical Properties

4.1 Overview

This chapter describes the relationship between the nanocrystal size distribution as determined by TEM and their photoluminescence (PL) spectra, and the process of determining Si-nc's recombination strength. Two quantum confinement models were utilized to investigate the potential relationship between Si-nc size and luminescent emission: a one-dimensional finite square well; and a three-dimensional finite spherical well. The one-dimensional finite square well approximated the luminescent emission of the Si-nc better than the three-dimensional spherical well did. The one-dimensional finite square well also gave better agreement to experimental data reported by others. Applying the one-dimensional finite square well to all of the measured Si-nc sizes permitted the determination of the Si-nc's recombination strength. Through the recombination strength, additional experimental measurements and other published results, it was established that energy is transferred from smaller Si-nc to larger Si-nc, resulting in less efficient Si-nc. The most efficient Si-nc size was approximately 1.75 nm in diameter, where a *quasi*-direct transition can occur. Finally, the larger Si-nc behaved like bulk silicon as their size increased, reducing the Si-nc's efficiency. All these results are discussed in the following sections.

4.2 Introduction

The luminescent mechanisms of Si-nc have been widely debated [23–25, 27–30], which is a barrier to correlating the Si-nc emission wavelength to any model. Wolkin *et al.* [24] observed that following exposure to oxygen, smaller porous silicon samples would redshift and this shift was attributed to localized surface states. Godefroo *et al.* [33] measured photoluminescence (PL) in large magnetic fields and determined that Si-nc in SiO_2 exhibit two discrete luminescent mechanisms depending on the system's passivation. In unpassivated systems, the luminescent mechanism was correlated to localized surface states (similar to Wolkin *et al.*), but in hydrogen passivated systems, the luminescent mechanism was associated to quantum confinement. Since our PL measurements were completed after a hydrogen passivation, the quantum confinement and measured size distribution could be correlated with the PL.

Prior to linking the Si-nc size to quantum confinement, the uniformity in the excitation of Si-nc by the pump laser, and the absorption cross section for various Si-nc sizes must be determined. As the pump laser propagates through the SiO_2 layer containing the ensemble of Si-nc's, internal reflections and absorptions occur depending on the Si content and the nanocrystal sizes. The mean Si-nc size as a function of depth, presented in the previous Chapter, ranged from 1.67 to 1.86 nm with a standard deviation of approximately 0.5 nm for all depths. With the similarity in Si-nc size distributions at the different depths, the change in pump intensity as it propagates through the material would not skew the emission spectrum because

the average pump intensity for all sizes is roughly the same. Thus, the excitation of the Si-nc by the pump laser can be considered uniform.

The Si-nc's absorption cross section across the range of measured sizes was assumed to be uniform. This assumption is supported by Kovalev *et al.* [62], who demonstrated that the absorption cross section in porous silicon became more uniform as the excitation energy increased from 1.93 to 3.53 eV. Similar results of uniformity in the absorption cross section have been observed at higher pump laser energies for Si-nc embedded in SiO_2 [63]. However, uniformity is also possible at a lower pump laser energy if the pump laser's power is large enough [62, 64]. For our excitation wavelength of 325 nm (3.81 eV) and power density of 0.64 W/cm^2, the absorption cross section would be generally uniform over the range of Si-nc sizes.

Since the PL emission is due to quantum confinement, the Si-nc are uniformly excited by the pump laser, and the absorption cross section is uniform for the range of sizes, we can relate the PL emission to the Si-nc size distribution. The one-dimensional finite square well is the simplest first principle quantum confinement model that can be employed to link the PL emission with the Si-nc size distribution. Considering Si-nc are three-dimensional spheres, a three-dimensional finite spherical well is a more realistic model. There are other possible methods for calculating the emission energy of Si-nc, such as the effective mass approximation [34], the truncated crystal method [34], direct molecular calculations [34, 65], empirical tight-binding model [35], empirical pseudo-potential [34, 36], and others. However, the first principle methods have had little to no success and some of the methods require fitted parameters, which naturally leads to good agreement [31]. Therefore, only the

one-dimensional square well and three-dimensional spherical well will be addressed further.

4.3 Quantum Confinement Models

For the quantum confinement models presented in this chapter, the electrons and holes are treated separately because the majority of Si-nc were in a regime of strong quantum confinement where $d < 2a_e$ (3.7 nm) and $d < 2a_h$ (2.2 nm), with d being the diameter of the Si-nc, and a_e and a_h being the effective Bohr radii of the electron and hole respectively [31]. The electron and hole Bohr radii were calculated with the following expression [31]:

$$a_{e,h} = \frac{4\pi\varepsilon_o\varepsilon_r\hbar^2}{m^*_{e,h}e^2}$$

where ε_o is the permittivity of free space, ε_r is the dielectric constant of silicon (11.9), $\hbar$ is Planck's reduced constant, $m^*_{e,h}$ is the effective mass of the electron and hole respectively, and e is the charge of an electron. The effective masses of the isotropic electron and hole were calculated to be $0.33m_o$ and $0.55m_o$ (m_o is the free electron mass), using the following expressions [66]:

$$m^*_e = \left(m^*_l m^{*2}_t\right)^{\frac{1}{3}}$$
$$m^*_h = \left(m^{*\frac{3}{2}}_{lh} + m^{*\frac{3}{2}}_{hh}\right)^{\frac{2}{3}}$$

where m^*_l is the longitudinal mass ($0.98m_o$), m^*_t is the transverse mass ($0.19m_o$), m^*_{lh} is the light hole mass ($0.16m_o$), and m^*_{hh} is the heavy hole mass ($0.49m_o$) of silicon. These effective masses agree with values presented by Godefroo *et al.* [33].

Table 4.1: One-dimensional and three-dimensional model parameters.

Carrier type	Effective mass (m_o)		Barrier Height (eV)
	Si	SiO_2	
electrons	0.33	0.5	3.2[a]
holes	0.55	0.35	4.7[b]

[a] References [68, 72, 73]
[b] References [72, 73]

The effective mass for the electron in both bulk and thin film SiO_2 is approximately $0.5m_o$ [67–69], and the effective mass for the holes varies dramatically from 3-10m_o for bulk SiO_2 to approximately $0.35m_o$ in thin films [70, 71]. Based on the TEM images and evaluating the Wigner-Seitz radius, it was determined that the closest distance between the Si-nc was approximately 7 nm (Appendix A), implying that the hole's effective mass can be treated like that in a thin film. A summary of the parameters used for the models are given in Table 4.1.

4.3.1 One-Dimensional Finite Square Well

The one-dimensional finite square well is often utilized for multi-layered structured systems where the electron-hole pairs are confined in one spatial dimension with a small feature size [73–75]. In Si-nc, electron-hole pairs are confined in all three spatial dimensions, which indicates that a three-dimensional model would be more appropriate. However, beginning with a simple model and adding complexities to the model can render interesting results. The emission energy in the one-dimensional finite square well can be determined by solving Schrödinger's time-independent wave

equation

$$-\frac{\hbar^2}{2m^*_{e,h}}\frac{d^2\psi}{dx^2}+V_{e,h}\psi=E_{e,h}\psi$$

with the potential energy of the system given by

$$V_{e,h}(x)=\begin{cases}0, & \text{for } |x|<a\\ V_o, & \text{for } |x|>a\end{cases}$$

where V_o is the potential energy barrier height of 3.2 eV for the electron [68, 72, 73] and 4.7 eV for the hole [72, 73], and a is the radius of the Si-nc. The general solutions for the Schrödinger equation, both inside and outside of the nanocrystal, in this system are:

$$\psi(x)=\begin{cases}A\cos(\kappa x), & \text{for } |x|<a \quad \text{even solution}\\ C\exp(-kx), & \text{for } |x|>a\end{cases} \tag{4.1}$$

$$\psi(x)=\begin{cases}B\sin(\kappa x), & \text{for } |x|<a \quad \text{odd solution}\\ C\exp(-kx), & \text{for } |x|>a\end{cases} \tag{4.2}$$

with

$$\kappa=\frac{\sqrt{2m^*_{e,h(in)}E_{e,h}}}{\hbar} \qquad \text{and} \qquad k=\frac{\sqrt{2m^*_{e,h(out)}\left(V_o-E_{e,h}\right)}}{\hbar}$$

where the effective masses are indicated either inside or outside of the nanocrystal, and A, B and C are normalization constants. The general solution for the nanocrystal should be continuous at the boundary, which implies that ψ and $d\psi/dx$ at $|x|=a$, inside and outside the well, must be equal to each other. After some

algebra transcendental expressions are obtained and given by

$$\sqrt{\left(\frac{z_o}{z}\right)^2 - \frac{m^*_{e,h(out)}}{m^*_{e,h(in)}}} = \begin{cases} \tan(z), & \text{even solution} \\ -\cot(z), & \text{odd solution} \end{cases} \tag{4.3}$$

where $z = \kappa a$ and $z_o = a/\hbar\sqrt{2m^*_{e,h(out)}V_o}$. More detailed calculations are given in Appendix B. The above transcendental expressions differ slightly from those presented in quantum mechanics textbooks due to the variation in the effective masses inside and outside the one-dimensional finite square well. Solving the even solution in Eq. 4.3 determined the first excited energy states of the electron and hole in the Si-nc, and the odd solution determined the second excited energy states. Along with the individual excited states for the electrons and holes, the silicon band gap of 1.12 eV must also be included to obtain the emission energy of the Si-nc.

$$E = E_g + E_e + E_h \tag{4.4}$$

The application of Eqs 4.3 and 4.4 to the TEM measured Si-nc mean diameter of 1.78 nm results in a first excited state emission energy of 1.54 eV (806 nm) and a second excited state emission energy of 2.76 eV (448 nm). The emission wavelength of the first excited state is similar to the measured PL peak wavelength of 825 nm. This good result should improve with the three-dimensional finite spherical well.

4.3.2 Three-Dimensional Finite Spherical Well

Based on the good results from the one-dimensional model and the fact that Si-nc are three-dimensionally confined, it is assumed that the three-dimensional finite spherical well would approximate the emission energy better. To determine the

emission energy in three-dimensions requires solving the radial Schrödinger equation given by

$$-\frac{\hbar^2}{2m^*_{e,h}}\frac{d^2\psi}{dr^2}+\left[V_{e,h}+\frac{\hbar^2}{2m^*_{e,h}}\frac{\ell(\ell+1)}{r^2}\right]\psi=E_{e,h}\psi$$

with

$$V_{e,h}(r)=\begin{cases}0, & \text{for } |r|<a\\ V_o, & \text{for } |r|>a\end{cases}$$

where V_o is the potential energy barrier, a is the radius of the Si-nc, and ℓ is the angular momentum. The general solution to the radial Schrödinger equation inside the nanocrystal for the zeroth order ($\ell=0$) is the spherical Neumann function of the first kind and the spherical Bessel function of the first kind. The general solution to the radial Schrödinger equation outside the nanocrystal for the zeroth order is the Hankel function of the first kind. In this system the general solutions can be separated as follows:

$$\psi(r)=\begin{cases}n_o(\kappa r)=-A\dfrac{\cos(\kappa r)}{\kappa r}, & \text{for } |r|<a \quad \text{Neumann Function}\\ h_o^{(1)}(ikr)=-C\dfrac{\exp(-kr)}{kr}, & \text{for } |r|>a\end{cases} \tag{4.5}$$

$$\psi(r)=\begin{cases}j_o(\kappa r)=B\dfrac{\sin(\kappa r)}{\kappa r}, & \text{for } |r|<a \quad \text{Bessel Function}\\ h_o^{(1)}(ikr)=-C\dfrac{\exp(-kr)}{kr}, & \text{for } |r|>a\end{cases} \tag{4.6}$$

with once again

$$\kappa=\frac{\sqrt{2m^*_{e,h(in)}E_{e,h}}}{\hbar} \quad \text{and} \quad k=\frac{\sqrt{2m^*_{e,h(out)}(V_o-E_{e,h})}}{\hbar}$$

where the effective masses are indicated either inside or outside of the nanocrystal, and A, B and C are normalization constants. Similar to the one-dimensional

finite square well, the general solution inside and outside of the nanocrystal should be continuous at the boundaries. After some algebra the following transcendental expression is obtained:

$$\sqrt{\left(\frac{z_o}{z}\right)^2 - \frac{m^*_{e,h(out)}}{m^*_{e,h(in)}}} = -\cot(z) \tag{4.7}$$

where $z = \kappa a$ and $z_o = a/\hbar\sqrt{2m^*_{e,h(out)}V_o}$. It should be noted that the transcendental expression (Eq. 4.7) is similar to Eq. 4.3 apart from the even solution disappearing due to the Neumann function having a singularity as r $\rightarrow$ 0. More detailed calculations are given in Appendix B. This is a fascinating result because the even solution agreed best with the PL results and the odd solution dramatically overestimates the emission energy. Due to the poor correlation between the three-dimensional model and the PL results, researchers rely on more complicated theoretical methods. However, these methods for determining the emission energy do not accurately reproduce the experimental emission characteristics.

A possible explanation for the poor agreement between the three-dimensional spherical well and the experimental PL data could be related to the crystallinity of the nanocrystals. The three-dimensional model assumes spherical symmetry, which is lost in crystalline silicon due to its cubic symmetry. This loss of symmetry would negate the assumption made in the three-dimensional model potentially explaining its inability to predict experimental results. The loss of symmetry three-dimensionally could also be an explanation for the one-dimensional model being able to predict experimental PL results more effectively. Another possible explanation is uniaxial stress on the nanocrystals that break the symmetry leading to a preference

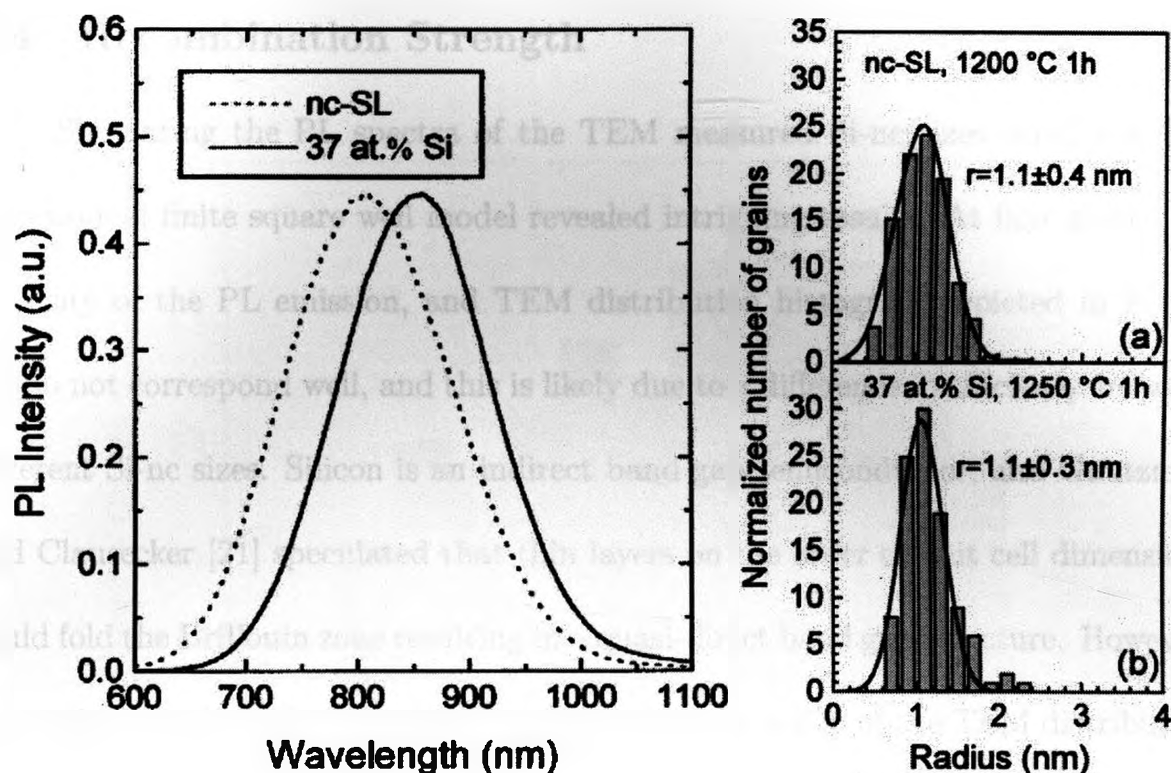

Figure 4.1: On the left is the PL emission from a Si/SiO_2 superlattice (SL) structure and Si-nc in SiO_2 with similar shape and peak wavelength. On the right is the TEM histogram for the two different systems with similar Gaussian distributions [64].

in one direction.

Furthermore, in a publication by Priolo *et al.* [64], the PL emission spectra of a Si/SiO_2 superlattice structure and Si-nc in SiO_2 were reported to be similar for samples with similar TEM size distributions (Figure 4.1), despite the difference in dimensionality. A Si/SiO_2 superlattice structure is spatially confined only in one dimension and would indicate that the one-dimensional model could potentially approximate the emission energy of a wide range of Si-nc sizes. Thus, the emission energy of the Si-nc sizes from the TEM results were simulated by the one-dimensional model and compared to the experimental PL emission.

4.4 Recombination Strength

Simulating the PL spectra of the TEM measured Si-nc sizes using the one-dimensional finite square well model revealed intriguing results. At first glance the intensity of the PL emission, and TEM distribution histogram depicted in Figure 4.2 do not correspond well, and this is likely due to a difference in efficiency between different Si-nc sizes. Silicon is an indirect band gap semiconductor, and Gnutzman and Clausecker [21] speculated that thin layers on the order of unit cell dimensions could fold the Brillouin zone resulting in a quasi-direct band gap structure. However, the critical result is illustrated in Figure 4.2 (b): the width of the TEM distribution histogram is roughly equal to the width of the PL emission, which indicates that the one-dimensional model is appropriate for a wider range of emission wavelengths. In addition, the results in Figure 4.2 can be utilized to determine the most efficient nanocrystal size for emitting a photon or, as previously stated, to determine the recombination strength [76].

The recombination strength was determined by dividing the measured PL spectrum by the emission spectrum simulated from the TEM distribution utilizing the one-dimensional square well model. The results of this are shown in Figure 4.3 (a). The data points in Figure 4.3 (a) were fitted with the following expression to help guide the eye:

$$y = A\exp\left[-\exp\left(-\frac{x-x_c}{w}\right) - \left(\frac{x-x_c}{w}\right) + 1\right] \tag{4.8}$$

where A is the amplitude, x_c is the centre of the peak, and w is the width of the curve. Recombination strength results for Si/SiO_2 superlattice structures have also

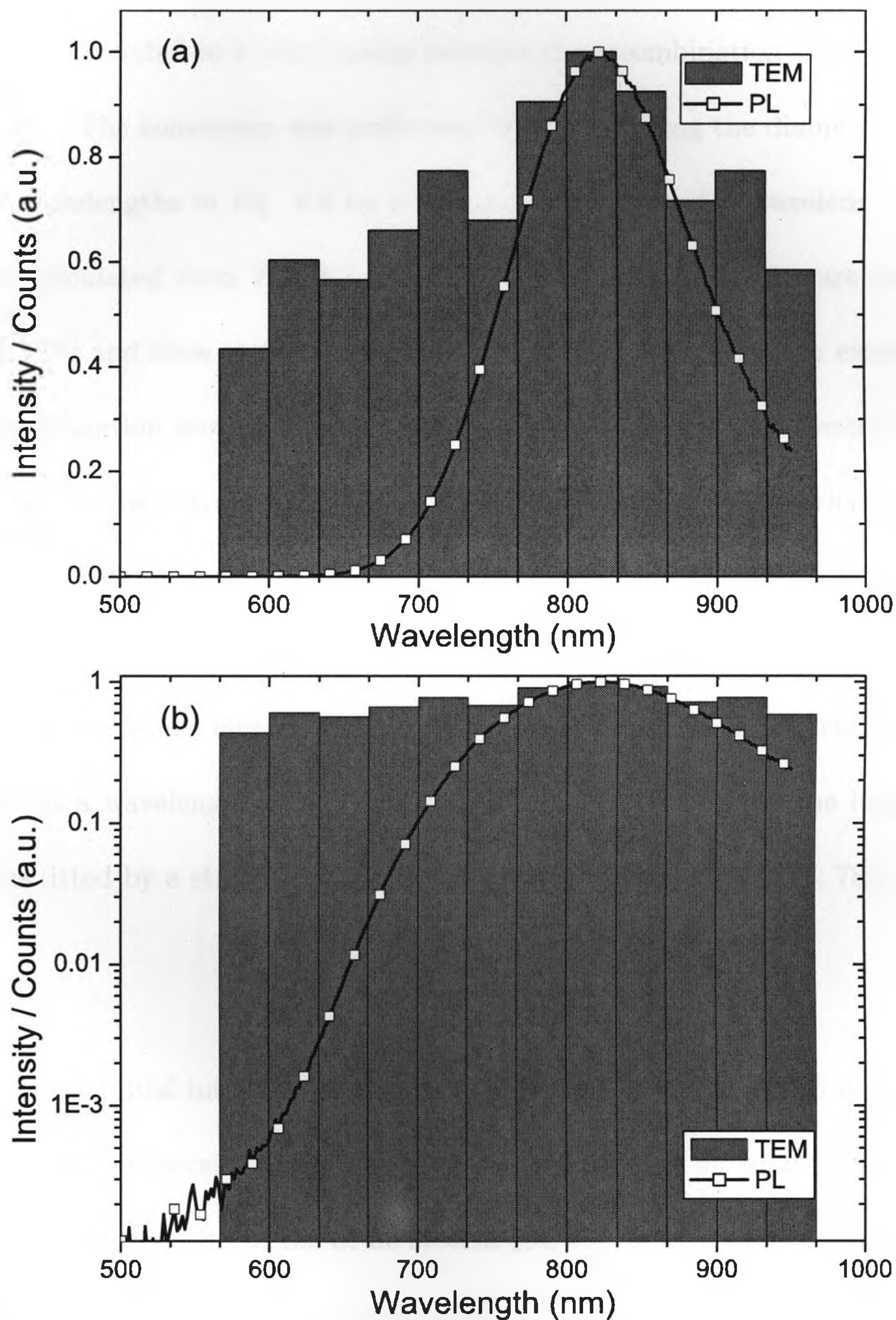

Figure 4.2: PL and TEM results superimposed using the one-dimensional model. (a) plots the results linearly, and (b) plots the results logarithmically.

been reported with respect to the silicon layer thickness [76], and can be compared to the results in Figure 4.3. But in order to compare the two results Figure 4.3 (a) needs to be converted to a relationship between the recombination strength and Si-nc diameter. The conversion was performed by interpolating the diameter from the emission wavelengths in Eq. 4.8 by using an array of emission wavelengths versus diameter calculated from Eqs 4.3 and 4.4. The conversion results are plotted in Figure 4.3 (b) and show similarities to the superlattice structures. For example, the peak recombination strength for both superlattice and Si-nc was around 1.7 nm. These results demonstrate further the similarities between superlattice structures and Si-nc.

Moreover, the recombination strength results in Figure 4.3 (a) are supported by luminescent lifetime measurements. A luminescent lifetime measurement of Si-nc that emit at a wavelength of 800 nm is shown in Figure 4.4, and the luminescent decay was fitted by a stretched exponential function given by [64, 77, 78];

$$I(t) = I_o \exp\left[-\left(\frac{t}{\tau}\right)^{\beta}\right]$$

where I_o is the initial intensity, t is time, τ is the time constant, and β is the dispersion factor. The dispersion factor has been shown to change for smaller nanocrystals depending on the density of the Si-nc system [64, 78]. The authors of those studies concluded that energy migrated from smaller to larger nanocrystals and that the smaller the dispersion factor, the greater the migration of energy to larger nanocrystals. If energy can migrate from smaller to larger nanocrystals, it may be possible in larger nanocrystals to observe energy migrating to non-radiative recombination cen-

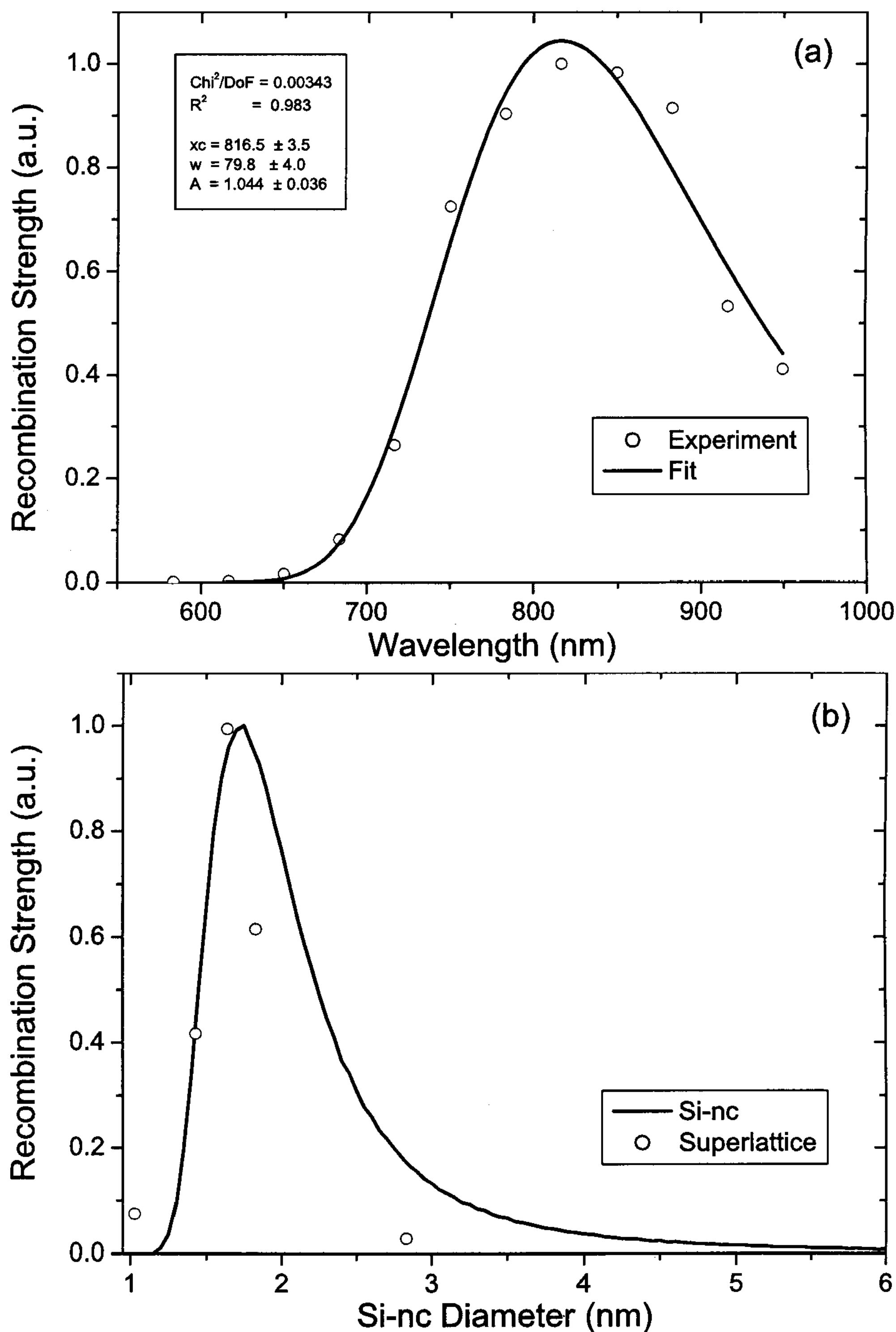

Figure 4.3: (a) Fitted recombination strength of the Si-nc with respect to the emission wavelength using the results in Figure 4.2. (b) Recombination strength converted into the equivalent nanocrystal diameter along with the recombination strength from the superlattice (SL) structures [76].

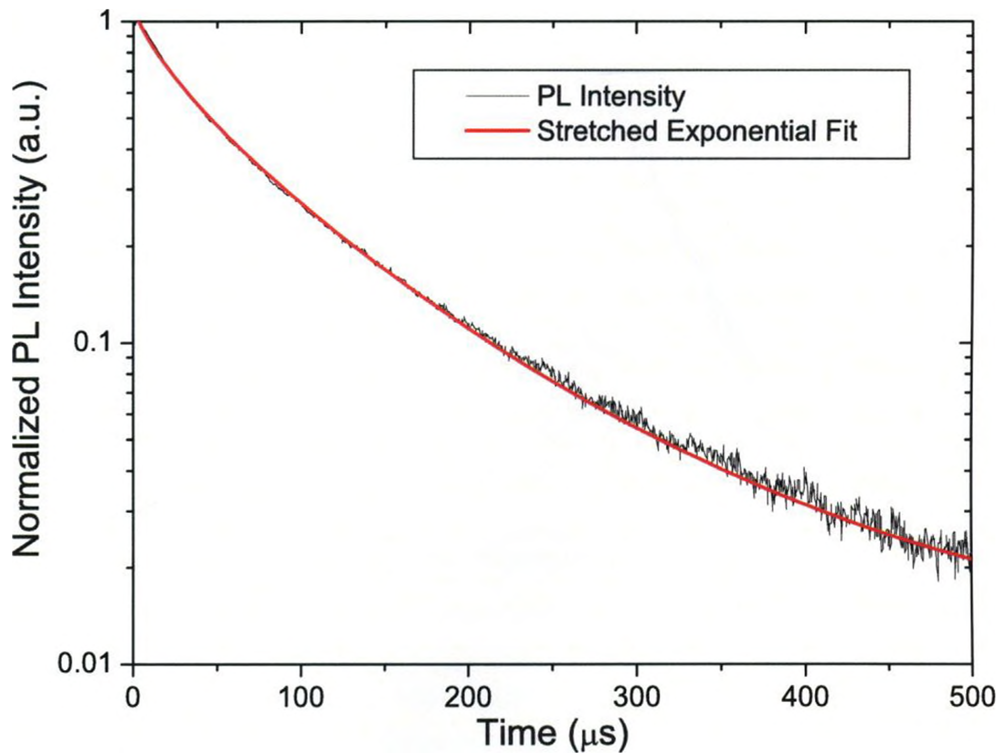

Figure 4.4: Luminescent lifetime measurement of Si-nc emitting light at a wavelength of 800 nm, fitted with a stretched exponential. The luminescent lifetime measurements were performed utilizing a monochromator and photomultiplier tube, along with a pump wavelength of 473 nm and a pump power of 40 mW.

tres. As the nanocrystals get larger the probability of non-radiative recombination centres increases [7] and thus the dispersion factor should decrease.

Lifetime measurements could be a means of determining the recombination strength because more efficient nanocrystals tend to utilize their energy in radiative processes. Comparing the dispersion factor results to the recombination strength reveals similarities in the shape of the curve and the approximate location of the most efficient wavelength (Figure 4.5). The similar shape and location of the most efficient wavelength are good indicators that the recombination strength is comparable to the dispersion factor. Dispersion factor results observed by Linnros *et al.* [78] had a similar tendency to the one illustrated in Figure 4.5. Furthermore, Pavesi *et al.* [79] made optical gain measurements with a similar trend to the dispersion factor

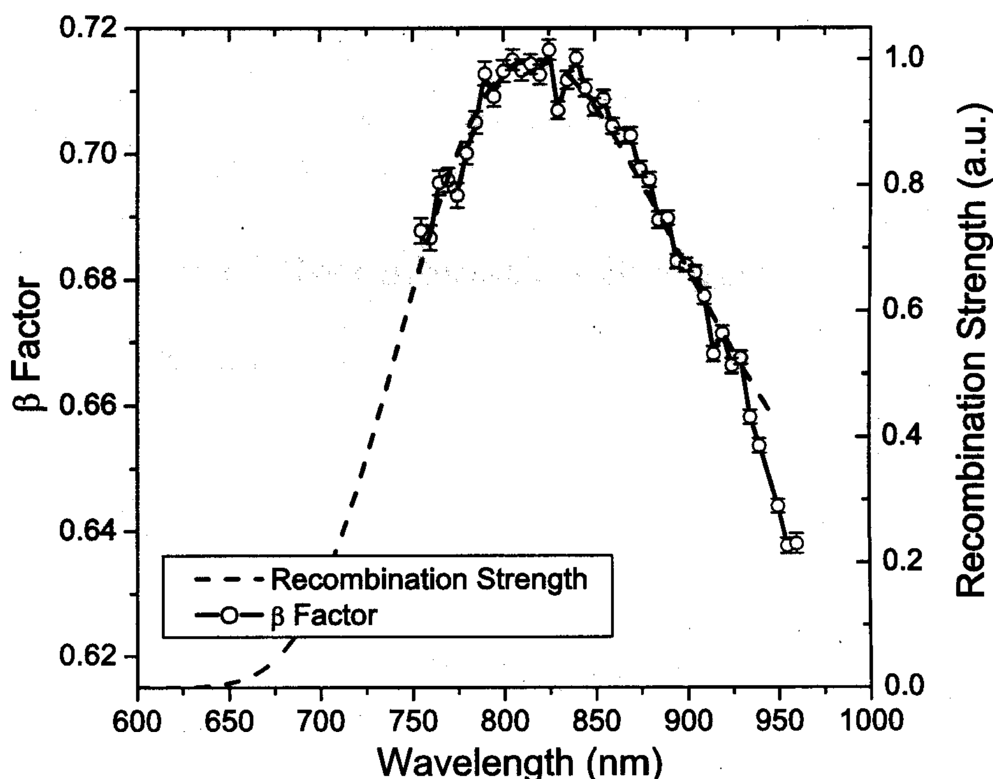

Figure 4.5: Dispersion factor plotted along side the recombination strength indicating similarities in the trend and peak location. The luminescent lifetime measurements were performed with a pump wavelength of 473 nm and a pump power of 40 mW. The beam spot was approximately 1 mm in diameter.

results in Figure 4.5 with the highest gain achieved at 800 nm.

The comparable recombination strength, dispersion factor results and published optical gain results could indicate a quasi-direct transition. The recombination strength peak in Figure 4.3 (a) occurred at 816 nm, but the TEM distribution histogram has broad bin sizes of 33 nm, and 816 nm is at the centre of one bin. The most efficient size in Figure 4.3 (b) was 1.75 nm or an emission wavelength of 800 nm. Pavesi *et al.* [79] measured the optical gain of Si-nc and discovered that it peaked at 800 nm and the optical gains were of the same order as other direct band gap quantum dots. Furthermore, the dispersion factor results also peaked between 800 and 830 nm. Therefore, the most efficient emission wavelength should be be-

tween 800 and 830 nm, and measurements of the direct transition are possible with a tunable laser. Unfortunately, such measurements were not able to be performed.

4.5 Discussion of Recombination Strength

4.5.1 Large to Medium Size Nanocrystals (> 1.75 nm)

Figure 4.3 (b) illustrates that the recombination strength peaks at a nanocrystal size of 1.75 nm, and this is attributable to several factors. The electron and hole wavefunctions increasingly overlap for smaller nanocrystals due to the spatial confinement of the well, which increases the probability of a radiative process [7]. Smaller nanocrystals are less likely to have non-radiative recombination centres, which allows smaller nanocrystals to be more optically active [7]. In addition, the Brillouin zone can fold and then requires smaller momentum phonons. The smaller phonons can quicken the radiative process by improving the probability that an electron and hole occupy a radiative recombination centre simultaneously. All of these factors to some extent should be and are observable in the dispersion factor and lifetime measurements (Figure 4.5 and Figure 4.6). As the nanocrystals get smaller the dispersion factor improves indicating more efficient radiative processes, and the lifetimes become shorter indicating a faster radiative process.

Furthermore, in previously reported results [64, 78], β and τ remained consistent at higher wavelengths regardless of nanocrystal density. This suggests that the density of the Si-nc does not affect the behaviour of the larger nanocrystals [64]. Therefore, the results and conclusions for larger nanocrystals (> 1.75 nm) would indicate quantum confinement and the material transitioning from a bulk-like material

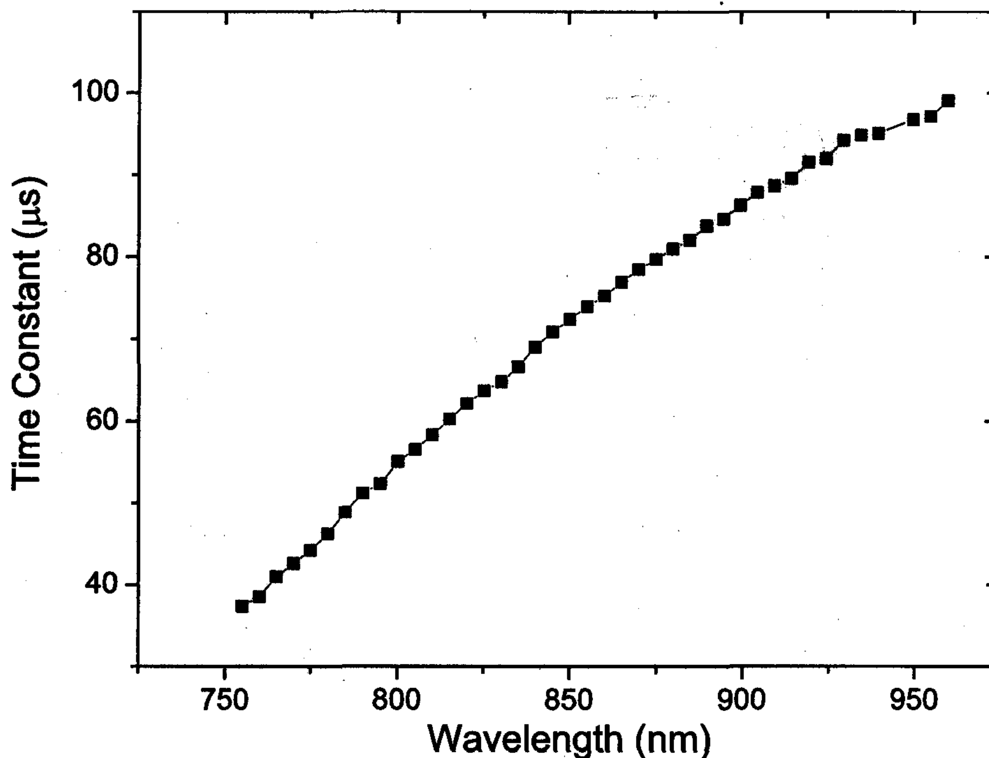

Figure 4.6: Lifetime measurements at various wavelengths that were performed with a pump wavelength of 473 nm and a pump power of 40 mW. The beam spot was approximately 1 mm in diameter.

to a quasi-direct band gap material.

4.5.2 Small Nanocrystals (< 1.75 nm)

In contrast, smaller nanocrystals alter their behaviour depending on the density of the nanocrystal system. At higher implantation doses or larger supersaturations of silicon in SiO_2, β decreases and the decay constant τ becomes shorter. It has been concluded that highly dense nanocrystal systems enhance the migration of energy from smaller to larger nanocrystals [64, 78]. As well, a broader size distribution occurred simultaneously in denser nanocrystal systems, which would promote the migration of energy from smaller to larger nanocrystals. These results and conclusions are reasonable considering the carrier confinement of smaller nanocrystals,

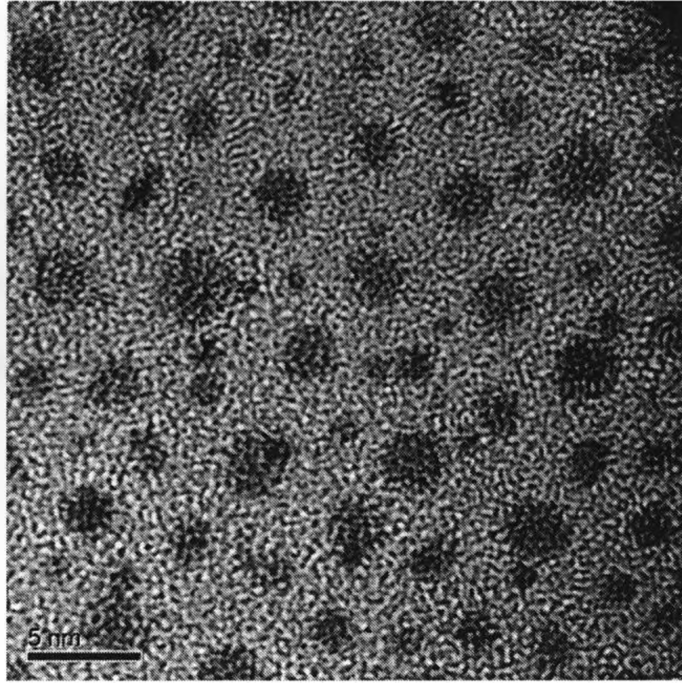

Figure 4.7: TEM image showing smaller nanocrystals closer to larger ones.

and that the growth of the Si-nc occurs through Ostwald ripening.

As the nanocrystals become even smaller, the probability of the electron and hole wavefunctions existing outside the potential well becomes greater. Moreover, as the wavefunctions increasingly branch out of the well, the more likely the carriers are to migrate to larger nanocrystals. In addition, the growth of the Si-nc is mediated by Ostwald ripening [58] whereby large nanocrystals consume the atoms of small nanocrystals. Due to this consumption, it would be expected that smaller nanocrystals are closer to the larger nanocrystals, which is evident in the TEM images (an example image is shown in Figure 4.7). Therefore, the close proximity of small nanocrystals to larger nanocrystals and the extension of the wavefunctions into the sample's medium enhance the probability that energy will migrate to larger nanocrystals in densely populated Si-nc systems.

4.6 Photoluminescence Simulations

To date, there have been several publications on the TEM size distribution of Si-nc in SiO_2 and their PL emission [59, 64, 80, 81]. Noteworthy results may be obtained by simulating the PL emissions from the TEM size distributions reported in these publications, using the recombination strength and the one-dimensional model. As such, publications by Iacona *et al.* [80] and Priolo *et al.* [64] will be reviewed.

The TEM images by Iacona provided good contrast between Si and SiO_2. Conversely, the publication by Priolo did not provide the TEM images, but since Iacona was a co-author it was assumed that the TEM images were of similar quality. Unfortunately, in the publication by Iacona the PL emission spectra for some of the TEM nanocrystal size distributions were not presented. However, in the Priolo publication, PL emission spectra were presented that matched the missing PL emission stated in the Iacona publication with the same material property characteristics. Therefore, it was assumed that the PL results in the Priolo publication were from the same or similar samples to those presented in the Iacona publication.

The PL emission for the two publications was simulated by multiplying the Gaussian size distributions stated by the authors with the recombination strength to obtain the light-emitting effective distribution. The effective distributions were then evaluated to an equivalent emission wavelength using the one-dimensional model (Eq. 4.3). A summary of the results is presented in Table 4.2 and shown in Figures 4.8 and 4.9. Better agreement was obtained for smaller nanocrystal distributions,

Table 4.2: Summary of the experimental and simulated PL. The values in brackets of the "simulated" columns represent the difference between the experimental and simulated results.

Sample	Mean Diameter (nm)	σ (nm)	λ_{max} (nm)	λ_{max} Simulated (nm)	FWHM (nm)	FWHM Simulated (nm)
A1-SL	2.2	0.8	810	830 (+20)	175	175 (0)
A2	2.2	0.6	860	850 (−10)	165	165 (0)
B1	2.0	0.4	900	835 (−65)	–	130 (–)
B2	2.2	0.4	850	855 (+ 5)	160	130 (−30)
B3	2.6	0.8	915	855 (−60)	185	190 (+ 5)
B4	3.0	0.6	890	940 (+50)	175	150 (−25)
B5	3.4	1.0	910	915 (+ 5)	190	230 (+40)
B6	4.2	1.0	950	1005 (+55)	230	170 (−60)
Mean Difference				34		23

Samples A - Priolo *et al.* [64]
Samples B - Iacona *et al.* [80]

and results deviated more with larger nanocrystal distributions.

4.7 Discussion of PL Simulations

4.7.1 TEM Distributions

Some of the results for which poor agreement was obtained could be attributed to TEM distributions that were over or under estimated due to the difficulty in preparing thin TEM samples, rather than an error in PL measurements. For example, samples $B1$ and $B3$ in Table 4.2 underestimate the PL peak wavelength by 65 and 60 nm, respectively. Plotting the nanocrystal diameter versus PL peak wavelength in Figure 4.10, there exists a linear relationship between the majority of mean nanocrystal sizes and peak PL wavelengths. However, $B1$ and $B3$ appear to be outliers from the linear trend. Calculating the PL peak wavelength for samples

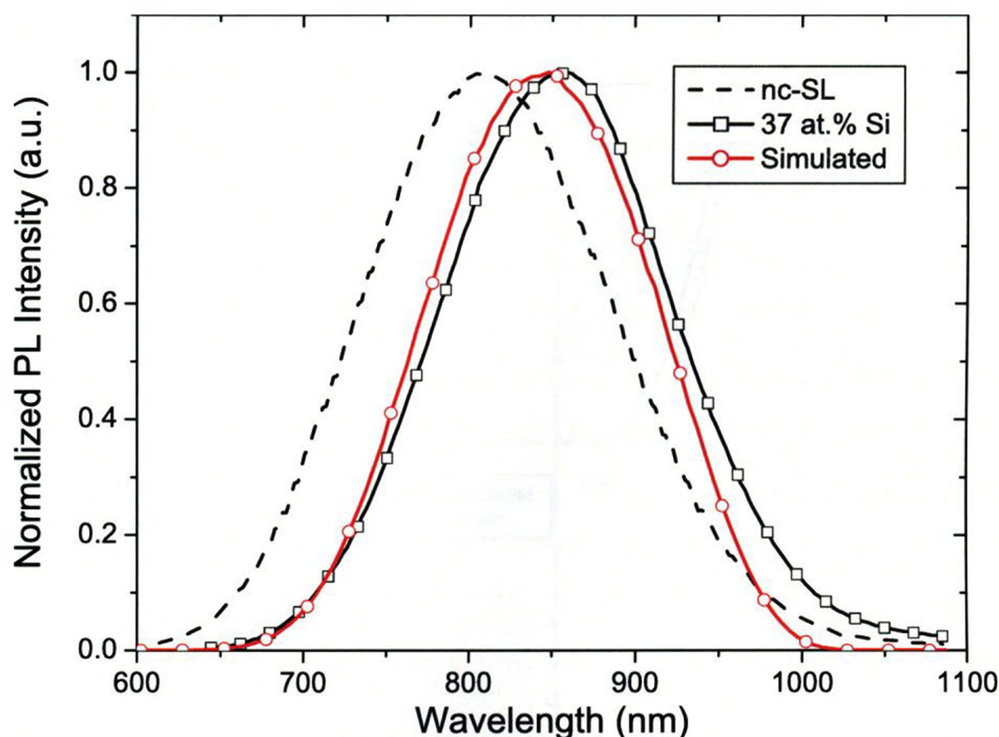

Figure 4.8: Simulated PL (in red) of Si-nc in SiO_2 for a Si concentration of 37% annealed at 1250°C for 1 hr. The experimental PL is from Priolo *et al.* [64], which was previously shown in Figure 4.1.

$B1$ and $B3$ from the linear relationship would result in wavelengths of 840 and 870 nm, respectively. These values differ from the simulated results by 5 and 15 nm, as opposed to 65 and 60 nm. Another example is $B4$ and $B6$, which appear to have a much smaller standard deviation compared to $B3$ and $B5$. If the standard deviation for $B4$ was increased to a value of 0.8 nm, the simulated PL peak wavelength would be 898 nm and the FWHM would be 200 nm, much closer to the experimental results.

As well, both authors' TEM size distributions were fitted using the radius of the nanocrystals, but could have achieved more accurate Gaussian fits had they utilized the nanocrystal diameter while still maintaining the same number of significant digits and decimal places. For example, a mean radius of 1.1 nm is equivalent

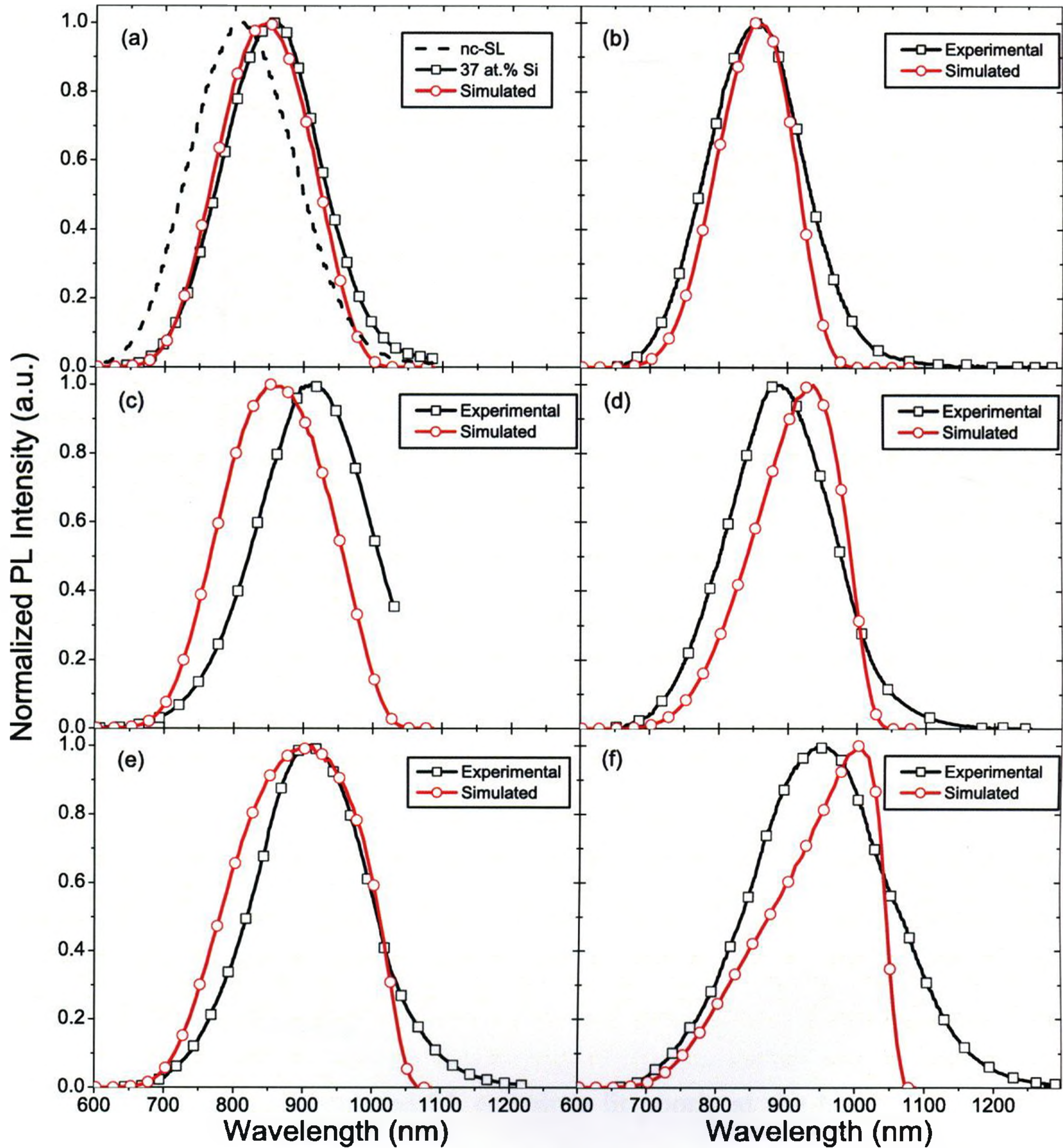

Figure 4.9: The simulated PL emissions are from Table 4.2 sample's $A2$ (a), $B2$ (b), $B3$ (c), $B4$ (d), $B5$ (e), and $B6$ (f). The experimental PL for (a - b), and (d - f) are from Priolo [64], and (c) is from Iacona [80].

to a diameter of 2.2 ± 0.2 nm, whereas a measurement of the mean diameter would have been 2.2 ± 0.1 nm. Thus, the PL emission is revisited in Appendix C, with the exception that our own fit of the TEM size distributions was utilized. Therefore, the accuracy of the TEM measurements can impact how well the PL can be simulated.

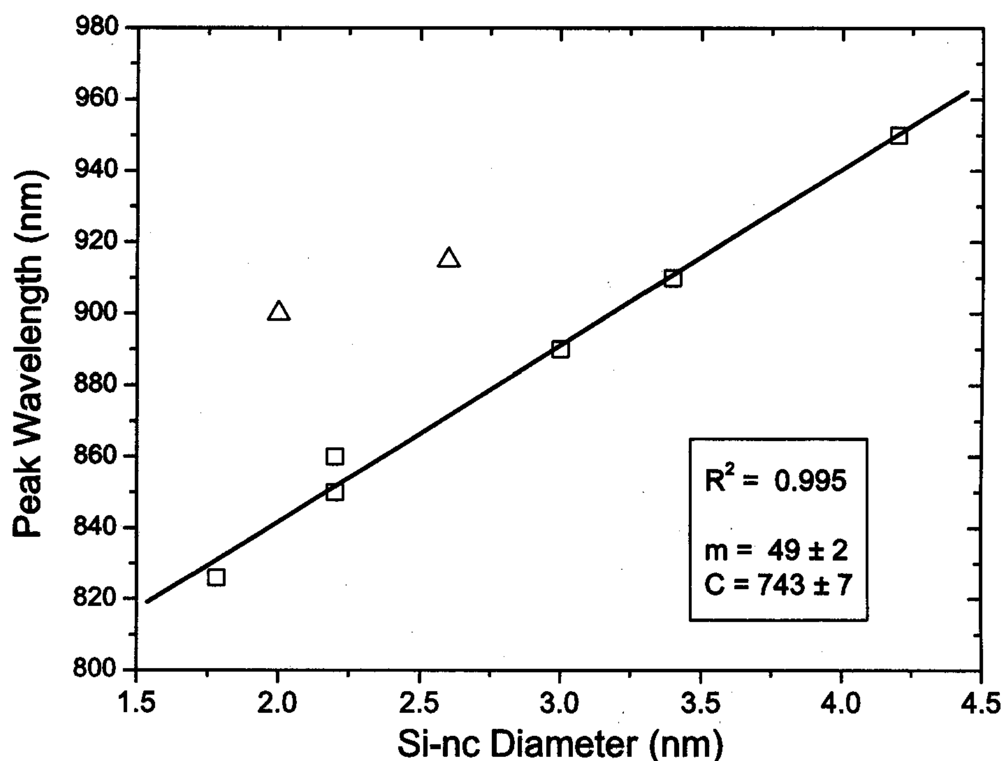

Figure 4.10: PL peak wavelength as a function of Si-nc diameter. A linear relationship exists between the results with a square symbol (□), and the linear fit is from the square symbols. The results with a triangular symbol (△) appear to be outliers.

However, there are other explanations for the deviations between experimental and simulated results.

4.7.2 Interface Defects

Nearly all of the simulated PL emissions fit poorly at the higher wavelengths. Looking closer at the experimental PL in Figure 4.9 one notices that the emission extends beyond 1100 nm, which is below the band gap of silicon. As well, in Figure 4.9(f), one will notice a shoulder in the experimental PL at the higher wavelengths. As has been mentioned before there are two competing luminescent mechanisms: quantum confinement and surface states. Due to hydrogen passivation the quantum confinement mechanism dominates [33], but Iacona and Priolo did not report

performing a final hydrogen anneal. Their PECVD SiO_x films were fabricated with SiH_4 and N_2O gases, which should incorporate a significant amount of hydrogen. Thus, most likely enough hydrogen was provided by the processing of the material to passivate the majority of the Si-nc, but not all of them.

Larger nanocrystals are more prone to have defects and are more difficult to passivate. It is possible that the larger nanocrystals are not passivated well enough and are transferring their energy to surface defects or impurities that may lie below the band gap of silicon. If the larger nanocrystals are not passivated well enough and did transfer energy to surface defects or impurities, then the one-dimensional model would have difficulty simulating the experimental results since it does not include these features. Therefore, surface defects or impurities for larger nanocrystals most likely contributed to the discrepancies between the simulated and experimental PL results.

4.7.3 Coulomb Interaction

The majority of the above published size distributions are in a moderate confinement regime, and the calculations consider a strong confinement regime. In a strong confinement regime the Coulomb interaction between the electron and hole is ignored, but should be included in a moderate confinement regime [31]. The inclusion of the Coulomb interaction should and does improve the accuracy of simulated photoluminescence for both the one-dimensional and three-dimensional models. A more in-depth discussion of the Coulomb interaction, and calculations are presented in Appendix D. One of the important results in Appendix D is that although the

simulated PL improves, the three-dimensional model still does not adequately predict the emission of the silicon nanocrystals, whereas the one-dimensional model does.

4.8 Summary and Conclusions

Two first principle models, a one-dimensional finite square well and a three-dimensional spherical well, were utilized to approximate the emission energy of Si-nc. The one-dimensional finite square well predicted the PL peak emission wavelength better than the three-dimensional spherical well, which was unexpected. However, evidence from other publications has revealed similar PL emissions between Si-nc and superlattice structures that spatially confine carriers in one dimension. Extending the one-dimensional model to all Si-nc sizes and comparing the resultant histogram to the PL emission demonstrated that the one-dimensional model did comparably well over a wider wavelength range. The major difference between the histogram and the PL emission was intensity, but silicon's indirect band gap results in different efficiencies due to nanocrystal size. Using the histogram and PL emission, it was possible to calculate the recombination strength or the efficiency of the Si-nc. The recombination strength was compared to the dispersion factor, a parameter in luminescent lifetime measurements that indicates energy migration, and both had strikingly similar results. A significant outcome from the recombination strength and dispersion factor results was the possibility of a quasi-direct transition, as predicted by Gnutzman and Clausecker [21].

For smaller nanocrystals, their recombination strength reflected the migra-

tion of energy to larger nanocrystals, which was more pronounced for the smallest nanocrystals. The recombination strength of larger nanocrystals reflected the spatial confinement of the carriers, as the nanocrystals transitioned from a bulk silicon material to a quasi-direct material. As well, the one-dimensional model and the obtained recombination strength were applied to other published TEM results, which produced better agreement for smaller nanocrystal distributions than for larger ones. The observed deviations for larger size distributions were due to a few factors. First, the accuracy of the TEM distribution is crucial in simulating the PL emission spectrum. Any difference in size or standard deviation can have a negative effect on the simulated PL emission. Surface defects or impurities appear to be participating in the emission due to the PL at wavelengths below the band gap of silicon. As well, the inclusion of the Coulomb interaction improved the agreement between simulation and experiment.

Overall, the PL can be suitably simulated by a one-dimensional model and a strong confinement regime. Although further refinement of the model can be completed with the inclusion of the Coulomb interaction, comparisons with other experimental results were acceptable, particularly for the typically reported emission wavelengths [33, 72, 79, 82–84]. Therefore, the one-dimensional model reasonably approximates the emission energies for nanocrystals with sizes of studied interest.

CHAPTER 5

Luminescence

5.1 Overview

In this chapter the photoluminescence (PL) and cathodoluminescence (CL) of Si-nc will be discussed. The first part of the chapter focuses on how the processing steps affected on the PL, particularly the growth and terminal size of the Si-nc, and the impact on the optical properties. Results and discussions on the processing steps will be related back to the previous two chapters on the growth and optical properties. The second part of the chapter will focus on cathodoluminescence. In cathodoluminescence the sample is bombarded with high energy electrons in much the same way as electroluminescent measurements, but with some differences. At first it appeared as though the second excited state of the Si-nc were being excited, but after further experiments the luminescence was concluded to originate from damage caused at the Si-nc interface by the incoming electrons. All of these results will be discussed in more detail in this chapter.

5.2 Photoluminescence

The previous two chapters examined the growth and optical properties of the Si-nc, which are responsible for the photoluminescence (PL). To relate the results from the previous two chapters to the PL requires a review of the processing steps

that affect the nucleation and growth of the Si-nc. The two most important processing steps are ion implantation and the annealing stages. The ion implantation step produces vacancy-type defects that affect the size, location, and efficiency of the Si-nc. The annealing stages act as the catalyst for the growth of the Si-nc and the reduction of defects at the Si-nc's surface. The reduction of defects permits more Si-nc to be optically active, improving the PL intensity. Both of these processing steps affect the PL and can therefore be directly linked to the growth and optical properties.

5.2.1 Implantation Dose

Implantation is a key parameter that can have a significant impact on the luminescence of the Si-nc embedded in SiO_2. Implantation creates vacancy-type defects in the SiO_2 film, which was determined in Chapter 3 to affect initial growth and, depending on the annealing gas, the final size of the Si-nc. In Chapter 4, the efficiency of the Si-nc was shown to be dependent on their size and therefore, luminescence is directly affected by the implantation dose. As such, the relationship and importance of the implantation dose to the Si-nc size distribution and the PL intensity will be discussed.

In order to examine the impact of implantation dose on the luminescence, the preparation of several samples with a range of doses was required. The samples were annealed in nitrogen gas at three different temperatures ranging from 970°C to 1170°C and for various annealing times until saturation of the PL intensity was achieved. Finally, a 1 hour anneal in forming gas at 450°C was performed after

each high temperature anneal to reduce the defects at the Si-nc's interface and to increase the number of optically active nanocrystals.

The PL intensity saturated more quickly at higher temperatures then at lower temperatures. The rapid saturation at higher temperatures is due to the mobility of excess silicon and the dissociation of nitrogen atoms. Higher silicon mobility results from higher annealing temperatures, and a faster reduction of vacancy-type defects. Greater annealing temperatures also dissociate more nitrogen atoms from the ambient gas, which passivates the defects quicker. Therefore, the PL intensity saturated more rapidly at higher temperatures.

Another noticeable difference that occurred was the PL intensity at different annealing temperatures. For the samples annealed at 1070°C, the PL intensity was greater than the samples annealed at higher or lower temperatures (illustrated in Figure 5.1). The sample's lower PL intensity when annealed at 970°C was likely due to the fact that nitrogen gas does not dissociate below 1000°C [85] and the Si particles are amorphous [64, 86]. The lack of dissociated nitrogen atoms hinders the passivation of defects and amorphous Si particles have been shown to be less efficient [64, 86]. The sample annealed at 1170°C had a lower PL intensity, which was possibly due to the formation of larger Si-nc. The formation of larger Si-nc would result in fewer Si-nc and possibly less efficient ones depending on their recombination strength. The size and number of optically active Si-nc can be investigated further by relating the PL spectrum to the Si-nc size distribution.

The size of the Si-nc can be calculated from the PL emission by interpolating the diameter from an array of emission wavelengths versus diameter values calculated

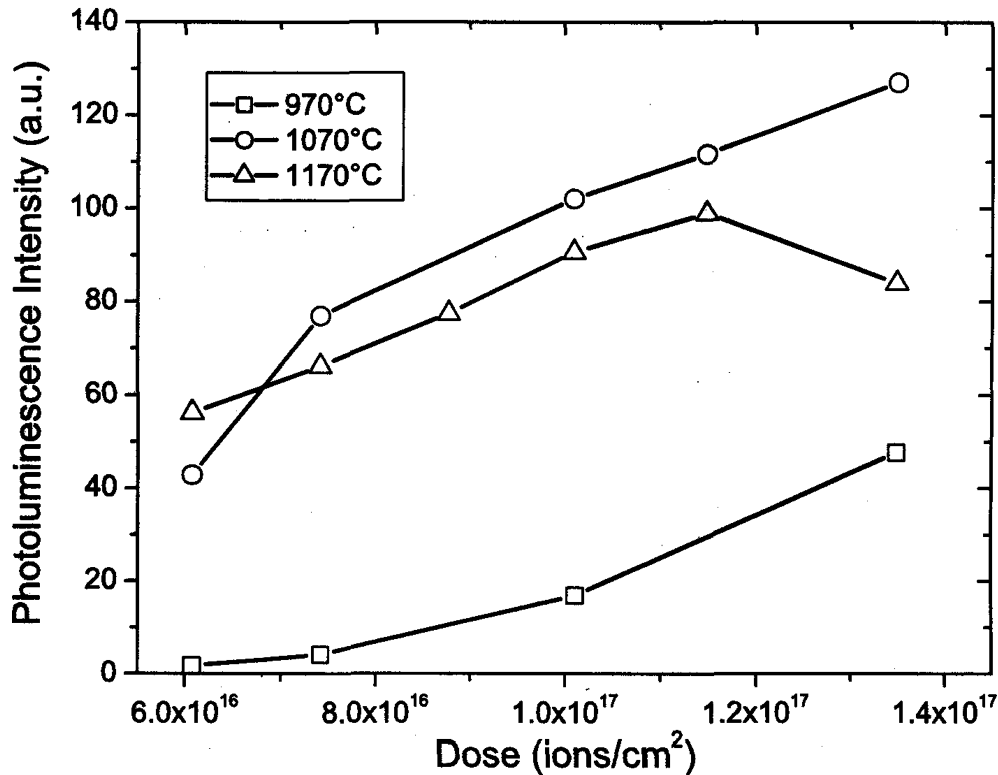

Figure 5.1: PL intensity for samples implanted with different doses of Si. The samples were annealed at 970°C for 10 hrs, 1070°C for 3 hrs, or 1170°C for 15 min. All samples after the high temperature anneals were annealed at 450°C in a mixture of hydrogen and nitrogen.

from Eqs. (4.3) and (4.4) in Chapter 4. The number of optically active Si-nc of a given size can be estimated by multiplying the PL intensity with its corresponding Si-nc size, which provides an effective size distribution. Figure 5.2 illustrates two size distributions determined from the PL intensity and provides insight into the results plotted in Figure 5.1. The key parameters from all the interpolated PL emissions are summarized in Table 5.1.

One of the first parameters to look at is the peak nanocrystal size and how it compares with the peak PL wavelength because they should be connected. In Figure 5.3 both the peak nanocrystal size and peak PL wavelength have very similar trends and the quantum confinement emissions are very similar. A larger nanocrystal size

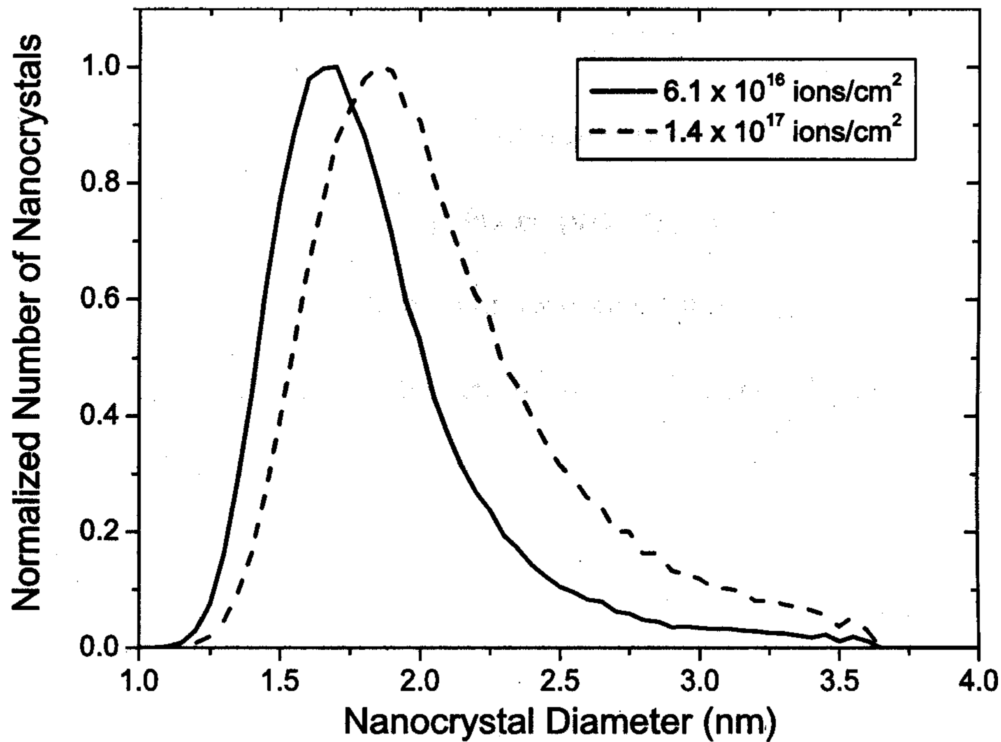

Figure 5.2: Theoretical size distribution that emits light for samples implanted at 90 keV, and doses of 6.1×10^{16} ions/cm^2 and 1.4×10^{17} ions/cm^2. Both samples were annealed at 1170°C for 15 min and at 450°C for 1 hr in a mixture of hydrogen and nitrogen.

Table 5.1: A comparison of the important factors that affect the PL intensity for samples annealed at 1070°C for 3 hrs and 1170°C for 15 min. The values are calculated by converting the PL emission energy into the Si-nc distribution that emits light. Peak size refers to the mode of the distribution and FHWM stands for full width half maximum. The size distribution gets cut off at nanocrystal sizes greater than 3.5 nm due to the detector wavelength limit of 1000 nm.

Dose ($\times 10^{16}$ cm^{-2})	Peak Size (nm)		FWHM (nm)		Number of Si-nc (Normalized)	
	1070°C	1170°C	1070°C	1170°C	1070°C	1170°C
6.1	1.62	1.73	0.58	0.66	0.31	0.42
7.2	1.67	1.76	0.61	0.71	0.55	0.51
8.8		1.77		0.71		0.59
10	1.76	1.82	0.68	0.78	0.76	0.70
12	1.79	1.84	0.82	0.80	0.92	0.78
14	1.87	1.91	0.81	0.94	1	0.69

occurred at higher doses which is anticipated because more vacancy-type defects are created, allowing larger nanocrystals to form as described in Chapter 3. As well, larger nanocrystals occurred at higher annealing temperatures because the silicon atoms are able to diffuse further and faster prior to the minimization of vacancy-type defects. The results in Table 5.1 can also give some explanations as to the PL intensity declining at 1170°C for the largest dose in Figure 5.1. The decline can be explained by the Si-nc size distribution and the number of nanocrystals.

As the nanocrystals become larger, they consume more silicon atoms at a rate proportional to d^3 (where d is the nanocrystal diameter) [34, 87]. For example, a nanocrystal 2 nm in diameter requires twice as many atoms as a nanocrystal 1.6 nm in diameter. The increased appetite of the larger nanocrystal indicates that twice as many smaller nanocrystals can be formed with the same amount of atoms. Depending upon the efficiency of the nanocrystals, doubling the number of nanocrystals can have a significant impact on the PL intensity even with a minor change in the nanocrystal diameter. The PL intensity was also lower at the higher annealing temperature due to the broader size distribution of nanocrystals (demonstrated in Table 5.1). Broader size distribution exacerbates the reduction in the number of nanocrystals by consuming even more atoms. The combination of the larger nanocrystal sizes and broader size distributions at the highest doses and annealing temperatures eventually reduced the number of optically active Si-nc, resulting in a decline in the PL intensity.

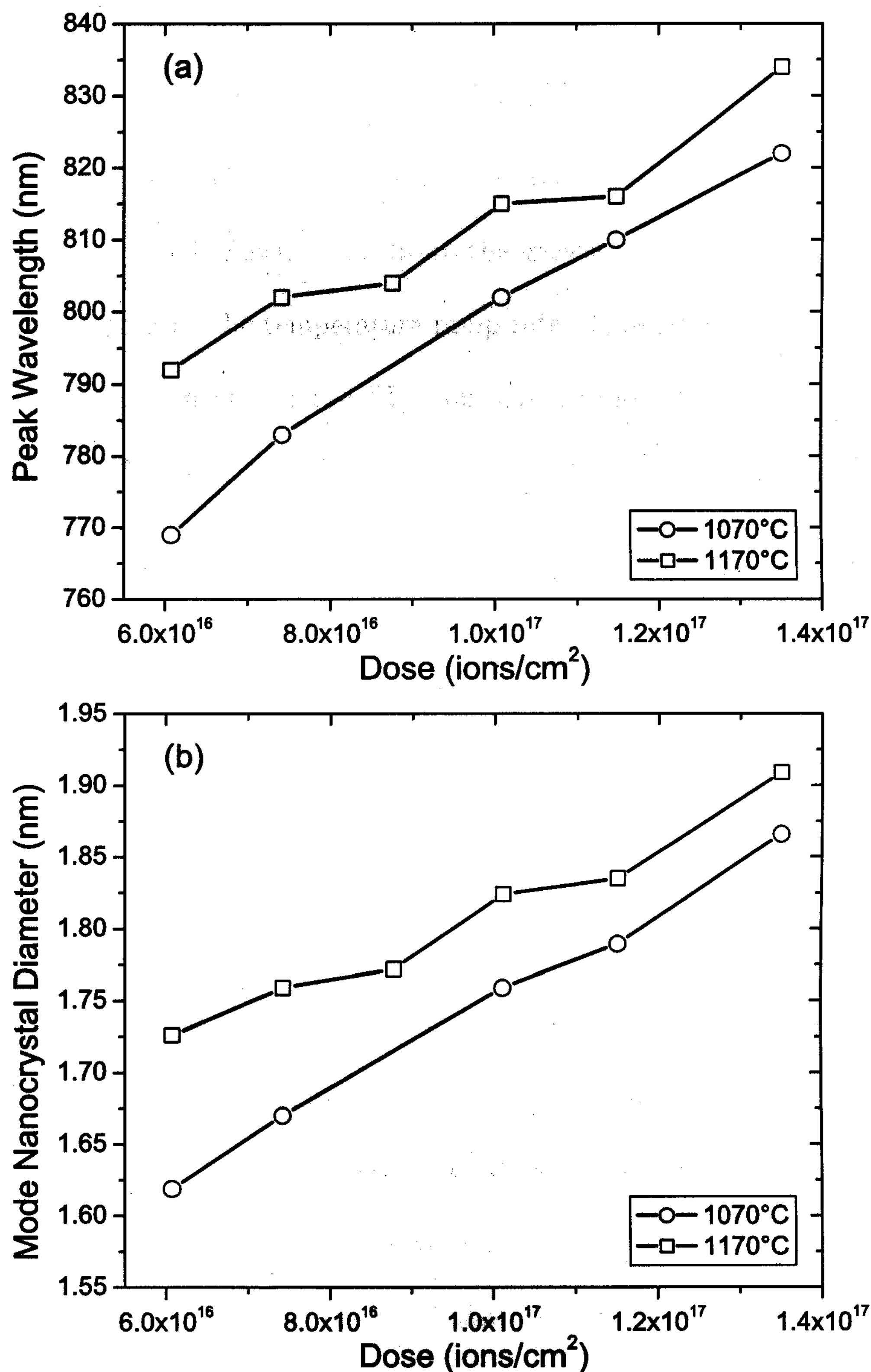

Figure 5.3: (a) the PL peak wavelength and (b) the mode for the nanocrystal size of samples annealed at 1070°C for 3hrs and 1170°C for 15 min in nitrogen, followed by a 1 hr hydrogen anneal.

5.2.2 Annealing

The annealing stages are critical processing steps that affect the Si-nc growth and the reduction of defects at the interface between the Si-nc and SiO_2. Vacancy-type defects have been shown to facilitate the growth of nanocrystals, which is a fast process affected by the temperature ramp rate. Thus, the two commonly used annealers and their effects on the PL intensity are discussed. The reduction in defects allows additional Si-nc to be optically active, and so three of the commonly used gases in silicon processing and their impact on the luminescence will also be discussed.

5.2.2.1 Furnace versus Rapid Thermal Annealing

Two types of annealers are generally used in silicon processing: a furnace and a rapid thermal annealer (RTA). In a furnace the sample's temperature increases gradually, whereas in the rapid thermal annealer (RTA) the temperature increases much quicker, as suggested by the name. In addition, the temperature ramp rate can be better controlled in a RTA. It has already been discussed in Chapter 3 that the diffusion of silicon in SiO_2 is very slow [49] and that the initial growth of the nanocrystals is greatly affected by the vacancy-type defects introduced by the ion implantation. As well, it was suggested that the vacancy-type defects facilitate the silicon atom diffusion required for the ripening of the Si-nc. Therefore, the temperature ramp rate should affect the growth and PL.

A comparison of the PL intensity between similar samples, one annealed in a furnace and the other in an RTA (Figure 5.4), revealed a significant difference.

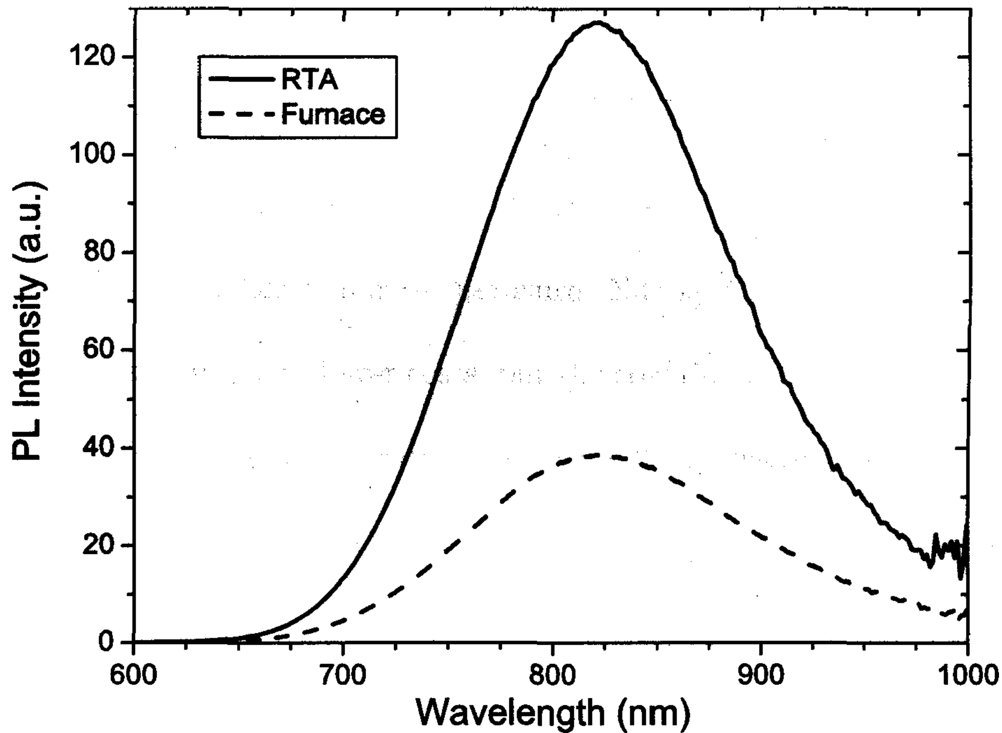

Figure 5.4: PL intensity of similar samples annealed in a furnace or an RTA at 1070°C for 3 hrs. Both samples were annealed at 450°C for 1 hr in forming gas to reduce additional dangling bonds. The RTA ramp rate was 100°C/s.

The PL intensity from the sample annealed in the RTA was more than three times higher than the one annealed in the furnace. Iwayama *et al.* [88] observed similar differences between the furnace and RTA anneals. In addition, the two samples had similar PL spectrum shapes and peak PL wavelengths, suggesting that more nanocrystals were formed for the sample annealed in the RTA. In other words, more silicon atoms are allowed to diffuse and form nanocrystals before the vacancy-type defects have been annealed away in the RTA process. In contrast, the nanocrystal growth is slower in the furnace process and results in fewer nanocrystals. This has significant implications on the thermal budget utilized in the formation and luminescence of nanocrystals, which will become more evident after the discussion in the next two sections on the annealing gases.

5.2.2.2 Nitrogen and Argon

Nitrogen or argon gas are typically utilized in silicon processing with high temperature anneals. The choice of gas depends on two factors: the cost and the inertness of the gas at a particular temperature. Nitrogen gas was originally utilized more often than argon due to lower costs, but the cost differences have been reduced. The key concern with high temperature anneals is the inclusion of dissociated atoms from the ambient gas into the annealed material and their effect on the overall performance. Early studies of SiO_2 films showed that annealing in nitrogen gas for temperatures above 1000°C reduced the fixed oxide charge [85]. The reduction was due to the inclusion of nitrogen at the interface between the Si/SiO_2 creating a thin oxynitride layer that reduced the number of dangling bonds [89, 90]. Conversely, argon gas is relatively inert at high temperatures and will incorporate negligible amounts of argon in the film. Therefore, the dependence of the PL intensity on the annealing gas has been investigated and will be discussed further.

Wilkinson and Elliman [46] investigated the affect of the annealing gas on PL intensity and nanocrystal size. They observed that the PL intensity was stronger for samples annealed in nitrogen than in argon and the difference increased with longer anneals. As well, the peak wavelength red-shifted in argon after a long anneal time and in nitrogen the peak wavelength remained relatively stable. Through Raman spectroscopy it was demonstrated that larger nanocrystals had formed in the sample annealed in argon after a long annealing time. The increases in nanocrystal size could explain both the red-shift and lower PL intensity. Larger nanocrystals emit

photons closer to the band gap energy resulting in the red-shift, and the lower PL intensity is caused by the formation of fewer nanocrystals since larger nanocrystals require more atoms [34, 87], and are potentially less efficient. Wilkinson and Elliman [46] concluded that the inclusion of nitrogen gas formed oxynitride layers at the interface of the nanocrystals. These oxynitride layers thermally relaxed the bonds and reduced the interface defects, which resulted in smaller nanocrystals and improved PL. These findings are consistent with earlier studies of SiO_2 films, and the relationship between the nitrogen content and PL intensity can be investigated further.

The dependence of the PL intensity on nitrogen content can be investigated through the implantation of nitrogen ions since the dose can be accurately measured. Four samples were prepared; two that were implanted with nitrogen ions and another two that were not. Samples were annealed in either argon or nitrogen gas at a temperature of 1100°C for 1 hr. Figure 5.5 illustrates that the samples implanted with nitrogen ions had a stronger PL signal than their non-implanted counterparts, and the PL intensity was stronger for the samples annealed in nitrogen gas. Since the PL's peak wavelength and shape are very similar in all four samples, the effect of the included nitrogen atoms in the film from both the implanted ions and from the ambient gas on the PL intensity can be analyzed. It is assumed that each sample annealed in nitrogen gas had a similar amount of nitrogen incorporated in the film. The difference in intensity in Figure 5.5 between the nitrogen implanted sample and the non-implanted sample annealed in argon is greater than the samples annealed in nitrogen. The smaller difference in intensity for the samples annealed in nitrogen

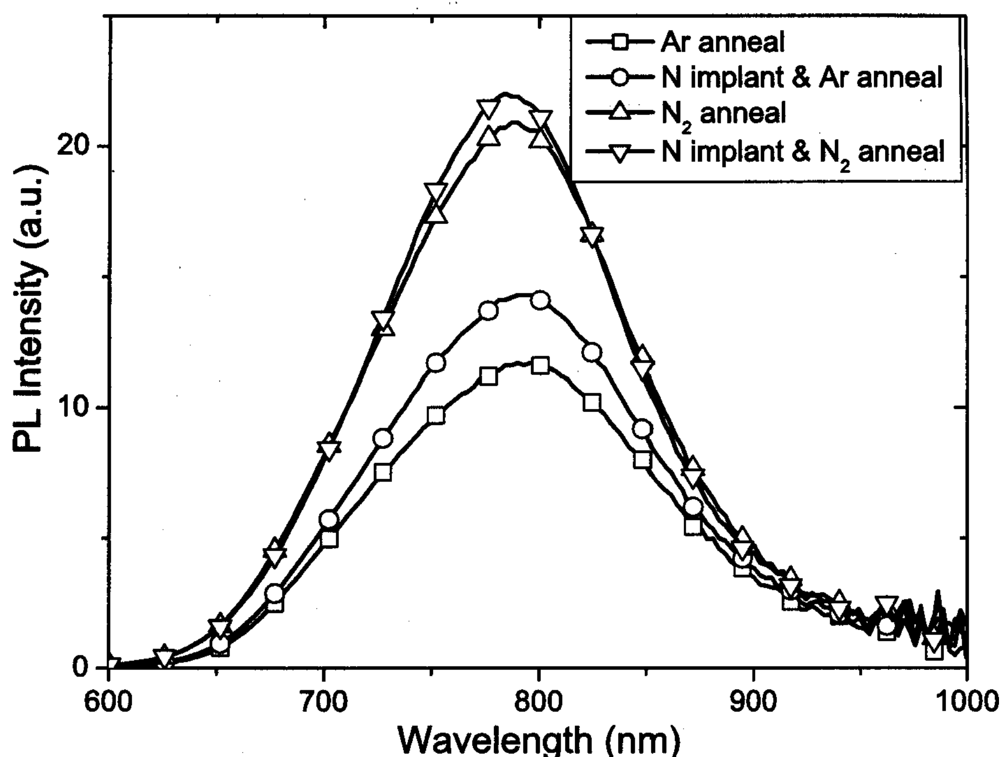

Figure 5.5: PL intensity of two samples annealed in either argon or nitrogen at a temperature of 1100°C for 1 hr. All samples were implanted with silicon at 425 keV and a dose of 1×10^{17} ions/cm^2, and two of the samples were implanted with nitrogen at 250 keV and a dose of 5×10^{14} ions /cm^2.

is due to the defects at the nanocrystal interfaces being sufficiently passivated by nitrogen. At 1070°C, the PL intensity saturates after approximately a 3 hour anneal, and at 1170°C saturation occurred within 15 minutes (as shown in Figure 5.6).

The inclusion of nitrogen atoms either from ion implantation or the dissociation of the ambient nitrogen gas into the silicon rich oxide film reduced the number of defects at the nanocrystals' interfaces, which permitted more nanocrystals to be optically active. It also needs to be mentioned that the nitrogen implant adds vacancies, but the effect of that is likely small due to a small dose. Annealing in inert argon gas was less effective in improving the PL than annealing in nitrogen gas because of the lack of defect reduction and the increase in nanocrystal size after long anneals. Nonetheless, annealing in nitrogen has its limitations and eventually

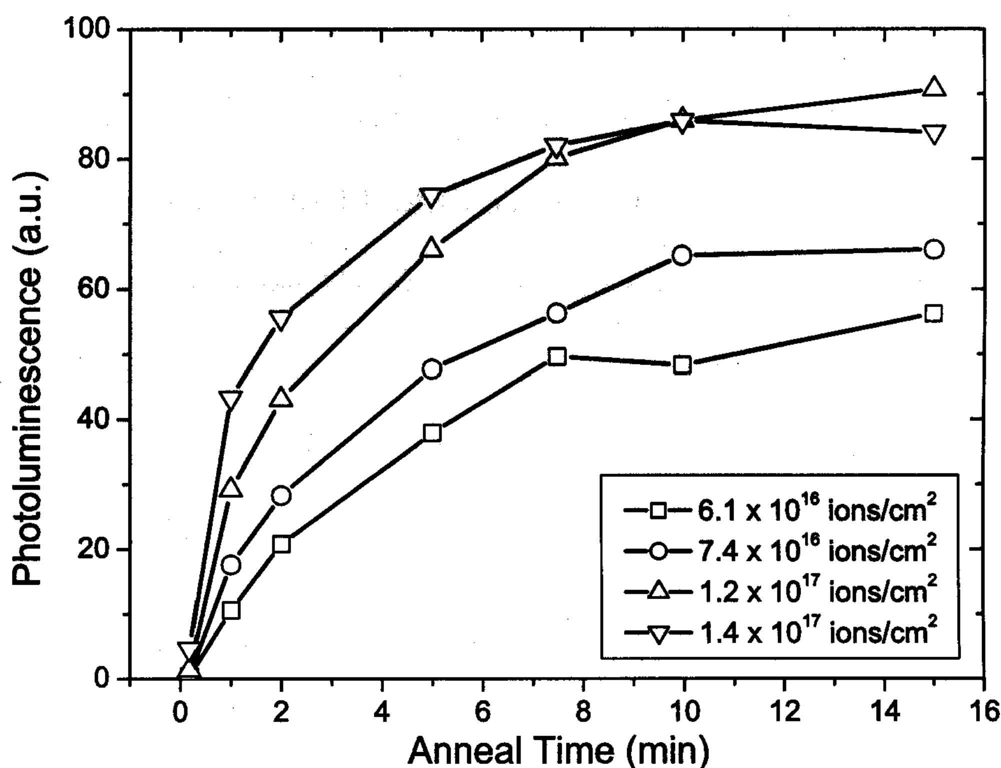

Figure 5.6: Evolution of the PL intensity for various Si implant doses at an anneal temperature of 1170°C in nitrogen.

results in a saturation point. However, improvements can be gained by annealing in hydrogen gas, which was observed in early device fabrication.

5.2.2.3 Hydrogen

Initially during silicon device operation, the defects at the Si/SiO_2 interface would trap electrons or holes and hinder performance. Through a low temperature anneal in hydrogen gas, a reaction at the interface causing Si-H bonds to form was observed and rendered the defects electrically inactive [91]. As such, hydrogen gas is presumed to improve the PL in nanocrystals by rendering defects inactive and allowing more nanocrystals to emit light. This improvement is potentially still achievable even after a nitrogen anneal because remaining defects may be passivated by a hydrogen atom that requires only one bond, compared to three bonds for

nitrogen.

Wilkinson and Elliman [82, 92], have reported extensive work on the effects of hydrogen annealing on the PL of silicon nanocrystals. They observed that the PL intensity improves depending on temperature and on how the hydrogen is introduced during the annealing process. The optimal annealing temperature was found to be 500°C since the absorption and desorption of hydrogen are at their highest and lowest at this temperature. Figure 5.7 illustrates how the inclusion of hydrogen into the silicon rich oxide can improve the PL intensity. Also, the method by which the hydrogen atoms are introduced into the material can affect the PL intensity. Atomic hydrogen introduced through either implantation or other processing steps bonds readily to defects present at the interface between Si and SiO_2. In contrast, molecular hydrogen introduced through the ambient gas requires a reaction to occur and is not able to react with all non-radiative defects [92]. As such, atomic hydrogen removes substantially more defects, which allows additional nanocrystals to be optically active.

The benefit of annealing with hydrogen gas is not limited to the PL intensity. Additional benefits include longer radiative lifetimes and larger dispersion factors. Longer radiative lifetimes are an important benefit in regard to laser technology since population inversion is required and is easier to achieve with longer radiative lifetimes. Longer radiative lifetimes arise in Si-nc because the fast non-radiative defects are reduced improving the probability that a photon will be emitted. An increased dispersion factor is also advantageous because it indicates a lack of migration channels for the electrons and/or holes to non-radiative processes [92].

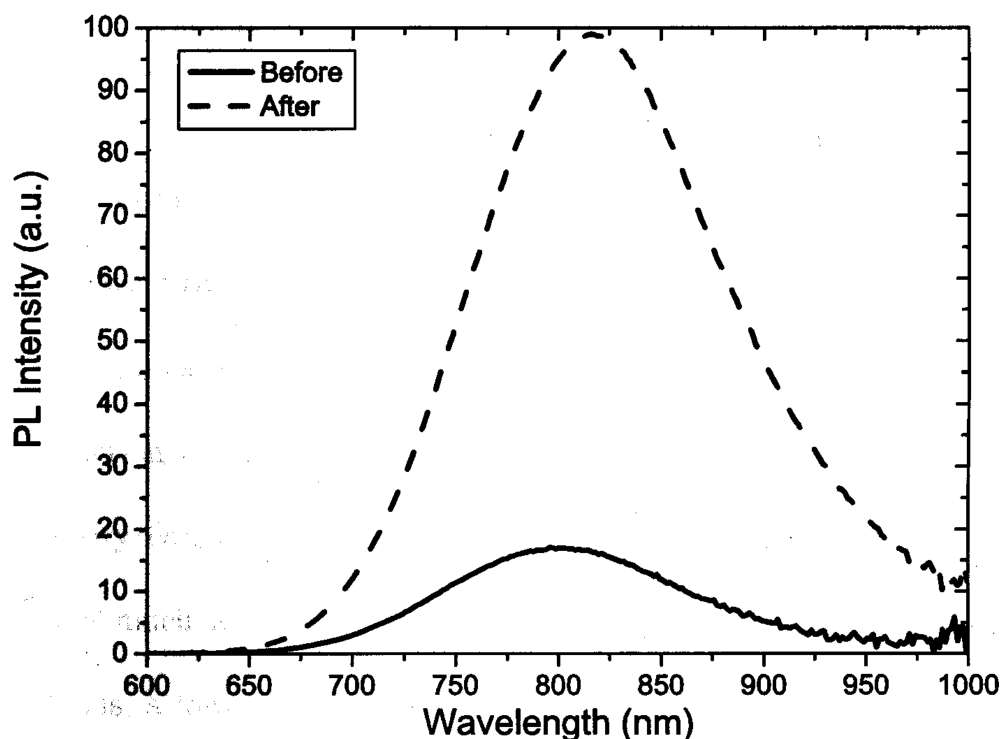

Figure 5.7: PL intensity before and after a 1 h anneal at 450°C in forming gas (5%H_2 95%N_2). The sample was implanted at 90 keV, a dose of 1.2 × 10^{17} Si ions /cm^2 and annealed at 1170°C for 15 min.

5.2.3 Photoluminescence Conclusions

In summary, implantation dose impacted the PL intensity by influencing the vacancy-type defects, which in Chapter 3 was shown to affect the nanocrystal size and distribution. The nanocrystal size increased with dose and annealing temperature, and the distribution broadened at higher temperatures. Increasing the dose and distribution resulted in large nanocrystals that required many more atoms, eventually reducing the overall number of Si-nc that emitted light and led to a reduction in PL intensity. As well, the larger and broader distributions had less efficient nanocrystals according the results found in Chapter 4, which contributed to the eventual reduction in PL intensity.

The photoluminescence of Si-nc is also strongly affected by the choice of the

annealer and annealing gas. The rapid thermal annealer allowed more silicon atoms to form nanocrystals which resulted in a higher PL intensity compared with samples annealed in a furnace. The choice of gases (i.e., argon, nitrogen, and hydrogen) utilized in silicon processing also affected the luminescence of Si-nc. Argon, an inert gas, does not achieve results approaching that of nitrogen gas due to a lack of defect reduction and the tendency to create larger nanocrystals. Additionally, the PL intensity can be enhanced further after the initial anneal in nitrogen by annealing at a much lower temperature with hydrogen, because of further defect reduction. Thus, a lower thermal budget can be achieved by annealing in an RTA with nitrogen gas, promoting the growth of the most nanocrystals, followed by an anneal at a lower temperature in hydrogen removing the defects at the surface of the nanocrystals.

5.3 Cathodoluminescence

Several methods for achieving a silicon light emitting device have been published [72, 93–95], some of which use Si-nc embedded in SiO_2. Most of the devices utilizing Si-nc excite them through impact ionization in the electroluminescence (EL) measurements. Impact ionization is a process whereby the injected electrons excite the material's electrons from the valence band to the conduction band, resulting in electron-hole pairs that can recombine to emit light. Cathodoluminescence (CL) also excites Si-nc by using electrons, but with slight differences between the two excitation techniques. The applied voltage in an EL measurement is much smaller than that applied in a CL measurement, and an electric field is present in an EL

measurement. Nevertheless, the excitation method for CL and EL measurements are similar and therefore, it is fascinating to probe the Si-nc by CL.

Exciting the Si-nc with a beam current of 0.6 mA at an energy of 6 keV revealed that the CL emission spectrum is dramatically different from the PL spectrum shown in Figure 5.8. This result is unexpected because it has been reported that the emission in EL measurements are similar to PL measurements [93, 96]. However, the difference between the two spectra can potentially be explained two ways. First, if enough electrons and holes occupy the first excited state of a Si-nc, then the second excited state can be observed. CL measurements are made with higher excitation intensities than either PL or EL measurements, possibly leading to the emission from the second excited energy state. Calculating the second excited energy state using Eq. (4.3) in Chapter 4 results in an emission centered near 450 nm, close to the emission observed in Figure 5.8. A second possibility is that the electron beam in a CL measurement creates and/or excites luminescent defects at the interface of the Si-nc. Either possibility can be explored further through the exposure of the sample to smaller beam currents.

Observing the changes in CL emission with smaller beam currents and exposure times can indicate the mechanism responsible for the CL emission. At lower beam currents two emission peaks are distinguishable, one centered at 450 nm and the other at 650 nm (illustrated in Figure 5.9). These emissions are consistent with other CL measurements [97–99]. Even though the emission at 650 nm is strongest at the lowest beam currents, the 450 nm emission becomes stronger at higher beam currents. As well, the longer the sample is exposed to the electron beam the stronger

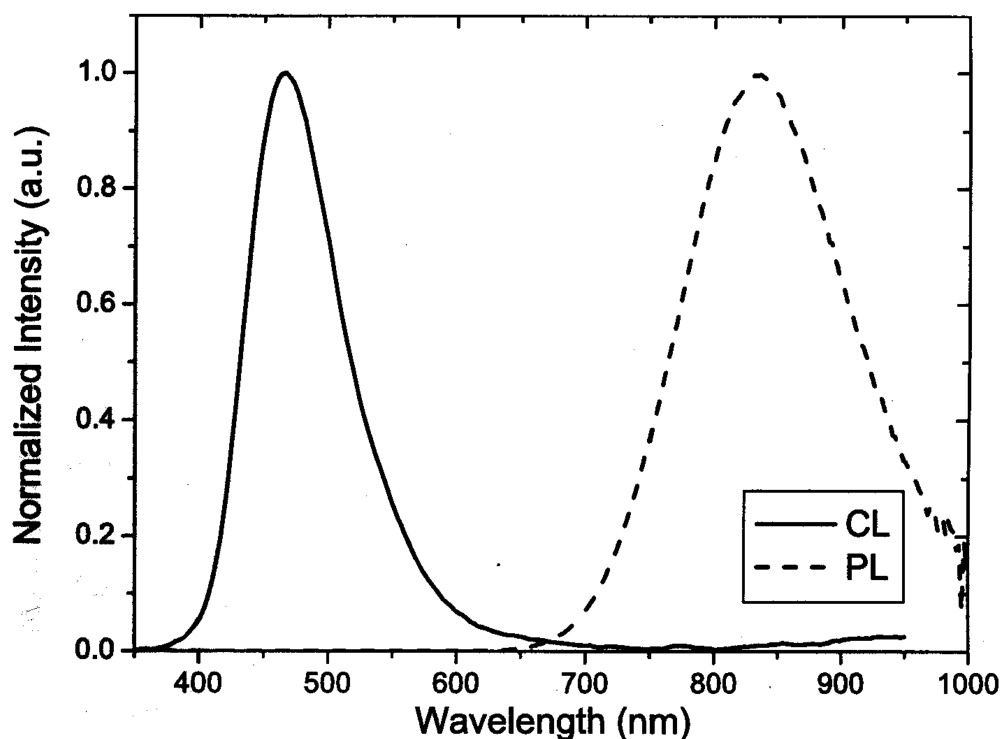

Figure 5.8: CL and PL emission spectra for a sample implanted at 90 keV and a dose of 1.4 × 10^{17} ions/cm^2. The sample was annealed in nitrogen at 1170°C for 15min followed by a passivation anneal at 450°C for 1 hr. The CL measurement was done at an energy of 6 keV with a 0.6 mA electron beam current. The CL emission was smoothed for clarity.

the emission at 450 nm becomes (Figure 5.10). If the emission was due to excited states, these results would indicate that: the first excited state was filling up allowing the second excited state to be observed; and the rate of excitation is faster than the radiative recombination rate. However, the results after long exposure times and large currents can also be explained by increased damage to the sample, creating more luminescent defects. Determining whether these results are related to the excited states or to defects can be accomplished with a straightforward experiment described below.

Multiple CL measurements of one region in a sample containing Si-nc, but changing the exposure time can determine which of the two possibilities is responsible for the observed CL emission. The first measurement was obtained after the

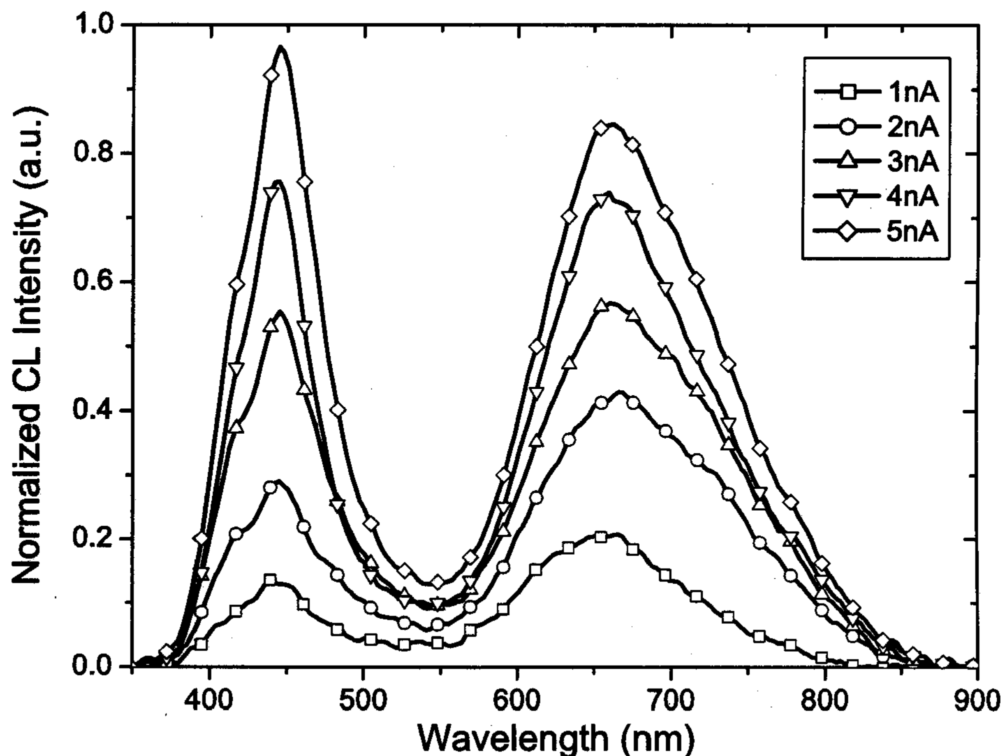

Figure 5.9: A 10 keV CL measurement with various target currents measured by a Faraday cup. The sample was implanted at 90 keV and a dose of 1.4 × 10^{17} ions/cm^2.

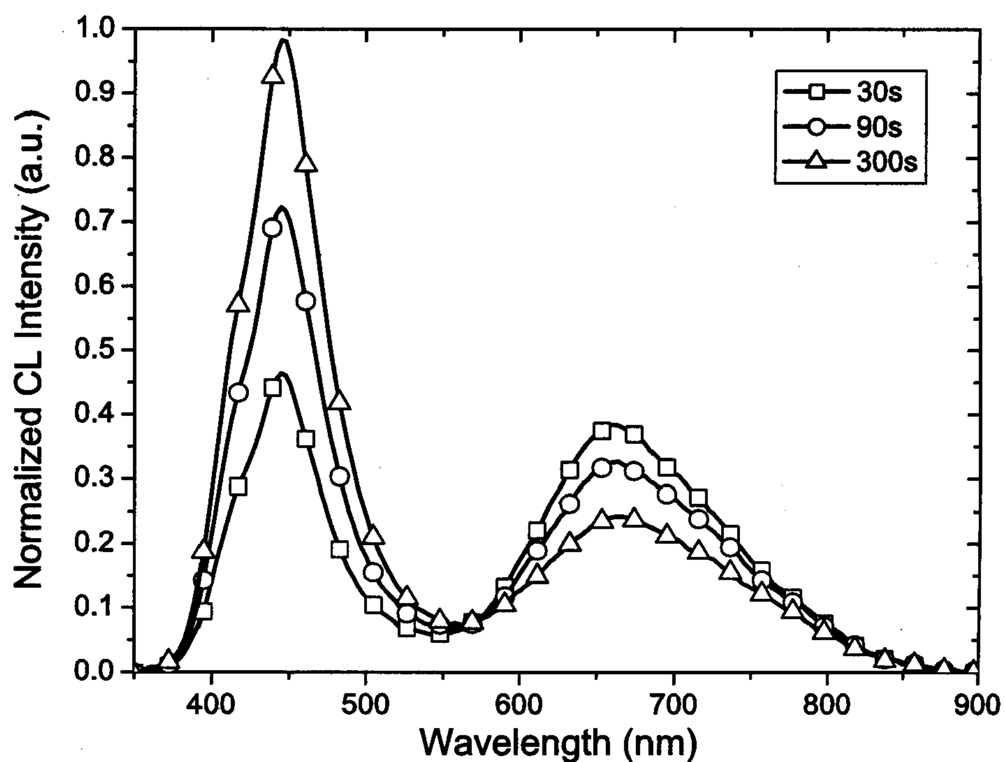

Figure 5.10: A progression of the CL at 10 keV with a target current of 5 nA.

sample had been exposed for 300 s with a beam current of 5 nA. The electron beam was then moved to another location for 300 s, allowing the region where the first measurement was collected to relax to its unexposed state. The second measurement was obtained in the same region as the first measurement, but exposed instead for 30 s. If the CL emission observed was due to the second excited state, then the second measurement would produce a spectrum similar to that measured after 30 s in Figure 5.10, because the excited states depopulate during the relaxation period and repopulate when exposed again. If the CL emission was due to defects, the second measurement would be identical to the first measurement because the beam would have caused irreparable damage. The results of the second measurement are identical to the first measurement, revealing that the emission spectrum measured at 450 nm was due to defects.

Additional evidence that the CL emission is caused by defects is provided during the ion implantation process where a blue emission at approximately 450 nm is clearly visible (Figure 5.11). The visible blue emission during the implantation process is likely due to defects because the nucleation of excess Si at room temperature is extremely small and the positron annihilation spectroscopy (PAS) measurements revealed numerous vacancy-type defects. However, the CL emission at 650 nm decreased with exposure to the electron beam, which is contrary to the defect emission at 450 nm. Thus, the luminescence at 650 nm needs to be investigated further.

Although it has already been demonstrated that the CL emission at 450 nm was due to defects, the results were inconclusive for the CL emission at 650 nm. The types of defects introduced into SiO_2 during ion implantation, some of which

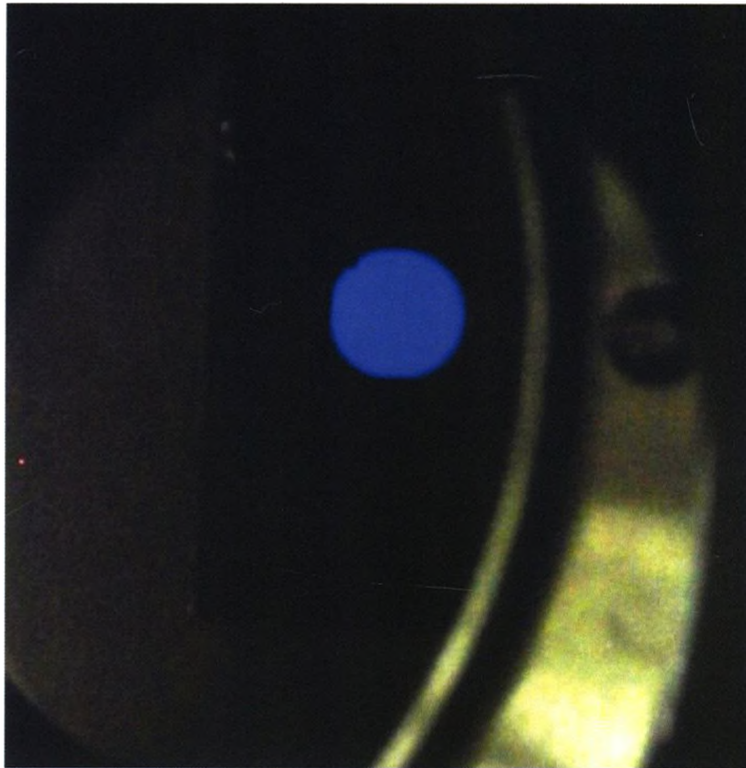

Figure 5.11: Picture of a sample during implantation emitting light in the blue region of the visible spectrum.

luminesce, were briefly discussed in the PAS section of Chapter 3. The luminescent defects in SiO_2 and their emission energies are tabulated in Table 5.2 and some of the luminescent defects are tentatively identified in Figure 5.12. The PL measurement after implantation demonstrates defect related emission centered at both 450 and 650 nm, similar to the CL emission. As well, Pillai *et al.* [98] obtained CL measurements from porous silicon with peaks at both 450 and 650 nm, and discovered that after the samples had been etched in hydrofluoric acid, the CL emission was extremely weak while the PL emission did not change. This experiment's results strongly support the theory that the CL emission at 650 nm is due to the oxide related defect rather than the Si-nc.

Table 5.2: List of luminescent defects in SiO_2 [100].

Defect Type	Energy (eV)	Wavelength (nm)
NBOHC	1.91 - 1.96	636 - 650
Self trapped exciton	2.2 - 2.4	517 - 564
E' centre	2.72 - 2.95	420 - 455
Al centre	3.12	397

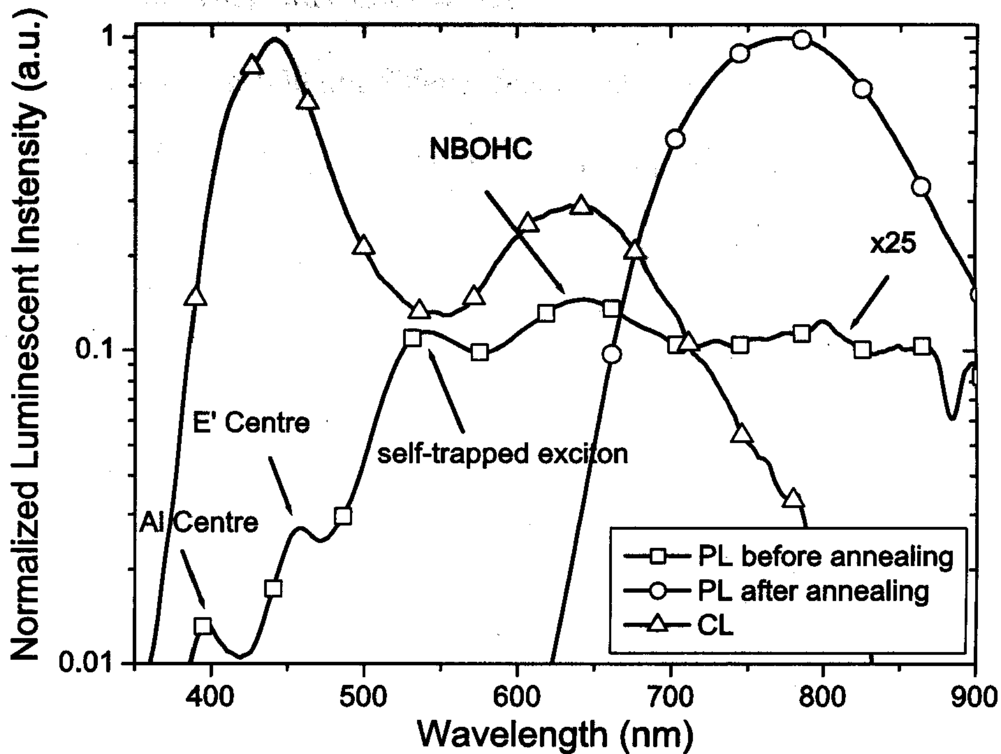

Figure 5.12: Comparison of defects excited by PL and CL. The two PL measurements are from the same sample. The first PL measurement was taken after the ion implantation stage and the other PL measurement was measured after a nitrogen and hydrogen anneals. The sample had a 1 μm thick oxide layer implanted at 450 keV and a dose of 1×10^{17} ions/cm^2. The sample was annealed at 1070°C in nitrogen gas and 450°C in 5%H_2 95%N_2. The CL measurement was done at 10 keV with an electron beam current of 5 nA. All the curves were smoothed for visual clarity.

5.3.1 Cathodoluminescence Conclusions

The cathodoluminescence (CL) measurements excited the Si-nc with energetic electrons much like electroluminescence (EL). With large electron beam currents, an emission spectrum centered at 450 nm is observed and a second emission centered at 650 nm is also observed at lower currents. These two emission peaks differ from

PL and EL measurements and are caused either by the emission from the second excited energy state or by defects. An experiment was completed where the CL spectrum was measured in one region with different beam exposure times. It was concluded that the emission at 450 nm was caused by defects and that the increase in the emission intensity was due to damage from the electron beam exposure. However, the emission at 650 nm differed from that at 450 nm and prompted further investigation. Pillai *et al.*'s CL experiment in porous silicon demonstrated that after a hydrofluoric acid etch, the CL emissions disappeared while the PL emission remained, which confirmed that the emissions were caused by SiO_2 defects. Thus, the CL measurements damaged and created defects in the sample that were excited by the incident electron beam.

CHAPTER 6

Conclusions

The microelectronics industry has followed Moore's law since 1965, whereby the number of transistors on a microchip doubles every two years. Although the challenge in maintaining Moore's law has traditionally been in reducing the size of the transistors, the International Technology Roadmap for Semiconductors (ITRS) has in the past few years highlighted interconnections between the transistors as another challenge. The challenge regarding the interconnections between the transistors is exacerbated as the size of the transistors decrease and there is no long term solution beyond 2010. Nevertheless, a potential solution is the integration of optical interconnects on a microchip, which would solve most, if not all, the problems associated with their metallic counterparts.

Most photonic devices used in the telecommunications industry are made of III/IV semiconductors that cannot be easily reduced in size, are expensive, and are not particularly compatible with silicon. Even though silicon would be the ideal material for integrating photonic devices on a microprocessor, its indirect band gap makes it a poor emitter of light. A solution for overcoming silicon's indirect band gap is through nanostructured materials that enhance the probability that a radiative recombination will occur.

In the early 1990's, L. T. Canham proposed that large and numerous holes in silicon would result in quantum confinement effects that improve the radiative

recombination of silicon. Canham's hypothesis was proven correct and initiated an interest in silicon photonic devices and a silicon laser. Some of the interest focused on silicon nanocrystals embedded in silicon dioxide because they utilize the quantum confinement effects produced through the difference in the two materials' band gaps.

With interest in silicon nanocrystals and a silicon laser, this thesis has focused on experimental and theoretical work to enhance and increase the comprehension of silicon nanocrystals' (Si-nc) material properties. The growth and optical properties of Si-nc were examined in greater detail since they are essential for developing a silicon light emitter.

The growth of Si-nc was examined through numerous experimental techniques and simulations to identify the mechanism responsible for the growth. A correlation was observed between the vacancy-type defects created by ion implantation and the growth of the Si-nc. This correlation had not previously been observed and has implications for the manipulation of the nanocrystals' optical characteristics for various applications. Experiments were performed to support the correlation and to illustrate its potential benefit. A sample was implanted twice, with the first implant deep in the material and the second implant shallow. The deep implant affected the shallow implant's vacancy-type defect distribution allowing larger nanocrystals to grow, which was reflected in the photoluminescence measurements. These results supported the preceding correlation and the potential to manipulate the growth of nanocrystals in a particular region.

Additionally, the relationship between the nanocrystal size obtained from transmission electron microscopy and emission wavelength from PL measurements

was explored. The images revealed that previous theoretical work overestimated the nanocrystals' emission energy and that a simple one-dimensional model can reasonably predict the emission energy. Even though nanocrystals are three-dimensionally confined, previously published results provided supporting evidence for the validity of a one-dimensional model. Through the application of the one-dimensional model to the nanocrystal size distribution, the recombination strength or the efficiency of the nanocrystals was determined and the results were similar to those published on one-dimensional structures. In addition, luminescent lifetime measurements and optical gain measurements in other published work supported the recombination strength. The establishment of a reasonable emission energy model and recombination strength permitted the simulation of photoluminescence from other published TEM size distributions. The results were in good agreement at lower emission wavelengths and deviated at wavelengths greater than 950 nm. Nonetheless, the majority of published results with the highest intensities occurred at lower wavelengths, which implies that the one-dimensional model and recombination strength are appropriate for the emission wavelengths of interest.

The results obtained regarding the growth and optical properties of silicon nanocrystals allowed for the analysis of the relationship between photoluminescence and processing parameters. It was discovered that the peak photoluminescence wavelength shifted with an increase in dose and/or annealing temperature due to the increase in the nanocrystal size. As well, the photoluminescence intensity increased with increasing dose until the nanocrystals' average size was large enough that fewer nanocrystals were formed due to the fact that larger nanocrystals require

more silicon atoms and are less optically efficient. When this point was attained, the PL intensity decreased. In addition, cathodoluminescence measurements were performed and produced different results than the photoluminescence measurements. Initially there were two potential explanations for this variation, but upon further investigation it was concluded that the emission was caused by defects at the surface of the nanocrystals.

All the experimental and theoretical work performed in this thesis regarding the growth and optical properties of Si-nc are valuable tools for future analysis of Si-nc. Based on the results obtained from the growth of the Si-nc, it was demonstrated that the growth of the nanocrystals can be modified to affect the emission wavelength and intensity. As well, the changes in photoluminescence with varying process parameters can be better understood with a simple theoretical model. Therefore, the results attained in this thesis allow for future enhanced analysis and manipulation of Si-nc in silicon dioxide.

APPENDIX A

Modeling PAS Results

PAS measurements were modelled and fitted using the program POSTRAP5 [57], which can provide insight into the material properties. A simple model was applied by dividing the oxide film into three regions, except for the reference SiO_2 which had two regions. Only two parameters were altered per region (i.e., thickness and diffusion coefficient) with the diffusion coefficient maintained between 0.0020 and 0.0143 cm^2/s, which are typical values for positrons in SiO_2 [101]. An illustration of the model and a description of each region is depicted in Figure A.1. In all the models the Si/SiO_2 interface was included because it effectively trapped positrons and significantly improved the fit of the model even though the thickness of the interface was only 1 nm. To maintain consistency the parameters obtained in fitting the reference SiO_2 for the interface and oxide region were kept identical for the implanted and annealed samples. As such, for the implanted and annealed samples only the thickness and diffusion coefficient in the implanted region were changed and all other parameters remained consistent between samples. Results of the S-parameter fitting are summarized in Table A.1 and the fits are shown in Figure 3.9. Figure 3.9 demonstrates that the model was a good representation of the materials properties and can be used for some important comparisons between the PAS measurements and the TEM images.

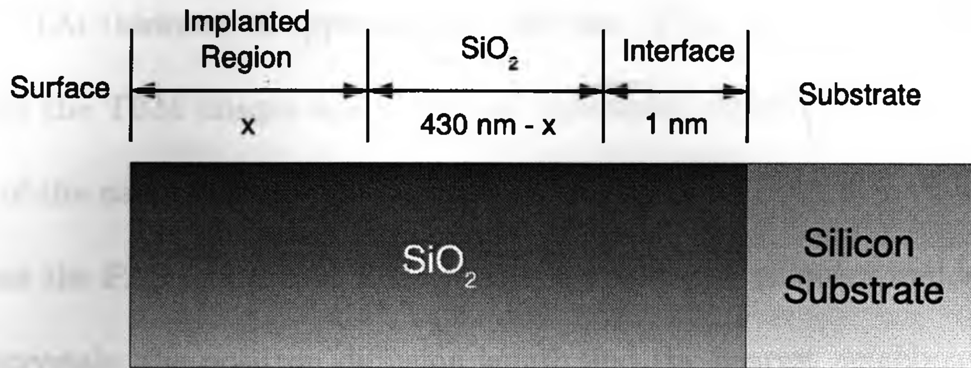

Figure A.1: Model used in POSTRAP5 to fit the PAS results for the implanted and annealed samples.

Table A.1: Normalized S-parameter values simulated by POSTRAP5 for PAS data collected from the 430 nm thick SiO_2 film implanted at 90 keV and a dose of 1.4×10^{17} ions/cm^2. Sample (A) reference SiO_2 film, (B) as-implanted film, (C) annealed 10 sec. at 1170°C, and (D) annealed 30 min. at 1170°C.

Sample	Surface	Implanted Region	SiO_2 film	Si/SiO_2 Interface	Substrate
A	0.9172	-	0.9827	0.9718	1
B	0.9495	1.0244	0.8339	0.9794	1
C	0.9466	0.9954	0.9790	0.9578	1
D	0.9074	0.9581	0.9841	0.9538	1

A.1 Presence and Location of Silicon Nanocrystals

The results from the PAS model are important when discussing the presence and location of nanocrystals in the film because they can be directly compared with the TEM images. The presence of nanocrystals is evident by the S-parameter value in the implanted region dropping below that of SiO_2 after a 30 min anneal (sample D in Table A.1), and being comparable to the value at the Si/SiO_2 interface. Ghislotti *et al.* [52] observed similar results with the same conclusion that the reduction in S-parameter was due to the formation of Si-nc because they introduced several Si/SiO_2 interfaces effectively lowering the S-parameter value [102]. As well, the model thickness of the Si-nc region was 225 nm, which is comparable with the

observed TEM thickness of approximately 200 nm. Thus, the results from the PAS model and the TEM images are in mutual agreement regarding the presence and location of the nanocrystals.

Since the PAS model and TEM images agree on the presence and location of the nanocrystals, the positron diffusion length and the nearest neighbour distance of the Si-nc in the TEM images should be comparable. Positrons are attracted to the Si-nc interface which would be reflected in the diffusion coefficient and diffusion length. The positron diffusion coefficient in the implanted and annealed sample was 0.0020 cm^2/s, much shorter than the SiO_2 film diffusion coefficient of 0.0083 cm^2/s. This indicates that the positrons do not diffuse as far before they annihilate and the average distance they travel before annihilation can be determined by the diffusion length:

$$l = \sqrt{4Dt}$$

where D is the diffusion coefficient and t is time. The diffusion length is directly comparable to the nearest neighbour distance in the TEM images. The nearest neighbour distance can be calculated by using the Wigner-Seitz radius given by

$$d_{nn} = 2\left(\frac{3}{4\pi}\frac{V}{N}\right)^{\frac{1}{3}} - d$$

where V is volume of the sample in the TEM image, N is the average number of particles in the TEM image, and d is the average particle diameter. The diffusion length using a diffusion coefficient of 0.0020 cm^2/s is 8.9 nm and the approximate nearest neighbour distance from the TEM images was 6.6 nm. However, the diffusion coefficient is constrained by the boundary conditions mentioned earlier for SiO_2,

which does not include the existence of Si/SiO_2 interfaces in the oxide layer. If the diffusion coefficient is permitted to vary in order to achieve the best fit, then the diffusion coefficient would be 0.0010 cm^2/s or a diffusion length of 6.3 nm. This best fit diffusion length is very similar to the nearest neighbour distance in the TEM images further supporting the existence of silicon nanocrystals.

APPENDIX B

Quantum Mechanics Calculations

B.1 One-Dimensional Finite Square Well

The one-dimensional finite square well can be solved using Schrödinger's time-independent wave equation expressed as follows

$$-\frac{\hbar^2}{2m^*_{e,h}}\frac{d^2\psi}{dx^2}+V_{e,h}\psi=E_{e,h}\psi$$

where the potential energy of the system is given by

$$V_{e,h}(x)=\begin{cases}0, & \text{for } |x|<a\\ V_o, & \text{for } |x|>a\end{cases}$$

For the region *inside* the square well the potential energy is zero, which implies that the Schrödinger equation becomes

$$-\frac{\hbar^2}{2m^*_{e,h(in)}}\frac{d^2\psi}{dx^2}=E_{e,h}\psi, \qquad \text{or} \qquad \frac{d^2\psi}{dx^2}=-\kappa^2\psi,$$

where

$$\kappa\equiv\frac{\sqrt{2m^*_{e,h(in)}E_{e,h}}}{\hbar}$$

The general solution for the wavefunction *inside* the well is then given by

$$\psi_{e,h}(x)=A\cos(\kappa x)+B\sin(\kappa x)$$

where A and B are normalization constants.

For the region *outside* the square well the potential energy is V_o, which implies that the Schrödinger equation becomes

$$-\frac{\hbar^2}{2m^*_{e,h(out)}}\frac{d^2\psi}{dx^2}+V_o\psi=E_{e,h}\psi, \qquad \text{or} \qquad \frac{d^2\psi}{dx^2}=k^2\psi,$$

where

$$k\equiv\frac{\sqrt{2m^*_{e,h(out)}\left(V_o-E_{e,h}\right)}}{\hbar}$$

The general solution for the wavefunction *outside* the well is then given by

$$\psi_{e,h}\left(x\right)=C\exp\left(-kx\right)+D\exp\left(kx\right)$$

where C and D are normalization constants.

Grouping the general solutions together and separating them into even and odd solutions results in the following forms

$$\psi\left(x\right)=\begin{cases}A\cos\left(\kappa x\right), & \text{for } |x|<a \quad \text{even solution}\\ C\exp\left(-kx\right), & \text{for } |x|>a\end{cases} \tag{B.1}$$

$$\psi\left(x\right)=\begin{cases}B\sin\left(\kappa x\right), & \text{for } |x|<a \quad \text{odd solution}\\ C\exp\left(-kx\right), & \text{for } |x|>a\end{cases} \tag{B.2}$$

The general solutions inside and outside the well need to be continuous at the boundaries, which implies that ψ and $d\psi/dx$ at $|x|=a$ need to be continuous. The continuity of $\psi\left(x\right)$ for both the even and odd solutions at a are

$$\psi\left(x\right)=\begin{cases}A\cos\left(\kappa a\right)=C\exp\left(-ka\right), & \text{even solution}\\ B\sin\left(\kappa a\right)=C\exp\left(-ka\right), & \text{odd solution}\end{cases} \tag{B.3}$$

and the continuity of $d\psi/dx$ for both the even and odd solutions at a are

$$\frac{d\psi(x)}{dx} = \begin{cases} -\kappa A \sin(\kappa a) = -kC \exp(-ka), & \text{even solution} \\ \kappa B \cos(\kappa a) = -kC \exp(-ka), & \text{odd solution} \end{cases} \tag{B.4}$$

Dividing Eq. B.4 by Eq. B.3, we find that

$$\frac{k}{\kappa} = \begin{cases} \tan(\kappa a), & \text{even solution} \\ -\cot(\kappa a), & \text{odd solution} \end{cases} \tag{B.5}$$

The expressions obtained in Eq. B.5 are the allowed energy states of the system since κ and k are both a function of $E_{e,h}$. Expanding Eq. B.5 we get

$$\sqrt{\frac{m^*_{e,h(out)}(V_o - E_{e,h})}{m^*_{e,h(in)}E_{e,h}}} = \begin{cases} \tan(\kappa a) \\ -\cot(\kappa a) \end{cases}$$

$$\sqrt{\frac{m^*_{e,h(out)}V_o}{m^*_{e,h(in)}E_{e,h}} - \frac{m^*_{e,h(out)}}{m^*_{e,h(in)}}} = \begin{cases} \tan(\kappa a) \\ -\cot(\kappa a) \end{cases}$$

Adopting a nicer notation: let

$$z \equiv \kappa a, \qquad \text{and} \qquad z_o \equiv \frac{a}{\hbar}\sqrt{2m^*_{e,h(out)}V_o}$$

Therefore, Eq. B.5 becomes

$$\boxed{\sqrt{\left(\frac{z_o}{z}\right)^2 - \frac{m^*_{e,h(out)}}{m^*_{e,h(in)}}} = \begin{cases} \tan(z), & \text{even solution} \\ -\cot(z), & \text{odd solution} \end{cases}} \tag{B.6}$$

The above transcendental expressions differ slightly from those presented in quantum mechanics textbooks due to the variation in the effective masses inside and outside the one-dimensional finite square well.

B.2 Three-Dimensional Finite Spherical Well

The three-dimensional finite spherical well can be solved using Schrödinger's radial time-independent wave equation expressed as follows

$$-\frac{\hbar^2}{2m^*_{e,h}}\frac{d^2\psi}{dr^2}+\left[V_{e,h}+\frac{\hbar^2}{2m^*_{e,h}}\frac{\ell(\ell+1)}{r^2}\right]\psi=E_{e,h}\psi$$

where the potential energy of the system is given by

$$V_{e,h}(r)=\begin{cases}0, & \text{for } |r|<a\\ V_o, & \text{for } |r|>a\end{cases}$$

For the region *inside* the spherical well the potential energy is zero, which implies that the Schrödinger equation becomes

$$-\frac{\hbar^2}{2m^*_{e,h(in)}}\frac{d^2\psi}{dr^2}+\frac{\hbar^2}{2m^*_{e,h(in)}}\frac{\ell(\ell+1)}{r^2}\psi=E_{e,h}\psi,$$

or

$$\frac{d^2\psi}{dr^2}=\left[\frac{\hbar^2}{2m^*_{e,h(in)}}\frac{\ell(\ell+1)}{r^2}-\kappa^2\right]\psi,$$

where

$$\kappa\equiv\frac{\sqrt{2m^*_{e,h(in)}E_{e,h}}}{\hbar}$$

Solving for the zeroth order case ($\ell=0$), the general solution for the wavefunction *inside* the well is then expressed as

$$\psi_{e,h}(r)=n_o(\kappa r)+j_o(\kappa r)=-A\frac{\cos(\kappa r)}{\kappa r}+B\frac{\sin(\kappa r)}{\kappa r}$$

where $n_o(\kappa r)$ is the Neumann function of the zeroth order, $j_o(kr)$ is the Bessel function of the zeroth order, and A and B are normalization constants.

For the region *outside* the spherical well the potential energy is V_o, which implies that the Schrödinger equation becomes

$$-\frac{\hbar^2}{2m^*_{e,h(out)}}\frac{d^2\psi}{dr^2}+\left[V_o+\frac{\hbar^2}{2m^*_{e,h(out)}}\frac{\ell(\ell+1)}{r^2}\right]\psi=E_{e,h}\psi,$$

or

$$\frac{d^2\psi}{dr^2}=\left[\frac{\hbar^2}{2m^*_{e,h(out)}}\frac{\ell(\ell+1)}{r^2}+k^2\right]\psi,$$

where

$$k\equiv\frac{\sqrt{2m^*_{e,h(out)}\left(V_o-E_{e,h}\right)}}{\hbar}$$

Solving for the zeroth order case ($\ell=0$), the general solution for the wavefunction *outside* the well is then expressed as

$$\psi_{e,h}(r)=-C\frac{\exp(-kr)}{kr}+D\frac{\exp(kr)}{kr}$$

where C and D are normalization constants.

Grouping the general solutions together and separating them in terms of the Neumann function, $n_o(\kappa r)$, and the Bessel function, $j_o(kr)$, results in the following forms

$$\psi(r)=\begin{cases}-A\dfrac{\cos(\kappa r)}{\kappa r}, & \text{for } |r|<a \quad \text{Neumann function}\\[2ex] -C\dfrac{\exp(-kr)}{kr}, & \text{for } |r|>a\end{cases} \tag{B.7}$$

$$\psi(r) = \begin{cases} B\dfrac{\sin(\kappa r)}{\kappa r}, & \text{for } |r| < a \quad \text{Bessel function} \\ -C\dfrac{\exp(-kr)}{kr}, & \text{for } |r| > a \end{cases} \tag{B.8}$$

For the Neumann function the constant A has to be zero because of the singular behaviour as $r \to 0$. This leaves only the Bessel function solution, which has to be continuous at the boundaries, implying that ψ and $d\psi/dr$ are continuous at $|r| = a$. The continuity of $\psi(r)$ for the Bessel function solution at a is

$$B\frac{\sin(\kappa a)}{\kappa a} = -C\frac{\exp(-ka)}{ka} \tag{B.9}$$

and the continuity of $d\psi/dr$ at a is

$$\frac{\kappa B\cos(\kappa a)}{\kappa a} - \frac{B\sin(\kappa a)}{\kappa a^2} = \frac{kC\exp(-ka)}{ka} + \frac{C\exp(-ka)}{ka^2}$$

$$B\frac{\kappa a\cos(\kappa a) - \sin(\kappa a)}{\kappa a^2} = C\frac{ka\exp(-ka) + \exp(-ka)}{ka^2} \tag{B.10}$$

Dividing Eq. B.10 by Eq. B.9, we find that

$$\frac{\kappa a\cos(\kappa a) - \sin(\kappa a)}{\cancel{a}\sin(\kappa a)} = -\frac{(ka+1)}{\cancel{a}}$$

$$\kappa a\cot(\kappa a) - \cancel{1} = -ka - \cancel{1}$$

$$\frac{k}{\kappa} = -\cot(\kappa a) \tag{B.11}$$

Equation B.11 is exactly the same result as the odd function given in Eq. B.5, therefore the simplified version of the transcendental equation is

$$\boxed{\sqrt{\left(\frac{z_o}{z}\right)^2 - \frac{m^*_{e,h(out)}}{m^*_{e,h(in)}}} = -\cot(z)} \tag{B.12}$$

B.3 Results

Along with the individual excited states for the electrons and holes, the silicon band gap of 1.12 eV must also be included to obtain the emission energy of the silicon nanocrystal (Si-nc).

$$E = E_g + E_e + E_h \tag{B.13}$$

A few example results are given below in Table B.1 and shown in Figure B.1.

Table B.1: Results for the one-dimensional *even* solution and the three-dimensional solution (which is equivalent to the one-dimensional *odd* solution).

Si-nc Diameter (nm)	Solution (1D/3D)	E_e (eV)	E_h (eV)	E (eV)	Wavelength (nm)
0.5	1D	1.54	1.06	3.71	334
	3D	-	-	-	-
1	1D	0.65	0.40	2.17	571
	3D	2.30	1.61	5.03	246
1.5	1D	0.35	0.21	1.68	739
	3D	1.33	0.84	3.29	376
2	1D	0.21	0.13	1.46	848
	3D	0.84	0.52	2.48	501
3	1D	0.10	0.06	1.29	963
	3D	0.42	0.25	1.79	694
5	1D	0.04	0.02	1.18	1046
	3D	0.16	0.10	1.38	899

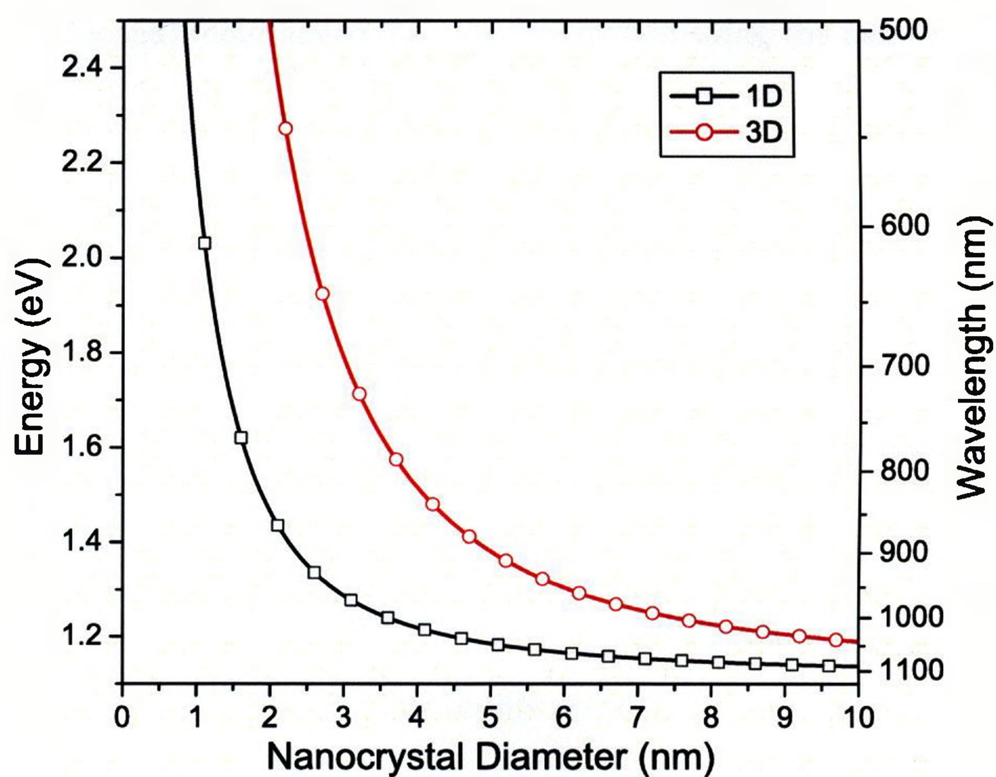

Figure B.1: The emission energy and wavelength of silicon nanocrystals for the one-dimensional *even* solution and the three-dimensional solution (or one-dimensional *odd* solution).

APPENDIX C

Photoluminescence Simulations

The simulated PL emission spectra and their equivalent TEM size distributions are further presented in this Appendix. The authors of the publications examined (Priolo and Iacona), determined the size distribution using the nanocrystal radius. Had they utilized the nanocrystal diameter they could have improved the Gaussian fit while maintaining the same number of significant digits and decimal places. For example, a mean radius of 2.1 nm is equivalent to a diameter of 4.2 ± 0.2 nm, whereas a measurement of the mean diameter would have been 4.2 ± 0.1 nm. As well, at the higher nanocrystal diameters the distribution deviates from a Gaussian distribution, which affects the simulated PL at higher wavelengths. Thus, the TEM size distributions were re-evaluated to obtain the best fit, and a comparison between the fits is shown in Figure C.1. The results are also summarized in Table C.1 and shown in Figure C.2. The difference in the results is noticeable both in the peak PL wavelength and the full width half maximum (FWHM), but more so in the FWHM compared with the results presented in Table 4.2. As well, one notices through inspection that the simulated PL in Figure C.2 appears to fit the experimental results better than those plotted in Figure 4.9. These results indicate the importance of the accuracy of the TEM distribution on the simulated PL.

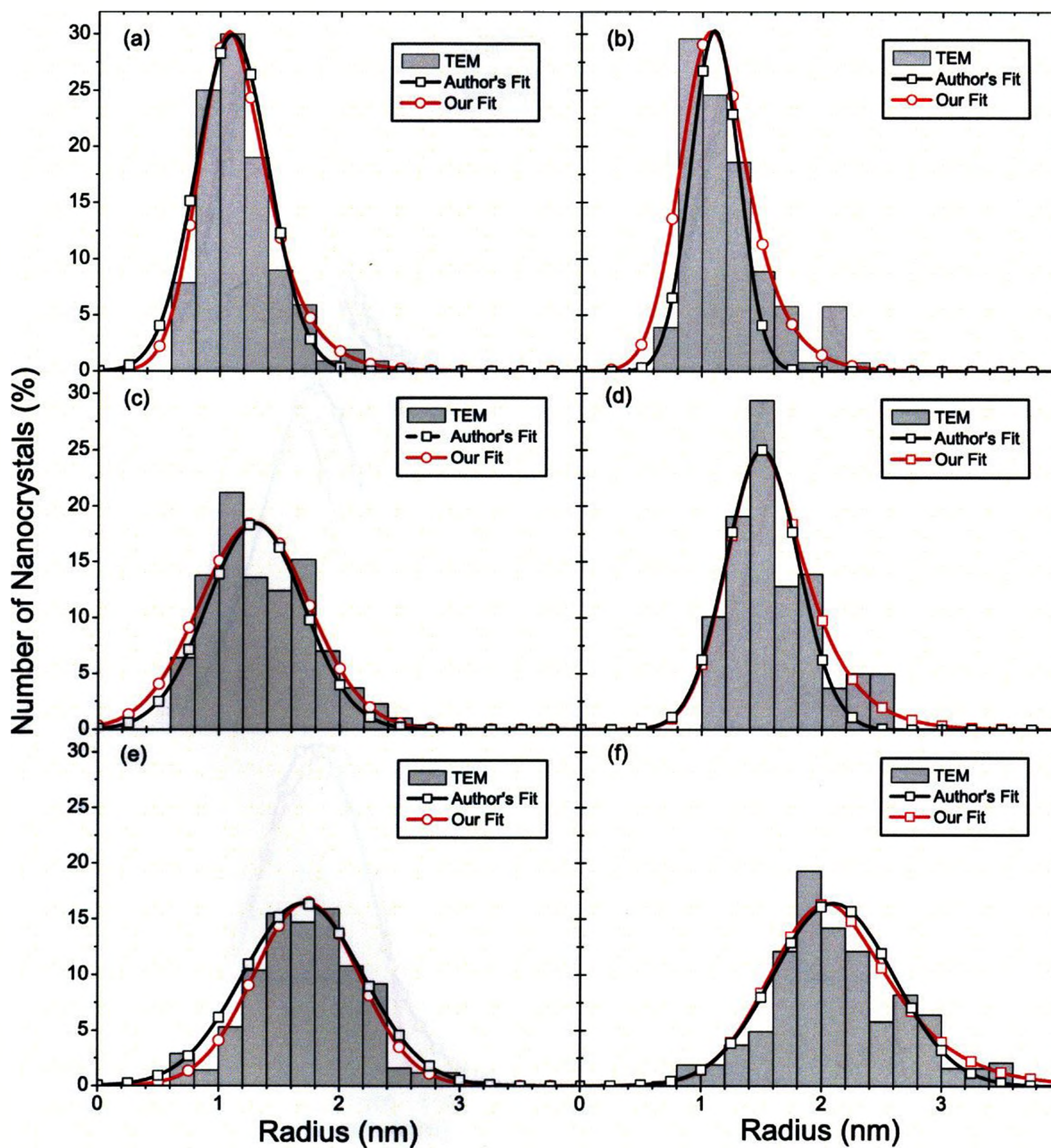

Figure C.1: The TEM distribution for (a) is from Priolo [64], and (b - f) are from Iacona [80]. Both the author's fits and our own are included in the TEM distributions. The TEM distributions refer to sample's $A2$ (a), $B2$ (b), $B3$ (c), $B4$ (d), $B5$ (e), and $B6$ (f) from Table C.1.

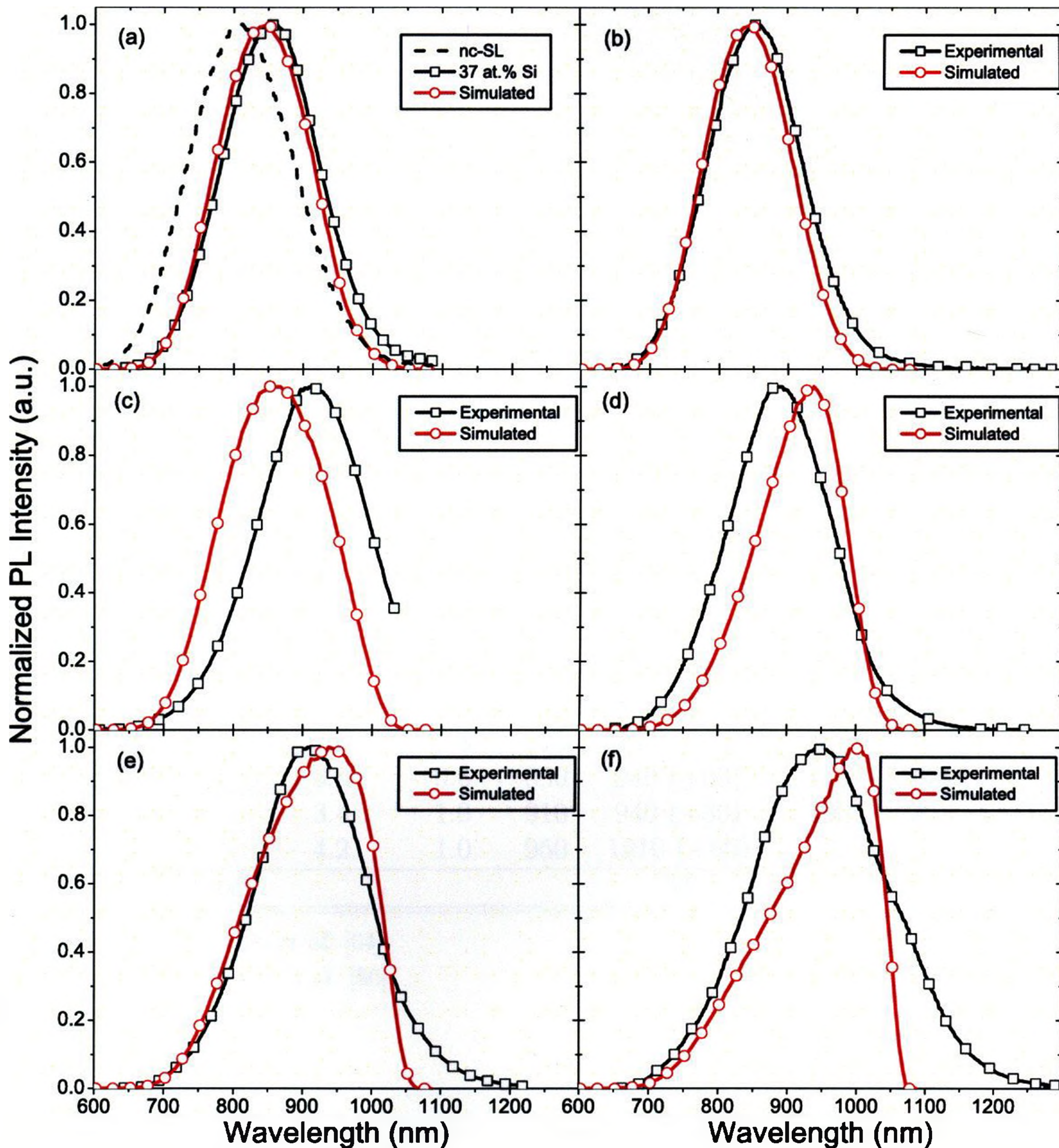

Figure C.2: The simulated PL intensities are from our own fits' of the TEM size distributions and not those stated in References [64, 80]. The simulated PL emissions are from Table C.1 sample's $A2$ (a), $B2$ (b), $B3$ (c), $B4$ (d), $B5$ (e), and $B6$ (f). The experimental PL for (a - b), and (d - f) are from Priolo [64], and (c) is from Iacona [80].

Table C.1: Summary of the experimental and simulated PL utilizing our own fit of the TEM distributions. The values in brackets of the "simulated" columns represent the difference between the experimental and simulated results.

Sample	Mean Diameter (nm)	σ (nm)	λ_{max} (nm)	λ_{max} Simulated (nm)	FWHM (nm)	FWHM Simulated (nm)
A1-SL	2.2	0.8	810	840 (+30)	175	175 (0)
A2	2.2	0.6	860	850 (−10)	165	165 (0)
B1	2.0	0.4	900	840 (−60)	–	130 (–)
B2	2.2	0.4	850	850 (0)	160	150 (−10)
B3	2.6	0.8	915	855 (−60)	185	190 (+ 5)
B4	3.0	0.6	890	940 (+50)	175	145 (−30)
B5	3.4	1.0	910	940 (+30)	190	205 (+15)
B6	4.2	1.0	950	1010 (+60)	230	175 (−55)
Mean Difference				38		16

Samples A - Priolo *et al.* [64]
Samples B - Iacona *et al.* [80]

APPENDIX D

Coulomb Interaction

There are several additional terms that can be included in the Hamiltonian utilized to determine the emission energy of the silicon nanocrystals. Among these terms are the Coulomb interaction, exchange interaction, electron-hole correlation, polarization at the surface, etc [31]. Most of these terms are very small with the exception of the Coulomb interaction. Generally, the Coulomb interaction is ignored in a strong confinement regime but included in other regimes, effectively lowering the emission energy. Thus, the Coulomb interaction will be the only additional term in the Hamiltonian that will be reviewed in detail.

The emission energy of the Si-nc was calculated using both the finite square well and finite spherical well models. The wavefunctions in the two models are either one-dimensional or three-dimensional in nature and require an equivalent Coulomb interaction. In both cases the Coulomb interaction is treated as a perturbation [103, 104], and the emission energy becomes

$$E = E_g + E_e + E_h + \langle \Psi | H_{eh} | \Psi \rangle \tag{D.1}$$

where E_g is the band gap of silicon, E_e is the energy of the excited electron, E_h is the energy of the excited hole, and H_{eh} is the exciton Hamiltonian.

D.1 Coulomb Interaction for a Finite Square Well

In a finite square well the Coulomb interaction Hamiltonian has the form [104, 105]

$$H_{eh}^{1D} = -\frac{\hbar^2}{2\mu}\nabla^2 - \frac{e^2}{4\pi\epsilon\sqrt{r^2 + (x_e - x_h)^2}} \tag{D.2}$$

where μ is the exciton effective mass, ϵ is the dielectric constant, which is generally different from the bulk dielectric constant, and r and x_i are the positions of the electrons and holes. The exciton effective mass can be determined from the following expression

$$\mu = \left(\frac{1}{m_e} + \frac{1}{m_h}\right)^{-1}$$

where m_e and m_h are the effective masses of the electron and hole respectively. The dielectric constant inside the nanocrystal is determined from a generalization of Penn's model [106, 107]

$$\epsilon_s(R) = 1 + \frac{\epsilon_b - 1}{1 + \left(\frac{\alpha}{R}\right)^l} \tag{D.3}$$

where R is the radius, ϵ_b is the bulk dielectric constant (11.9), $\alpha = 6.9$ Å[108], and $l = 1.37$ [108]. The wavefunction for the exciton in a finite square well is a product ansatz expressed as

$$\Psi^{1D} = \psi_e(x_e)\psi_h(x_h)\Psi_{eh}(r) \tag{D.4}$$

where ψ_e and ψ_h are the one-dimensional non-interacting electron (e) and hole (h) wavefunctions, and $\Psi_{eh}(r)$ is the electron-hole Coulomb interaction wavefunction. The non-interacting electron and hole wavefunctions in one-dimension had an *even* and *odd* solution given earlier in Eq. B.6. However, it is easier to evaluate the

Coulomb interaction by solving the infinite square well with an effective well width. The energy of the *even* solution and infinite square well with an effective well width renders the same excited energy results but is slightly easier to evaluate. The infinite square well wavefunction using the effective width is expressed as

$$\psi_j(x) = \sqrt{\frac{2}{L_j}} \cos\left(\frac{\pi x_j}{L_j}\right) \tag{D.5}$$

where L_j is the effective width.

For the electron-hole Coulomb interaction wavefunction (Ψ_{eh}), the 1s-like function is assumed [104, 105, 109].

$$\Psi_{1,eh}(r) = N_1 \exp\left(-\frac{r}{\lambda}\right) \tag{D.6}$$

$$\Psi_{2,eh}(r) = N_2 \exp\left(-\frac{\sqrt{r^2 + (x_e - x_h)^2}}{\lambda}\right) \tag{D.7}$$

where λ is the radius determined variationally, and N_1 and N_2 are the normalization constants. The first expression for the Coulomb interaction wavefunction can accurately account for the behaviour of the exciton in narrow square wells but fails to approximate the behaviour in wider square wells [105, 109]. The second expression approximates the behaviour of the exciton in both narrow and wide wells but it is more complicated to solve [105, 109].

First, the wavefunctions need to be normalized. The normalization constant for Eq. D.6 is given by $N_1 = \sqrt{\frac{2}{\pi\lambda^2}}$ [104, 105, 110], and Eq. D.7 normalized becomes

$$1 = |N_2|^2 \int_0^{2\pi} d\varphi \int_0^{\infty} r \exp\left(-\frac{2\sqrt{r^2 + (x_e - z_h)^2}}{\lambda}\right) dr \tag{D.8}$$

Adopting a nicer notation: Let

$$u = \sqrt{r^2 + (x_e - x_h)^2}$$

$$du = \frac{1}{2} 2r \left[r^2 + (x_e - x_h)^2\right]^{-1/2}$$

$$udu = rdr$$

Substituting u into the normalization expression results into Eq. D.8

$$1 = 2\pi |N_2|^2 \int_{|x_e - x_h|}^{\infty} u \exp\left(-\frac{2u}{\lambda}\right) du \tag{D.9}$$

$$1 = 2\pi |N_2|^2 \left[-\frac{1}{4}\lambda (2u + \lambda) \exp\left(-\frac{2u}{\lambda}\right)\right]_{|x_e - x_h|}^{\infty} \tag{D.10}$$

$$1 = |N_2|^2 \frac{\pi}{2}\lambda (2|x_e - x_h| + \lambda) \exp\left(-\frac{2|x_e - x_h|}{\lambda}\right) \tag{D.11}$$

Thus, the normalization constant for the second trial wavefunction is

$$\boxed{N_2 = \left[\frac{2\exp\left(\frac{2|x_e - x_h|}{\lambda}\right)}{\pi\lambda (2|x_e - x_h| + \lambda)}\right]^{1/2}} \tag{D.12}$$

Now, the Coulomb interaction of the two different trial wavefunctions can be determined. First, the simple trial wavefunction (Eq. D.6) will be evaluated. Since the simple trial wavefunction is separable the kinetic energy term only needs to be evaluated for the electron-hole Coulomb interaction wavefunction (Ψ_{eh}):

$$\langle T_1 \rangle = \left\langle \Psi_{1,eh}(r) \left| -\frac{\hbar^2}{2\mu}\nabla^2 \right| \Psi_{1,eh}(r) \right\rangle$$

$$\langle T_1 \rangle = -\frac{\hbar^2}{2\mu} |N_1|^2 \int_0^{2\pi} d\varphi \int_0^{\infty} r \exp\left(-\frac{r}{\lambda}\right) \nabla^2 \exp\left(-\frac{r}{\lambda}\right) dr$$

$$\langle T_1 \rangle = -\frac{\hbar^2\pi}{\mu} |N_1|^2 \int_0^{\infty} r \exp\left(-\frac{r}{\lambda}\right) \frac{1}{r}\frac{d}{dr} r \frac{d}{dr} \exp\left(-\frac{r}{\lambda}\right) dr$$

$$\langle T_1 \rangle = -\frac{\hbar^2\pi}{\mu} |N_1|^2 \int_0^{\infty} \left(\frac{r}{\lambda^2} - \frac{1}{\lambda}\right) \exp\left(-\frac{2r}{\lambda}\right) dr$$

$$\langle T_1 \rangle = -\frac{\hbar^2 \pi}{\mu} |N_1|^2 \left\{ \left[-\frac{\lambda^2}{4\lambda^2} - \frac{2r\lambda^2}{4\lambda^3} + \frac{1}{2} \right] \exp\left(-\frac{2r}{\lambda}\right) \right\}_0^\infty$$

$$\langle T_1 \rangle = -\frac{\hbar^2 \pi}{\mu} |N_1|^2 \left(\frac{1}{4} - \frac{1}{2}\right)$$

Thus, the kinetic energy term is

$$\boxed{\langle T_1 \rangle = \frac{\hbar^2}{2\mu\lambda^2}} \tag{D.13}$$

The potential energy for the simple trial wavefunction was evaluated both analytically and numerically as follows

$$\langle V_1 \rangle = \left\langle \Psi^{1D} \left| -\frac{e^2}{4\pi\epsilon} \frac{1}{\sqrt{r^2 + (x_e - x_h)^2}} \right| \Psi^{1D} \right\rangle$$

$$\langle V_1 \rangle = -\frac{e^2}{4\pi\epsilon} |A_e|^2 |A_h|^2 |N_1|^2 \int_{-a_e}^{a_e} \cos^2\left(\frac{\pi x_e}{L_e}\right) dx_e \int_{-a_h}^{a_h} \cos^2\left(\frac{\pi x_h}{L_h}\right) dx_h$$

$$\times \int_0^{2\pi} d\varphi \int_0^\infty \frac{r \exp\left(-\frac{r}{\lambda}\right)}{\sqrt{r^2 + (x_e - x_h)^2}} dr$$

Thus, the potential energy term is

$$\boxed{\begin{aligned} \langle V_1 \rangle = &-\frac{2e^2}{\pi\epsilon\lambda L_e L_h} \int_{-a_e}^{a_e} \cos^2\left(\frac{\pi x_e}{L_e}\right) dx_e \int_{-a_h}^{a_h} \cos^2\left(\frac{\pi x_h}{L_h}\right) dx_h \\ &\times \frac{2|x_e - x_h|}{\lambda} \left\{ \frac{\pi}{2} \left[H_1\left(\frac{2|x_e - x_h|}{\lambda}\right) - N_1\left(\frac{2|x_e - x_h|}{\lambda}\right) \right] - 1 \right\} \end{aligned}} \tag{D.14}$$

where H_1 is the first-order Struve function and N_1 is the first-order Neumann function or Bessel function of the second kind. Evaluating Eq. D.14 further analytically is very difficult and it was evaluated instead numerically. Both expressions for the kinetic and potential energy perturbations are the same as those presented in other publications [104, 105, 109, 110]

The second trial wavefunction is a little more complicated but can predict the Coulomb interaction for larger nanocrystals more accurately. The second trial

wavefunction is not separable, implying that the kinetic energy term needs to be evaluated for the entire product ansatz wavefunction (Ψ^{1D}) given by

$$\langle T_2\rangle = \left\langle \Psi^{1D} \left| -\frac{\hbar^2}{2\mu}\nabla^2 \right| \Psi^{1D} \right\rangle$$

$$\langle T_2\rangle = -\frac{\hbar^2}{2\mu} |A_e|^2 |A_h|^2 |N_2|^2 \int_{-a_e}^{a_e} \cos^2\left(\frac{\pi x_e}{L_e}\right) dx_e \int_{-a_h}^{a_h} \cos^2\left(\frac{\pi x_h}{L_h}\right) dx_h$$

$$\times \int_0^{2\pi} d\varphi \int_0^{\infty} r \exp\left(-\frac{\sqrt{r^2+(x_e-x_h)^2}}{\lambda}\right) \nabla^2 \exp\left(-\frac{\sqrt{r^2+(x_e-x_h)^2}}{\lambda}\right) dr$$

$$\langle T_2\rangle = -\frac{\hbar^2\pi}{\mu} |A_e|^2 |A_h|^2 |N_2|^2 \int_{-a_e}^{a_e} \cos^2\left(\frac{\pi x_e}{L_e}\right) dx_e \int_{-a_h}^{a_h} \cos^2\left(\frac{\pi x_h}{L_h}\right) dx_h$$

$$\underbrace{\times \int_0^{\infty} r \exp\left(-\frac{\sqrt{r^2+(x_e-x_h)^2}}{\lambda}\right) \frac{1}{r}\frac{d}{dr} r \frac{d}{dr} \exp\left(-\frac{\sqrt{r^2+(x_e-x_h)^2}}{\lambda}\right) dr}_{\blacktriangle}$$

$$\blacktriangle = |N_2|^2 \int_0^{\infty} r \exp\left(-\frac{\sqrt{r^2+(x_e-x_h)^2}}{\lambda}\right)$$

$$\times \frac{1}{r}\frac{d}{dr} \frac{r^2\left(r^2+|x_e-x_h|^2\right)^{-1/2}}{\lambda} \exp\left(-\frac{\sqrt{r^2+(x_e-x_h)^2}}{\lambda}\right) dr$$

$$\blacktriangle = |N_2|^2 \int_0^{\infty} r \left\{ \frac{r^2\left[r^2+(x_e-x_h)^2\right]^{-3/2}}{\lambda} + \frac{r^2\left[r^2+(x_e-x_h]^2\right)^{-1}}{\lambda^2} \right.$$

$$\left. - \frac{2\left[r^2+(x_e-x_h)^2\right]^{-1/2}}{\lambda} \right\} \exp\left(-\frac{2\sqrt{r^2+(x_e-x_h)^2}}{\lambda}\right) dr$$

Once again let

$$u = \sqrt{r^2+(x_e-x_h)^2}$$

$$udu = rdr$$

$$\blacktriangle = |N_2|^2 \int_{|x_e-x_h|}^{\infty} u \left\{ \frac{u^2-(x_e-x_h)^2}{u^3\lambda} + \frac{u^2-(x_e-x_h)^2}{u^2\lambda^2} - \frac{2}{u\lambda} \right\} \exp\left(-\frac{2u}{\lambda}\right) du$$

$$\blacktriangle = |N_2|^2 \int_{|x_e-x_h|}^{\infty} \left\{ \frac{u}{\lambda^2} - \frac{(x_e-x_h)^2}{u^2\lambda} - \frac{(x_e-x_h)^2}{u\lambda^2} - \frac{1}{\lambda} \right\} \exp\left(-\frac{2u}{\lambda}\right) du$$

$$\blacktriangle = |N_2|^2 \left\{ \left[\frac{1}{2} - \frac{1}{4} + \frac{(x_e-x_h)^2}{u\lambda} - \frac{u}{2\lambda} \right] \exp\left(-\frac{2u}{\lambda}\right) - \frac{(x_e-x_h)^2}{\lambda^2} E_1\left(\frac{2u}{\lambda}\right) \right\}_{|x_e-x_h|}^{\infty}$$

$$\blacktriangle = |N_2|^2 \left[-\frac{\lambda + 2|x_e-x_h|}{4\lambda} \exp\left(-\frac{2|x_e-x_h|}{\lambda}\right) + \frac{(x_e-x_h)^2}{\lambda^2} E_1\left(\frac{2|x_e-x_h|}{\lambda}\right) \right]$$

$$\blacktriangle = -\frac{1}{2\pi\lambda^2} + \frac{2(x_e-x_h)^2}{\pi\lambda^3\left[2(x_e-x_h)^2+\lambda\right]} \exp\left(\frac{2|x_e-x_h|}{\lambda}\right) E_1\left(\frac{2|x_e-x_h|}{\lambda}\right)$$

where E_1 is the exponential integral. Thus, the kinetic energy term can be evaluated numerically from the following expression

$$\boxed{\begin{aligned} \langle T_2 \rangle = & \frac{\hbar^2}{2\mu\lambda^2} \\ & - \frac{8\hbar^2}{\mu\lambda^3 L_e L_h} \int_{-a_e}^{a_e} \cos^2\left(\frac{\pi x_e}{L_e}\right) dx_e \int_{-a_h}^{a_h} \cos^2\left(\frac{\pi x_h}{L_h}\right) \\ & \times \frac{(x_e-x_h)^2}{2|x_e-x_h|+\lambda} \exp\left(\frac{2|x_e-x_h|}{\lambda}\right) E_1\left(\frac{2|x_e-x_h|}{\lambda}\right) dx_h \end{aligned}} \tag{D.15}$$

where a_e and a_h are the effective well radii for the electron and hole respectively. In the above kinetic energy expression, the first term is the same as that of the kinetic energy in Eq. D.13. The second term is smaller than the first term leading to a slight difference in the kinetic energies of both trial wavefunctions.

The potential energy term of the Hamiltonian for the second trial wavefunctions is evaluated both analytically and numerically as before. As well, the same substitution $u = \sqrt{r^2 + (x_e - x_h)^2}$ is utilized as shown in previous calculations.

$$\langle V_2 \rangle = \left\langle \Psi^{1D} \left| -\frac{e^2}{4\pi\epsilon} \frac{1}{\sqrt{r^2+(x_e-x_h)^2}} \right| \Psi^{1D} \right\rangle$$

$$\langle V_2 \rangle = -\frac{e^2}{4\pi\epsilon} |A_e|^2 |A_h|^2 |N_2|^2 \int_{-a_e}^{a_e} \cos^2\left(\frac{\pi x_e}{L_e}\right) dx_e \int_{-a_h}^{a_h} \cos^2\left(\frac{\pi x_h}{L_h}\right) dx_h$$

$$\times \int_0^{2\pi} d\varphi \int_{|x_e - x_h|}^{\infty} \frac{u \exp\left(-\frac{2u}{\lambda}\right)}{u} du$$

$$\langle V_2 \rangle = -\frac{e^2}{2\epsilon} |A_e|^2 |A_h|^2 |N_2|^2 \int_{-a_e}^{a_e} \cos^2\left(\frac{\pi x_e}{L_e}\right) dx_e \int_{-a_h}^{a_h} \cos^2\left(\frac{\pi x_h}{L_h}\right) dx_h$$

$$\times \left[-\frac{\lambda}{2} \exp\left(-\frac{2u}{\lambda}\right)\right]_{|x_e - x_h|}^{\infty}$$

Thus, the potential energy term is

$$\boxed{\langle V_2 \rangle = -\frac{2e^2}{\pi \epsilon L_e L_h} \int_{-a_e}^{a_e} \cos^2\left(\frac{\pi x_e}{L_e}\right) dx_e \int_{-a_h}^{a_h} \frac{\cos^2\left(\frac{\pi x_h}{L_h}\right)}{2|x_e - x_h| + \lambda} dx_h} \tag{D.16}$$

The perturbation expressions for the kinetic and potential energies of the two trial wavefunctions are the first step in determining the Coulomb interaction energy. With a variational parameter, the kinetic and potential energy perturbations need to be evaluated until a minimum in the Coulomb interaction is reached.

$$\left\langle \Psi^{1D} \left| H_{eh} \right| \Psi^{1D} \right\rangle_{min} = \langle T_i \rangle + \langle V_i \rangle$$

Since the expressions are not analytic, the minimization of the Coulomb interactions is determined numerically. A comparison of the Coulomb interaction energy for the two trial wavefunctions is shown in Table D.1 and Figure D.1. The results are very similar even for large nanocrystal sizes, but the relative difference as a percentage increases with nanocrystal diameter as discussed earlier.

Table D.1: Comparison of the Coulomb interaction energy determined utilizing the two trial wavefunctions.

Diameter (nm)	Wavefunction #1 E_{Coul}^{1D} (meV)	Wavefunction #2 E_{Coul}^{1D} (meV)
1.00	210	220
1.50	124	130
1.78	102	107
2.08	86	91
2.70	67	71
4.00	48	51
5.00	41	44
6.00	36	39

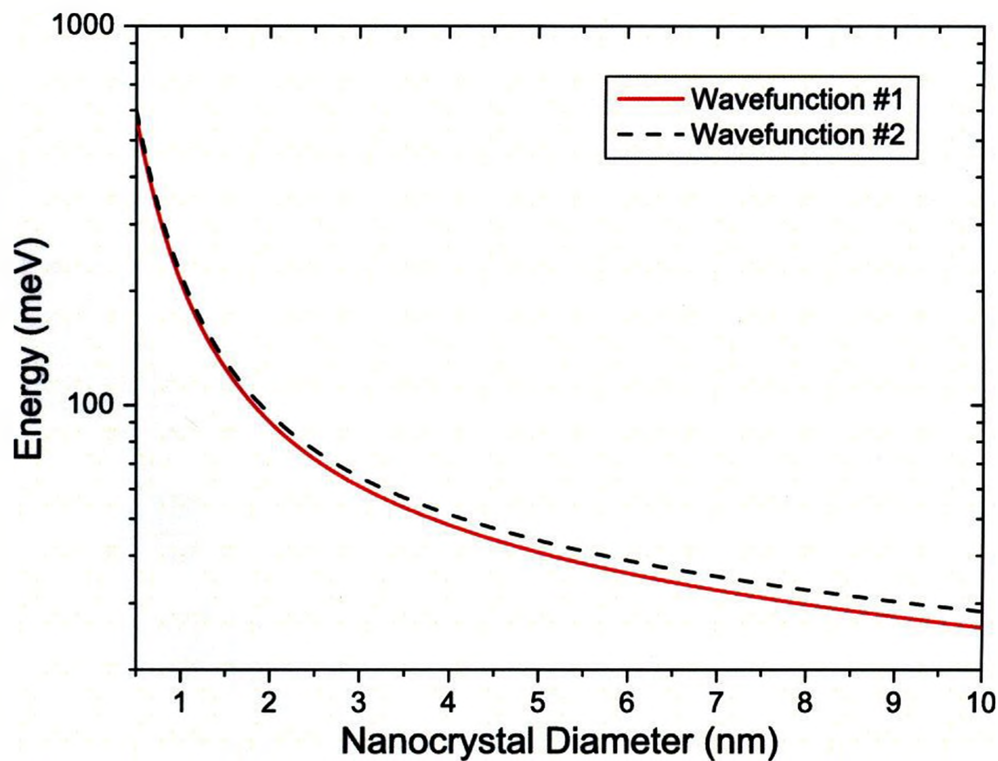

Figure D.1: Comparison of the Coulomb interaction energy evaluated utilizing the two trial wavefunctions.

D.2 Coulomb Interaction for a Finite Spherical Well

The Coulomb interaction Hamiltonian in a three-dimensional finite spherical well has the form [103].

$$H_{eh}^{3D} = -\frac{e^2}{4\pi\epsilon\left|\mathbf{r}_h - \mathbf{r}_e\right|}$$

where $\mathbf{r}_h$ and $\mathbf{r}_e$ are the position of the hole (h) and electron (e), and $|\mathbf{r}_h - \mathbf{r}_e| = \sqrt{r_h^2 + r_e^2 - 2r_h r_e \cos\theta_e}$. The wavefunction for the exciton in a finite spherical well is once again a product ansatz expressed as

$$\Psi^{3D} = \psi_e(\mathbf{r}_e)\psi_h(\mathbf{r}_h) \tag{D.17}$$

where ψ_e and ψ_h are the three-dimensional non-interacting electron (e) and hole (h) wavefunctions. Since the above Coulomb interaction is for a three-dimensional object, the three-dimensional Bessel function (Eq. 4.6) will be utilized and compared with other published results in literature. Prior to the calculation of the Coulomb interaction, the wavefunction needs to be normalized.

$$1 = \int |\psi(r)|^2 \, d^3\mathbf{r} = \int |\psi(r)|^2 \, r^2 dr \int_0^{\pi} \sin\theta d\theta \int_0^{2\pi} d\varphi$$

$$1 = 4\pi \left[\frac{|B|^2}{\kappa^2} \int_0^a \sin^2(\kappa r) dr + \frac{|C|^2}{k^2} \int_a^{\infty} \exp(-2kr) dr \right]$$

$$1 = 4\pi \left\{ \frac{|B|^2}{\kappa^2} \left[\frac{r}{2} - \frac{2\sin(\kappa r)\cos(\kappa r)}{4\kappa} \right]_0^a + \frac{|C|^2}{k^2} \left[-\frac{\exp(-2kr)}{2k} \right]_a^{\infty} \right\}$$

$$1 = 4\pi \left\{ \frac{|C|^2}{\kappa^2} \left[\frac{a}{2} - \frac{2\sin(\kappa a)\cos(\kappa a)}{4\kappa} \right] + \frac{|C|^2}{k^2} \left[-\frac{\exp(-2ka)}{2k} \right] \right\}$$

Substituting from the boundary condition $C = -Bk\sin(\kappa a)\exp(ka)/\kappa$ (Eq. B.9), and $k = \kappa\cot(\kappa a)$ (Eq. B.11) into the above expression leads to

$$1 = 4\pi |B|^2 \left[\frac{a}{2\kappa^2} - \frac{2\sin(\kappa a)\cos(\kappa a)}{4\kappa^3} - \frac{\sin^2(\kappa a)}{2\kappa^3\cot(\kappa a)} \right]$$

$$1 = 4\pi |B|^2 \left[\frac{a}{2\kappa^2} - \frac{2\sin(\kappa a)\cos(\kappa a)}{4\kappa^3} - \frac{\sin^3(\kappa a)}{2\kappa^3 \cos(\kappa a)} \right]$$

$$1 = 4\pi |B|^2 \left\{ \frac{a}{2\kappa^2} - \frac{2\sin(\kappa a)}{4\kappa^3 \cos(\kappa a)} \left[\cos^2(\kappa a) + \sin^2(\kappa a) \right] \right\}$$

$$1 = 4\pi |B|^2 \left\{ \frac{a}{2\kappa^2} - \frac{1}{2\kappa^2 k} \right\}$$

$$|B|^2 = \frac{2\kappa^2 k}{4\pi(ka+1)}$$

Thus, the normalization constants are:

$$\boxed{B = \frac{\kappa}{\sqrt{2\pi(a+1/k)}}} \quad \text{and} \quad \boxed{C = \frac{-k\sin(\kappa a)\exp(ka)}{\sqrt{2\pi(a+1/k)}}} \tag{D.18}$$

Next the Coulomb interaction energy is examined assuming that the exciton recombines inside the well, so

$$E^{3D}_{Coul} = \frac{e^2}{4\pi\epsilon} \iint \frac{|\psi_h(\mathbf{r}_h)|^2 |\psi_e(\mathbf{r}_e)|^2}{|\mathbf{r}_h - \mathbf{r}_e|} d^3r_h d^3r_e$$

$$E^{3D}_{Coul} = \frac{e^2}{4\pi\epsilon} \left[\frac{|B_h|^2}{\kappa_h^2} \int_0^a \frac{\sin^2(\kappa_h r_h)}{r_h^2} r_h^2 dr_h \int_0^\pi \sin\theta_h d\theta_h \int_0^{2\pi} d\varphi_h \right.$$

$$\left. \times \frac{|B_e|^2}{\kappa_h^2} \int_0^a \frac{\sin^2(\kappa_e r_e)}{r_e^2} r_e^2 dr_e \int_0^\pi \frac{\sin\theta_e}{\sqrt{r_h^2 + r_e^2 - 2r_e r_h \cos\theta_e}} d\theta_e \int_0^{2\pi} d\varphi_e \right]$$

$$E^{3D}_{Coul} = \frac{e^2}{4\pi\epsilon} \left[4\pi \frac{|B_h|^2}{\kappa_h^2} \int_0^a \sin^2(\kappa_h r_h) dr_h \right.$$

$$\left. \times 2\pi \frac{|B_e|^2}{\kappa_h^2} \int_0^a \sin^2(\kappa_e r_e) dr_e \underbrace{\left(\frac{1}{r_h r_e} \sqrt{r_h^2 + r_e^2 - 2r_e r_h \cos\theta_e} \right)_0^\pi}_{\blacklozenge} \right]$$

where

$$\blacklozenge = \frac{1}{r_h r_e} \left(\sqrt{r_h^2 + r_e^2 + 2r_e r_h} - \sqrt{r_h^2 + r_e^2 - 2r_e r_h} \right)$$

$$\blacklozenge = \frac{1}{r_h r_e} \left[(r_h + r_e) - |r_h - r_e| \right]$$

$$\blacklozenge = \begin{cases} 2/r_h, & \text{if } r_e < r_h \\ 2/r_e, & \text{if } r_e > r_h \end{cases}$$

and hence

$$\boxed{E^{3D}_{Coul} = \frac{4\pi e^2 \left|B_h\right|^2 \left|B_e\right|^2}{\epsilon \kappa_h^2 \kappa_e^2} \int_0^a \sin^2(\kappa_h r_h) dr_h \left[\int_0^{r_h} \frac{\sin^2(\kappa_e r_e)}{r_h} dr_e + \int_{r_h}^a \frac{\sin^2(\kappa_e r_e)}{r_e} dr_e \right]} \tag{D.19}$$

D.2.1 Comparison of Three-Dimensional Coulomb Interaction Results

Most often the emission energy for nanocrystals or quantum dots is solved utilizing the effective mass approximation (EMA) assuming infinite potential barriers. The ground state electron and hole wavefunctions for the EMA model are $(2\pi R)^{-1/2} \sin(\pi r/R) r^{-1}$, and the Coulomb energy perturbatively calculated from Eq. D.19 gives the well known analytic expression [111, 112]

$$E^{EMA}_{Coul} = 1.786 \frac{e^2}{4\pi\epsilon R} \tag{D.20}$$

Unfortunately, the EMA model can significantly overestimate the Coulomb Energy [103], mainly due to the wavefunction unrealistically vanishing at the nanocrystal boundary. Thus, an effective radius is required to achieve a more realistic solution for the Coulomb interaction.

The effective radius can be approximated by

$$R_{eff} = R + 2/k \tag{D.21}$$

with

$$k = \frac{\sqrt{2m^*_{out}(V_o - E)}}{\hbar}$$

Table D.2: Comparison of the Coulomb interaction energies determined through effective mass approximation (EMA), pseudopotentials (PS) [103], as a perturbation using Eq. D.19 (3D), and effective mass approximation utilizing the effective well width (EMA*).

Diameter (nm)	Effective Diameter (nm)	E_{Coul}^{EMA} (meV)	E_{Coul}^{PS} (meV)	E_{Coul}^{3D} (meV)	E_{Coul}^{EMA*} (meV)
1.00	1.94	976	-	509	503
1.50	2.10	507	340	375	363
1.78	2.32	391	270	311	299
2.08	2.59	311	223	259	250
2.70	3.18	217	176	190	184
4.00	4.46	131	-	120	117
6.00	6.44	81	-	76	75

where V_o is the average potential barrier height for the electron and hole (3.95 eV), E is the energy of the exciton solved from the transcendental Eq. B.12, and m_{out}^* is the exciton reduced mass outside the well given by

$$m_{out}^* = \left(\frac{1}{m_{e(out)}^*} + \frac{1}{m_{h(out)}^*} \right)^{-1}$$

Substituting the effective well width into Eq. D.20 rendered very similar results to those calculated in Eq. D.19. The slight difference between the two calculations occurred because Eq. D.21 slightly overestimates the well width, resulting in a slightly lower Coulomb interaction. All of the Coulomb interaction energies are summarized in Table D.2 and plotted in Figure D.2. The results of all the methods are very similar with the exception at small nanocrystal diameters for the EMA calculation without the effective well width, but this is to be expected with the unrealistic boundary conditions.

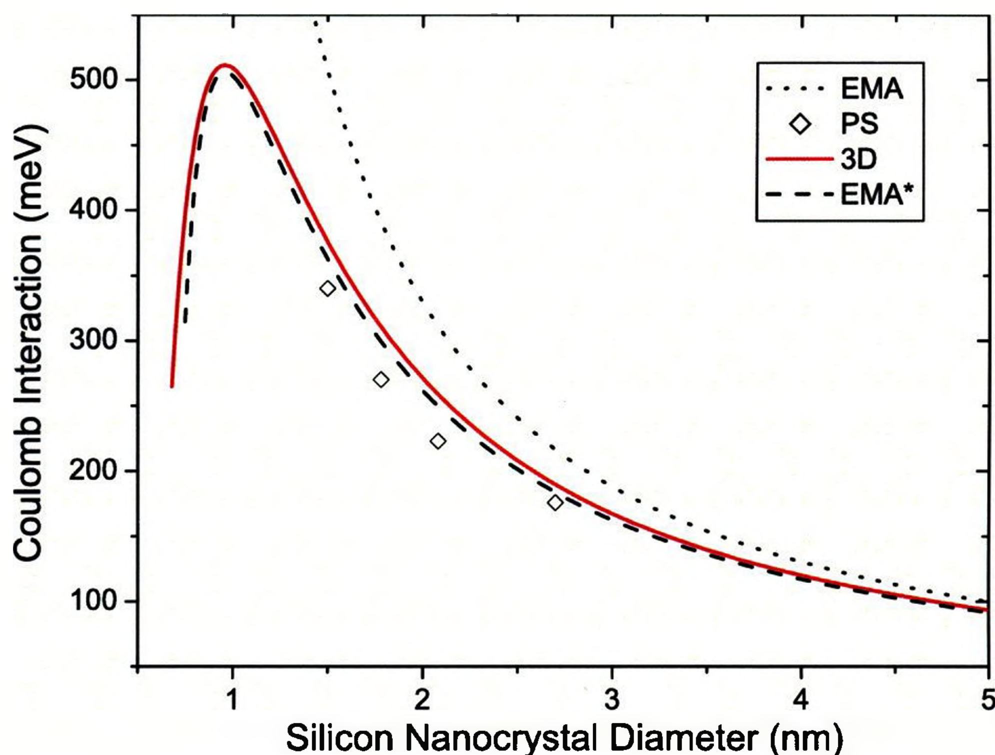

Figure D.2: Plot comparing the Coulomb interaction results from the effective mass approximation (EMA), pseudopotentials (PS) [103], as a perturbation (3D), and effective mass approximation utilizing the effective well width (EMA*).

D.3 Coulomb Interaction and Photoluminescence

The inclusion of the Coulomb interaction in both models should and did improve on the results stated in Chapter 4. In the case of the three-dimensional model, the results did not fit the experimental data well enough to warrant its application to the TEM measured nanocrystal size distribution. In Figure D.3, the emission energy including the Coulomb interaction for the three-dimensional model indicates that a nanocrystal approximately 3.4 nm in diameter emits at a wavelength of approximately 826 nm (the peak emission wavelength experimentally measured). From the 462 nanocrystals measured in the TEM micrographs, only one nanocrystal was 3.4 nm or greater in diameter. It seems highly unlikely that so few nanocrystals that emit at the peak PL wavelength or greater wavelengths, would result in such

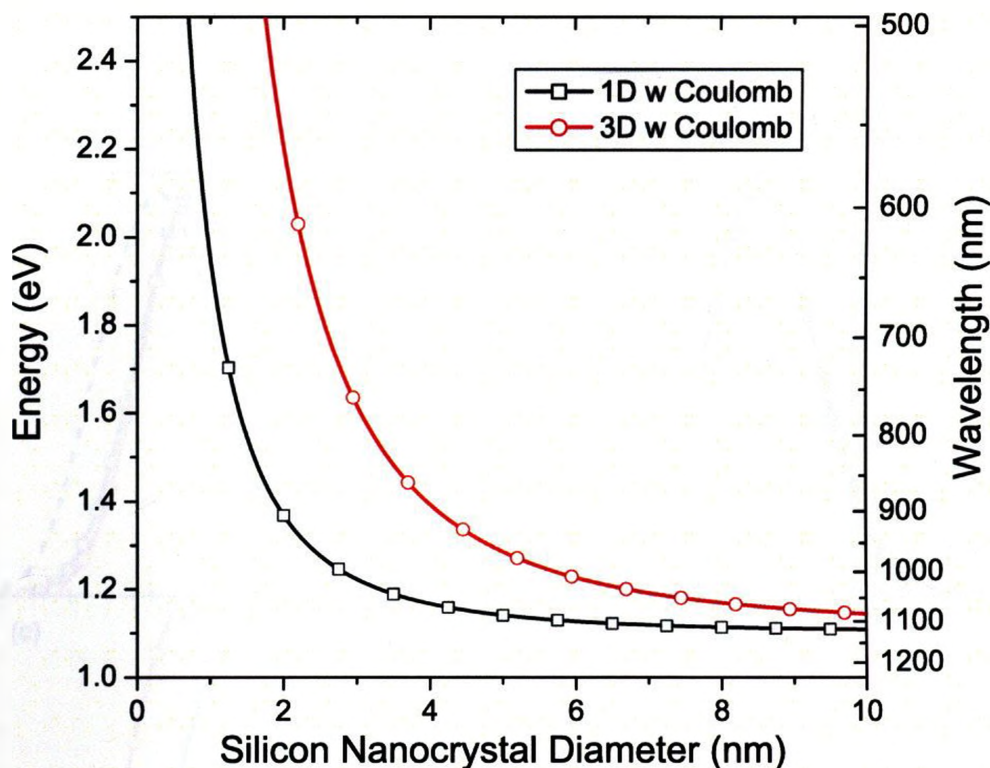

Figure D.3: The emission energy and wavelength for both the one-dimensional and three-dimensional models, with the inclusion of the Coulomb interaction.

a strong emission. Thus, the three-dimensional model as already stated does not adequately predict the emission characteristics of the Si-nc embedded in SiO_2.

In the case of the one-dimensional model, incorporating the Coulomb interaction improved on the already existing results in most cases. In Figure D.4, (a) and (b) are almost identical to the PL measurements, and for (e) and (f) the results improved on those presented in Figures 4.9 and C.2. For Figure D.4 (c) and (d) it is difficult to gauge the results due to the poor correspondence between the TEM distributions and the PL emission as discussed in Chapter 4. However, all of the simulations still have difficulties predicting the emission wavelengths above 1100 nm (below the band gap of silicon), which are due most likely to surface defects.

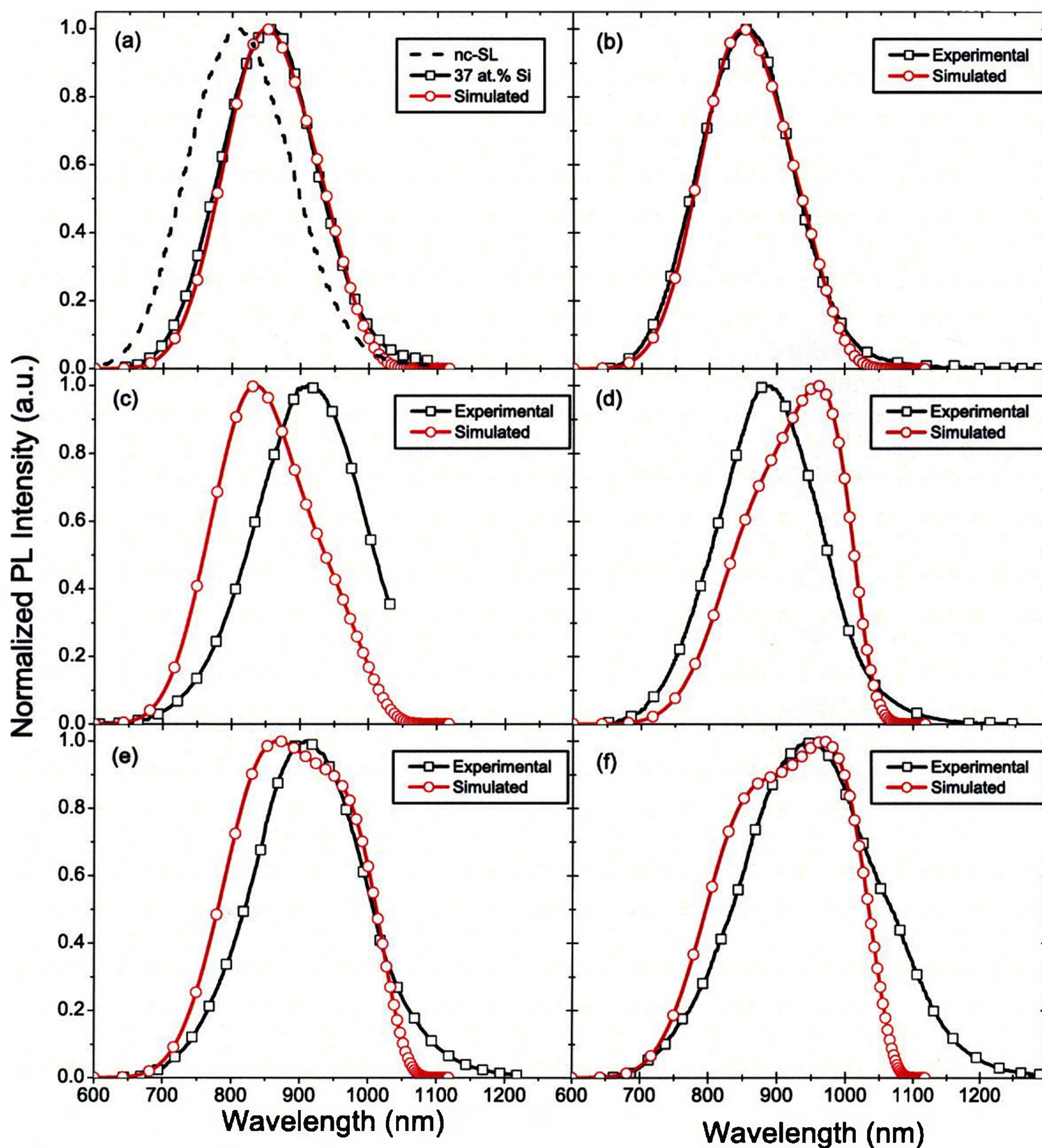

Figure D.4: The PL emission for (a - b), (d - f) are from Priolo *et al.* [64], and (c) is from Iacona *et al.* [80]. The simulated PL intensity incorporates the Coulomb interaction and is evaluated utilizing our own fits' of the TEM size distributions and not those stated in Ref. [80].

Table D.3: Summary of the experimental and simulated PL utilizing our own fit of the TEM distributions. The values in brackets of the "simulated" columns represent the difference between the experimental and simulated results.

Sample	Mean Diameter (nm)	σ (nm)	λ_{max} (nm)	λ_{max} Simulated (nm)	FWHM (nm)	FWHM Simulated (nm)
A1-SL	2.2	0.8	810	840 (+30)	175	160 (−15)
A2	2.2	0.6	860	850 (−10)	165	160 (− 5)
B1	2.0	0.4	900	850 (−50)	–	150 (–)
B2	2.2	0.4	850	850 (0)	160	160 (0)
B3	2.6	0.8	915	835 (−80)	185	180 (− 5)
B4	3.0	0.6	890	960 (+70)	175	180 (+ 5)
B5	3.4	1.0	910	870 (−40)	190	230 (+40)
B6	4.2	1.0	950	970 (+20)	230	240 (+10)
Mean Difference				38		11

Samples A - Priolo *et al.* [64]
Samples B - Iacona *et al.* [80]

BIBLIOGRAPHY

[1] L. C. Kimerling, *Appl. Surf. Sci.* **159-160**, 8 (2000).

[2] G. E. Moore, *Electronics* **38** (1965).

[3] Intel Corporation, http://www.intel.com/technology/mooreslaw/, *Moore's Law: Backgrounder.*

[4] International Technology Roadmap for Semiconductors (ITRS), *Home page*, http://www.itrs.net/about.html.

[5] International Technology Roadmap for Semiconductors (ITRS), *Interconnects*, 2007 edition.

[6] Intel Corporation, www.intel.com/go/sp/, *Intel's Photonics Technology Lab.*

[7] L. Pavesi and D. J. Lockwood, editors, *Silicon Photonics*, Springer, Berlin, 2004.

[8] H. Zimmermann, *Integrated Silicon Optoelectronics*, Springer, New York, 2000.

[9] L. Pavesi, *J. Phys.: Condens. Mat.* **15**, R1169 (2003).

[10] S. Ossicini, L. Pavesi, and F. Priolo, *Light Emitting Silicon for Microphotonics*, Springer, Berlin, 2003.

[11] O. Bisi, S. Campisano, L. Pavesi, and F. Priolo, *Silicon Based Microphotonics: from Basics to Applications*, IOS Press, Amsterdam, 1999.

[12] Intel Corporation, http://www.intel.com/technology/silicon/sp/, *Intel's Photonics Technology Lab.*

[13] B. G. Streetman and S. Banerjee, *Solid State Electronic Devices*, Prentice Hall, New Jersey, 2000.

[14] L. T. Canham, *Appl. Phys. Lett.* **57**, 1046 (1990).

[15] K. D. Hirschman, L. Tsybeskov, S. P. Duttagupta, and P. M. Fauchet, *Nature* **384**, 338 (1996).

[16] H. Takagi, H. Ogawa, Y. Yamazaki, A. Ishizaki, and T. Nakagiri, *Appl. Phys. Lett.* **56**, 2379 (1990).

[17] M. Yamamoto, R. Hayashi, K. Tsunetomo, K. Kohno, and Y. Osaka, *Jpn. J. Appl. Phys.* **30**, 136 (1991).

[18] R. Okada and S. Iijima, *Appl. Phys. Lett.* **58**, 1662 (1991).

[19] T. Shimizu-Iwayama, S. Nakao, and K. Saitoh, *Appl. Phys. Lett.* **65**, 1814 (1994).

[20] M. Molinari, H. Rinnert, and M. Vergnat, *Europhys. Lett.* **66**, 674 (2004).

[21] U. Gnutzmann and K. Clausecker, *Appl. Phys. B* **3**, 9 (1974).

[22] D. Kovalev, H. Heckler, M. Ben-Chorin, G. Polisski, M. Schwartzkopff, and F. Koch, *Phys. Rev. Lett.* **81**, 2803 (1998).

[23] P. M. Fauchet, *J. Lumin.* **70**, 294 (1996).

[24] M. V. Wolkin, J. Jorne, P. M. Fauchet, G. Allan, and C. Delerue, *Phys. Rev. Lett.* **82**, 197 (1999).

[25] G. Hadjisavvas and P. Kelires, *Physica E* **38**, 99 (2007).

[26] J. Heitmann, F. Müller, M. Zacharias, and U. Gösele, *Adv. Mater.* **17**, 795 (2005).

[27] B. Averboukh, R. Huber, K. W. Cheah, Y. R. Shen, G. G. Qin, Z. C. Ma, and W. H. Zong, *J. Appl. Phys.* **92**, 3564 (2002).

[28] G. Hadjisavvas and P. C. Kelires, *Phys. Rev. Lett.* **93**, 226104 (2004).

[29] X. X. Wang, J. G. Zhang, L. Ding, B. W. Cheng, W. K. Ge, J. Z. Yu, and Q. M. Wang, *Phys. Rev. B* **72**, 195313 (2005).

[30] A. J. Kenyon, C. E. Chryssou, C. W. Pitt, T. Shimizu-Iwayama, D. E. Hole, N. Sharma, and C. J. Humphreys, *J. Appl. Phys.* **91**, 367 (2002).

[31] A. D. Yoffe, *Advan. Phys.* **42**, 173 (1993).

[32] T. Takagahara and K. Takeda, *Phys. Rev. B* **46**, 15578 (1992).

[33] S. Godefroo, M. Hayne, M. Jivanescu, A. Stesmans, M. Zacharias, O. I. Lebedev, G. V. Tendeloo, and V. V. Moshchalkov1, *Nature Nanotech.* **3**, 174 (2008).

[34] L. W. Wang and A. Zunger, *J. Phys. Chem.* **98**, 2158 (1994).

[35] G. Allan, C. Delerue, and M. Lannoo, *Phys. Rev. Lett.* **76**, 2961 (1996).

[36] M. V. R. Krishna and R. A. Friesner, *J. Chem. Phys.* **96**, 873 (1992).

[37] J. F. Ziegler, J. P. Biersack, and U. Littmark, *The Stopping and Range of Ions in Solids*, Pergamon, New York, 1985.

[38] D. B. Williams and C. B. Carter, *Transmission electron microscopy: a textbook for materials science*, Plenum Press, New York, 1996.

[39] J. R. Tesmer and M. Nastasi, editors, *Handbook of modern ion beam materials analysis*, Materials Research Society, Pittsburgh, 1995, pp. 39-41.

[40] W. N. Lennard, H. Xia, and J. K. Kim, *Nucl. Instrum. Meth. B* **215**, 297 (2004).

[41] P. Asoka-Kumar, K. G. Lynn, and D. O. Welch, *J. Appl. Phys.* **76**, 4935 (1994).

[42] P. J. Simpson, M. Spooner, H. Xia, and A. P. Knights, *J. Appl. Phys.* **85**, 1765 (1999).

[43] D. W. Lawther and P. J. Simpson, *Defect Diffus. Forum* **138-139**, 1 (1996).

[44] S. Perkowitz, *Optical characterization of semiconductors : infrared, raman, and photoluminescence spectroscopy*, Academic Press, San Diego, 1993, p. 27.

[45] A. Li, Interaction of Nanoparticles with Radiation, in *Astrophysics of Dust*, edited by A. N. Witt, G. C. Clayton, and B. T. Draine, volume 309 of *Astronomical Society of the Pacific Conference Series*, pp. 417–453, 2004.

[46] A. R. Wilkinson and R. G. Elliman, *J. Appl. Phys.* **96**, 4018 (2004).

[47] X. wen Du, M. Takeguchi, M. Tanaka, and K. Furuya, *Appl. Phys. Lett.* **82**, 1108 (2003).

[48] E. Balanzat and S. Bouffard, *Solid State Phenom.* **30**, 7 (1992).

[49] L. A. Nesbit, *Appl. Phys. Lett.* **46**, 38 (1985).

[50] M. L. Brongersma, A. Polman, K. S. Min, and H. A. Atwater, *J. Appl. Phys.* **86**, 759 (1999).

[51] D. L. Griscom, *J. Non-Crystal. Solids* **73**, 51 (1985).

[52] G. Ghislotti, B. Nielsen, P. Asoka-Kumar, K. G. Lynn, L. F. Di Mauro, F. Corni, and R. Tonini, *Appl. Phys. Lett.* **70**, 496 (1997).

[53] A. Kalnitsky, J. P. Ellul, E. H. Poindexter, P. J. Caplan, R. A. Lux, and A. R. Boothroyd, *J. Appl. Phys.* **67**, 7359 (1990).

[54] M. Fujinami and N. B. Chilton, *Appl. Phys. Lett.* **62**, 1131 (1993).

[55] G. Ghislotti, B. Nielsen, P. Asoka-Kumar, K. G. Lynn, C. Szeles, C. E. Bottani, S. Bertoni, G. F. Cerofolini, and L. Meda, *Thin Solid Films* **276**, 310 (1996).

[56] A. P. Knights, P. J. Simpson, L. B. Allard, J. L. Brebner, and J. Albert, *J. Appl. Phys.* **79**, 9022 (1996).

[57] G. C. Aers, *AIP Conf. Proc.* **218**, 162 (1990).

[58] T. Müller, K.-H. Heinig, and W. Möller, *Appl. Phys. Lett.* **81**, 3049 (2002).

[59] B. Garrido Fernandez, M. López, C. García, A. Pérez-Rodríguez, J. R. Morante, C. Bonafos, M. Carrada, and A. Claverie, *J. Appl. Phys.* **91**, 798 (2002).

[60] M. Born and E. Wolf, *Principles of optics*, Pergamon Press, New York, 1970, pp. 57-60.

[61] H. A. Macleod, *Thin-film optical filters*, Institute of Physics Pub., Philadelphia, PA, 2001, pp. 40-49.

[62] D. Kovalev, J. Diener, H. Heckler, G. Polisski, N. Künzner, and F. Koch, *Phys. Rev. B* **61**, 4485 (2000).

[63] C. Garcia, B. Garrido, P. Pellegrino, R. Ferre, J. A. Moreno, J. R. Morante, L. Pavesi, and M. Cazzanelli, *Appl. Phys. Lett.* **82**, 1595 (2003).

[64] F. Priolo, G. Franzò, D. Pacifici, V. Vinciguerra, F. Iacona, and A. Irrera, *J. Appl. Phys.* **89**, 264 (2001).

[65] J. P. Proot, C. Delerue, and G. Allan, *Appl. Phys. Lett.* **61**, 1948 (1992).

[66] E. Kasper and D. J. Paul, *Silicon Quantum Integrated Circuits: Silicon-germanium Heterostructure Devices : Basics and Realisations*, Springer, New York, 2005.

[67] H. Namatsu, S. Horiguchi, Y. Takahashi, M. Nagase, and K. Kurihara, *J. J. Appl. Phys.* **36**, 3669 (1997).

[68] Z. A. Weinberg, *J. Appl. Phys.* **53**, 5052 (1982).

[69] Y. T. Hou, M. F. Li, Y. Jin, and W. H. Lai, *J. Appl. Phys.* **91**, 258 (2002).

[70] R. K. Chanana, K. McDonald, M. D. Ventra, S. T. Pantelides, L. C. Feldman, G. Y. Chung, C. C. Tin, J. R. Williams, and R. A. Weller, *Appl. Phys. Lett.* **77**, 2560 (2000).

[71] M. I. Vexler, S. E. Tyaginov, and A. F. Shulekin, *J. Phys-Condens. Mat.* **17**, 8057 (2005).

[72] R. J. Walters, G. I. Bourianoff, and H. A. Atwater, *Nature Mater.* **4**, 143 (2005).

[73] C.-T. Sah, *Fundamentals of solid-state electronics*, World Scientific, River Edge, NJ, 1991.

[74] S. M. Sze, *Physics of Semiconductor Devices*, John Wiley & Sons, New York, 1981.

[75] N. Holonyak, R. Kolbas, R. Dupuis, and P. Dapkus, *IEEE J. Quantum Elect.* **16**, 170 (1980).

[76] Z. H. Lu, J.-M. Barubeau, D. J. Lockwood, M. Buchanan, N. Tit, C. Dharma-Wardana, and G. C. Aers, *Proc. SPIE* **3491**, 457 (1998).

[77] L. Pavesi, *J. Appl. Phys.* **80**, 216 (1996).

[78] J. Linnros, N. Lalic, A. Galeckas, and V. Grivickas, *J. Appl. Phys.* **86**, 6128 (1999).

[79] L. Pavesi, L. Dal Negro, C. Mazzoleni, G. Franzò, and F. Priolo, *Nature* **408**, 440 (2000).

[80] F. Iacona, G. Franzò, and C. Spinella, *J. Appl. Phys.* **87**, 1295 (2000).

[81] V. Y. Timoshenko, M. G. Lisachenko, O. A. Shalygina, B. V. Kamenev, D. M. Zhigunov, S. A. Teterukov, P. K. Kashkarov, J. Heitmann, M. Schmidt, and M. Zacharias, *J. Appl. Phys.* **96**, 2254 (2004).

[82] A. R. Wilkinson and R. G. Elliman, *Phys. Rev. B* **68**, 155302 (2003).

[83] K. S. Min, K. V. Shcheglov, C. M. Yang, H. A. Atwater, M. L. Brongersma, and A. Polman, *Appl. Phys. Lett.* **69**, 2033 (1996).

[84] M. Fujii, M. Yoshida, Y. Kanzawa, S. Hayashi, and K. Yamamoto, *Appl. Phys. Lett.* **71**, 1198 (1997).

[85] M. Revitz, S. I. Raider, and R. A. Gdula, *J. Vac. Sci. Technol.* **16**, 345 (1979).

[86] F. Iacona, C. Bongiorno, C. Spinella, S. Boninelli, and F. Priolo, *J. Appl. Phys.* **95**, 3723 (2004).

[87] G. Ledoux, O. Guillois, D. Porterat, C. Reynaud, F. Huisken, B. Kohn, and V. Paillard, *Phys. Rev. B* **62**, 15942 (2000).

[88] T. Iwayama, T. Hama, D. Hole, and I. Boyd, *Vacuum* **81**, 179 (2006).

[89] S. I. Raider, R. A. Gdula, and J. R. Petrak, *Appl. Phys. Lett.* **27**, 150 (1975).

[90] B. Pivac, B. Rakvin, A. Borghesi, A. Sassella, M. Bacchetta, and L. Zanotti, *J. Vac. Sci. Technol. B* **17**, 44 (1999).

[91] J. D. Plummer, M. Deal, and P. B. Griffin, *Silicon VLSI Technology*, Prentice Hall, Toronto, 2000, p. 356.

[92] A. R. Wilkinson and R. G. Elliman, *Appl. Phys. Lett.* **83**, 5512 (2003).

[93] N. Lalic and J. Linnros, *J. Lum.* **80**, 263 (1998).

[94] M. A. Green, J. Zhao, A. Wang, P. J. Reece, and M. Gal, *Nature* **412**, 805 (2001).

[95] H. Rong, A. Liu, R. Jones, O. Cohen, D. Hak, R. Nicolaescu, A. Fang, and M. Paniccia, *Nature* **433**, 292 (2005).

[96] A. Irrera, D. Pacifici, M. Miritello, G. Franzò, F. Priolo, F. Iacona, D. Sanfilippo, G. Di Stefano, and P. G. Fallica, *Appl. Phys. Lett.* **81**, 1866 (2002).

[97] O. Arakaki, A. Hatta, T. Ito, and A. Hiraki, *J. J. Appl. Phys.* **33**, 6586 (1994).

[98] S. M. Pillai, Z. Y. Xu, M. Gal, R. Glaisher, M. Phillips, and D. Cockayne, *J. J. Appl. Phys.* **31**, L1702 (1992).

[99] L. H. Abuhassan, M. R. Khanlary, P. Townsend, and M. H. Nayfeh, *J. Appl. Phys.* **97**, 104314 (2005).

[100] M. A. Stevens Kalceff and M. R. Phillips, *Phys. Rev. B* **52**, 3122 (1995).

[101] S. Van Petegem, C. Dauwe, T. Van Hoecke, J. De Baerdemaeker, and D. Segers, *Phys. Rev. B* **70**, 115410 (2004).

[102] B. Nielsen, K. G. Lynn, Y.-C. Chen, and D. O. Welch, *Appl. Phys. Lett.* **51**, 1022 (1987).

[103] A. Franceschetti and A. Zunger, *Phys. Rev. Lett.* **78**, 915 (1997).

[104] H. Haug and S. W. Koch, *Quantum Theory of the Optical and Electronic Properties of Semiconductors*, World Scientific, Singapore, 1990.

[105] J. H. Davies, *The Physics of Low-dimensional Semiconductors: An Introduction*, Cambridge University Press, New York, 1998.

[106] R. Tsu, L. Ioriatti, J. F. Harvey, H. Shen, and R. A. Lux, *Mater. Res. Soc. Symp. Proc.* **283**, 437 (1993).

[107] D. R. Penn, *Phys. Rev.* **128**, 2093 (1962).

[108] L.-W. Wang and A. Zunger, *Phys. Rev. Lett.* **73**, 1039 (1994).

[109] G. Bastard, E. E. Mendez, L. L. Chang, and L. Esaki, *Phys. Rev. B* **26**, 1974 (1982).

[110] D. A. B. Miller, D. S. Chemla, T. C. Damen, A. C. Gossard, W. Wiegmann, T. H. Wood, and C. A. Burrus, *Phys. Rev. B* **32**, 1043 (1985).

[111] L. E. Brus, *J. Chem. Phys.* **80**, 4403 (1984).

[112] T. Takagahara, *Phys. Rev. B* **47**, 4569 (1993).